Particle-Stabilized, Bicontinuous Emulsions with Nanostructured Domains

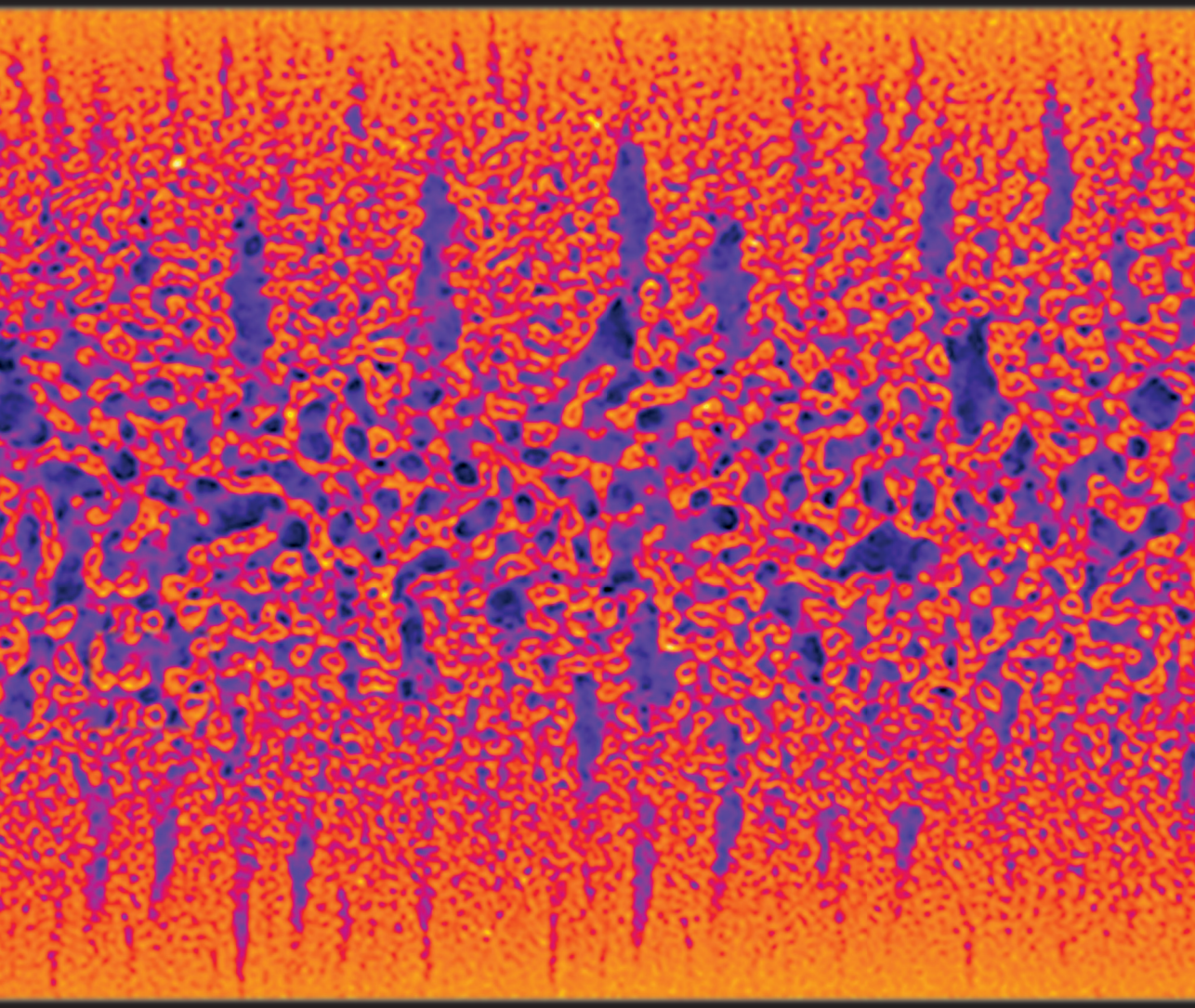

Mohd Azeem Khan

Particle-Stabilized, Bicontinuous Emulsions with Nanostructured Domains

Mohd Azeem Khan

Titel: Particle-Stabilized, Bicontinuous Emulsions with Nanostructured Domains

ISBN/EAN: 978-94-6469-267-9

DOI of dissertation: https://doi.org/10.33540/1668

Cover design by: Mohd Azeem Khan

Confocal micrograph of silica monolith of a nanostructured bijel fiber

Printed by: ProefschriftMaken

Particle-Stabilized, Bicontinuous Emulsions with Nanostructured Domains

Deeltjes-gestabiliseerde Bicontinue Emulsies met Nanogestructureerde Domeinen

(met een samenvatting in het Nederlands)

Proefschrift

ter verkrijging van de graad van doctor aan de
Universiteit Utrecht
op gezag van de
rector magnificus, prof.dr. H.R.B.M. Kummeling,
ingevolge het besluit van het college voor promoties
in het openbaar te verdedigen op

woensdag 22 maart 2023 des middags te 4.15 uur

door

Mohd Azeem Khan

geboren op 11 augustus 1990
te Gyanpur, India

Promotor:
Prof. dr. W.K. Kegel

Copromotor:
Dr. M.F. Haase

Beoordelingscommissie:
Prof. dr. A. Meijerink
Prof. dr. D. Bonn
Prof. dr. P.E. de Jongh
Prof. dr. A.P. Philipse
Prof. T. Zemb

This project has received funding from the European Research Council (ERC) under the European Union's Horizon 2020 research and innovation programme (Grant agreement no. 802636).

Contents

Introduction

1.1 General introduction

Contrary to solids, which have a definite shape, liquids typically have flow properties and tend to adopt the shape of their containers. This is because intermolecular attractive interactions (i.e. van der Waals forces, hydrogen bonding) in liquids are weak (only a few kT) hence the thermal energy of the molecules allows them to escape attractive forces. Whereas in solids, intermolecular interactions are very strong (i.e. covalent bonds) and impart a rigid structure. Over the last few decades, the interaction of liquid flow parameters with solids' shaping properties has become an attractive area of research. Solid particles can attach to the liquid interface and selectively rigidify the interface without changing the bulk properties.[1, 2] A dense particle crust formed at the liquid interface can be deformed to stabilize the non-equilibrium shape of liquids.[3, 4] This allows particle-stabilized liquids to be configured in different shape and assemblies for use in a range of applications such as tissue engineering[5, 6], liquid devices, and energy storage.[7, 8] In this thesis, we discuss non-spherical liquid shape stabilization by interfacial crosslinking and jamming of particles. We discuss two methods to form the non-spherical liquid structures, *i.* by applying force (gravitational and hydrodynamics) and *ii.* arresting the liquid-liquid demixing. The research contributes to a better understanding of different physical and physiochemical parameters that govern the control over the non-spherical structure formation, stability, and potential scalability.

1.2 Shaping Liquids

In the scope of our discussion on shaping liquids, we will briefly discuss the basic concepts of solid particles at the interface followed by past research on particle-stabilized non-spherical liquid shapes. Further, we connect our research findings to the advancement of liquid reconfiguration with economic, controlled and scalable methods. We start with discussing flow properties of matter, when a mechanical force is applied to a solid it builds up internal stress and stores the applied force as internal energy. In contrast, when a force is applied to a liquid, the energy is dissipated by flow,

resulting in friction between the fluid layers, and eventually the production of heat (dissipation). The science of flow and deformation of materials, especially liquid and soft matter is studied under Rheology.[9] The property of flow in materials is usually defined by yield stress, it's the threshold stress required before the sample starts to flow.[10] Solid materials have high yield stress (steel ~ 240 MPa). Liquids are divided as per their response to the applied stress. Shear-responsive fluids (Non-Newtonian fluid) have a wide range of applications due to their shape retention ability: toothpaste, mortars, foam, mayonnaise, etc. On the other hand, Newtonian fluids show no yield stress and have a constant viscosity with zero shear rate at zero shear stress.[10]

As mentioned earlier attractive intermolecular forces (hydrogen bonding, van der Waals attractions) define the physical state of a matter and are collectively called cohesive forces.[11] At a given temperature and pressure the net cohesive force acting on a molecule in the bulk is zero whereas a surface molecule experiences a non-zero net force directed toward the bulk liquid (Fig. 1.1). This imbalance of the net force on the liquid surface implies a pulling force towards the bulk and shapes the liquid with the minimum surface area. This is the reason behind the nearly spherical shape of a free-falling water droplet, the drop tried to minimize interfacial area and associated energy by attaining the lowest surface area to volume ratio (spherical geometry).[12]

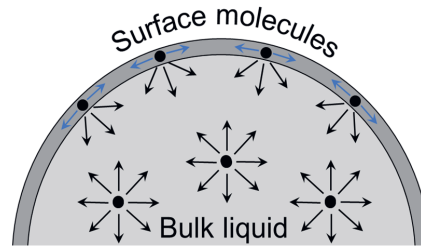

Fig. 1.1 Schematic representation of cohesive forces acting on liquid molecules at the surface and in the bulk.

The drive towards the surface minimization of liquids is defined as "surface tension (γ)" and mainly depends on the attractive forces between the molecules of a liquid. Surface tension and surface-free energy are physically equivalent and used as per the system, if the adjacent phase is solid, surface-free energy is used and in the case of fluids referred to as surface tension (air) or interfacial tension (liquid).[13] Mathematically, surface tension is defined as the force per unit length of a liquid surface or the energy required to create a unit interfacial area between liquid-liquid or liquid-gas phases.[14]

$$\gamma = \frac{dG}{dA} \tag{1}$$

Where γ is the surface tension, dG is the energy required to increase the system's area by dA. The SI unit of surface tension is mN/m or J/m^2. Interfacial tension plays a major role in multiphasic liquid systems and usually drives the system toward a minimum energy state. A common example is mixing oil and water where external energy generates a large area associated with high interfacial

energy of droplets (dispersed phase) of one phase in the other. These droplets tend to reduce the energy expensive area by coalescing where droplets merge to make bigger drops and if not stabilized, the liquids phase separates to attain a minimum energy state linked to the smallest possible interfacial area.[15, 16] Although this is not the case always, these energetically expensive drops can be kinetically trapped in a metastable energy state called emulsions.[17] Some of the examples in our everyday life are milk (oil in water), margarine (water in oil), and ice cream (oil and air in water emulsion with solid ice particles). All these stable emulsion systems have near spherical drops of a dispersed phase in the continuous phase due to the minimum energy principle.

Shaping liquids away from spherical drops to anisotropic shapes is possible either by external or internal means. Most common examples can be cited from nature where compartmentalization of liquids forms cell organelles and vesicles with various shapes.[18] Understanding the formation mechanism of these organelles has motivated researchers to employ the self-assembly of monomers such as lipids[19], polymers[20-22], and colloids[23-26] to stabilize the non-spherical shapes of liquid.

As mentioned earlier to change the equilibrium shape of a liquid drop one has to alter the cohesive interaction either by external forces or internally by perturbing the chemical interactions of molecules. The former method involves external forces such as shear or mechanical stress, gravitational-, and hydrodynamic forces to form the non-spherical shape of the liquid that can be further stabilized by different means.[27-29] Next, chemically induced surface tension alterations are a well known method for checking the analytical purity of a substance.[13, 30] For example, surfactants are common chemicals involved in our daily lives to modulate liquid surface tension in various food, drugs, and commercial products.[31-33] Surfactants are amphiphilic molecules having a hydrophilic head and hydrophobic tail. Chemical interactions of surfactants with the bulk molecule alter the cohesive forces and reduce the surface tension. The amphiphilic nature of surfactant molecules drives their self-assembly at the oil-water interface to form emulsions. Emulsions are found in nature from cellular to physiological level processes.[34] Due to the high surface area of the droplets, emulsification has been applied to a wide spectrum of applications such as metallurgy[35], medicine[36], cosmetics[37], drugs[5], and oil recovery.[38, 39]

Small attachment energies of surfactant molecules are susceptible to thermal fluctuations and usually not able to stabilize the emulsions at varying processing conditions.[40] For the same reason when a drop is deformed to a non-spherical shape surfactants are not able to stabilize the non-equilibrium shape. Therefore, surfactants can alter the interfacial properties to deform the drop shape but can not stabilize the deformed shape. On the other hand, colloids are also interfacially active and have attachment energies considerably high to circumvent the thermal fluctuations and impart rigid boundaries to liquid.

1.3 Pickering emulsions

Particle-stabilized emulsions also known as Pickering emulsions were introduced by Pickering and Ramsden more than a century ago.[1, 2] However, it's only in recent decades Pickering emulsions have gained more attention due to the rapid development of micro- and nanomaterials.[41] A variety of particles not only impart higher control and stability over the emulsion formation processes but also open a vast array of functionalities feasible with them. Solid particles have several advantages over surfactants like relatively higher stability and solid material properties such as conductivity, responsiveness, and porosity. Also, easy conjugations with biomolecules and biocompatible particles have advanced our reach for targeted and responsive therapies.[5] Sustainable approaches are appreciated due to the easy recycling of particles and moderate environmental impacts.[42]

Particle-stabilized emulsions have been studied extensively to describe the theory and mechanism of particle-based stabilization of emulsion drops. Pickering emulsions are thermodynamically not stable but the particles arrest the energy expensive high surface area of drops kinetically in the continuous phase.[43]

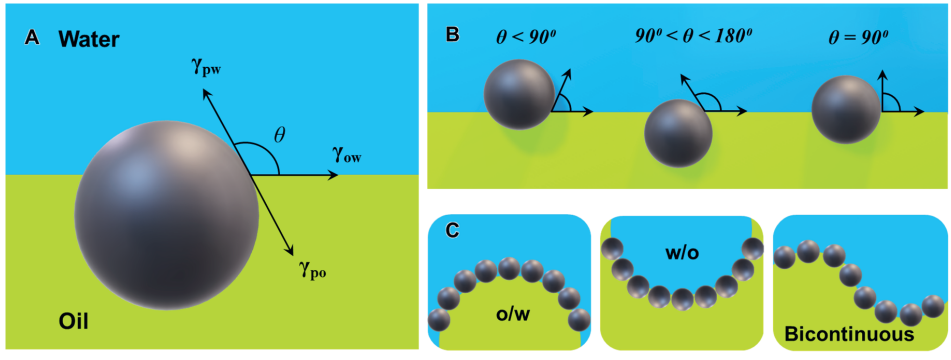

Fig. 1.2 Schematic depiction of particles at the oil-water interface A) Three-phase contact angle of the particle at the interface B) Contact angle varies depending on the particle hydrophobicity C) resulting curvature of the interface due to the particle hydrophobicity.

A key parameter to define the particle behavior at the fluid interface is the three-phase contact angle θ. It is the angle measured between the tangents to the solid surface and the liquid-liquid interface originating at the interface of solid and liquid surfaces.[44] By convention, the contact angle is

measured through the more polar phase. Fig. 1.2A shows the contact angle measurement, which depends on the surface free energies of the particle-oil (γ_{po}), particle-water (γ_{pw}), and oil-water (γ_{ow}) as per Young's equation.[45] It is important to note here that a particle will take up an equilibrium position at the liquid-liquid interface according to the three-phase contact angle without deforming the interface.[46]

$$\cos\theta = \frac{(\gamma_{po} - \gamma_{pw})}{\gamma_{ow}} \quad (2)$$

Depending on the wettability, particles position at the interface with a certain contact angle and impart a curvature. Hydrophilic particles with $\theta < 90^{o}$ attain the equilibrium position at the interface to maximize the surface area in the water phase and stabilize oil in water emulsion (o/w), whereas hydrophobic particles $\theta > 90^{o}$ form water in oil emulsion (w/o) (Fig. 1.2B & C). Interestingly, amphiphilic particles with a contact angle of 90^{o} do not have a preferential curvature towards the interface and can stabilize non-spherical drop shapes.

Neglecting the effect of gravity for a spherical solid particle (< 1 micron), the attachment energy is given by the following formula

$$\Delta G_{attach} = -\pi \cdot r^2 \cdot \gamma_{ow}(1 \pm \cos\theta)^2 \quad (3)$$

with r the particle radius, γ_{ow} the oil/water interfacial tension, and θ the three-phase contact angle.[47] It's important to note here, this simplified formula does not take into account effects arising from line tension k (important for particles < 10 nm, when k ranges from 10^{-11} – 10^{-9} N), which can change θ and result in an adsorption barrier for particles.[48] Particles do not change the interfacial tension between two immiscible liquids but reduce the effective fluid-fluid interfacial area equivalent to their cross-sections at the interface.[49] Furthermore, we discuss the two main factors affecting ΔG_{attach}. for a given immiscible liquid pair, *i*. particle size and *ii*. contact angle. Fig. 1.3 A shows the particle size dependency on ΔG_{attach}, for a toluene-water system (γ_{ow} = 36 mN/m) with $\theta = 90^{o}$ particle contact angle. In theory particles above r = 1 nm size with attachment energy of more than 27.5 kT should be safe from thermal fluctuations.[50] As we increase the particle size to 10 nm and above particles attain attachment energy several magnitudes higher than the thermal energy (kT, k is Boltzmann constant and T is the temperature) and attach to the interface irreversibly (Fig. 1.3A).

Another factor influencing the attachment energy is the contact angle θ, the same water-toluene system with r =10 nm particle size is used to calculate the ΔG_{attach} as a function of different contact angles. Fig. 1.3B shows that as the particle contact angle increases from 0 to 180^{o} the attachment increases from zero to maximum at $\theta = 90^{o}$ and again reduces to zero at $\theta = 180^{o}$. The negative values of particle attachment energy even at contact angles close to 0^{o} and 180^{o} show that particles

remain surface active for a wide range of hydrophobicity and self-assemble at the oil-water interface.[44]

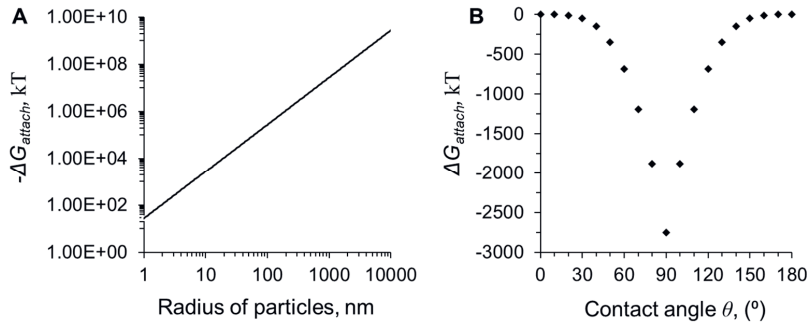

Fig. 1.3 A) Variation of interfacial attachment energy we change the particle size with 90º contact angle and γ_{ow} = 36 mN/m. B) Interfacial attachment energy as a function of contact angle for 10 nm particles at the water-toluene interface (γ_{ow} = 36 mN/m).

For contact angle variation the maximum ΔG_{attach} is attained at a θ = 90º, and calculated to be 2750 kT which is high enough to circumvent the ejection from the interface due to thermal fluctuations. The attachment energy of particles with different wettability has been studied using external forces such as Langmuir trough[51], drop size reduction[28], and microfluidic shear.[52] Generally, upon compression of the interface, particles with hydrophilic or hydrophobic surface modifications detach into the favorable bulk liquids. Nanoparticles with equal wetting towards the liquids ($\theta \sim 90º$) exhibit jamming and formed rigid interface buckles to accommodate the excess stress.[28, 53] Notably, in Fig. 1.3B particles with a contact angle near 90º also seem to have ΔG_{attach} high enough to jam at the interface but do not support the effective stabilization of co-continuous liquid structures.[4]

In emulsions, droplets are the dispersed phase stabilized by hydrophilic or hydrophobic particles. This generates an enormous interfacial area of secluded drops against the continuous phase. For example, milk (500 ml) has around 12 *vol* % fat (oil) and the average size of fat globules size is ~ 2.5 microns which equates to $8.5*10^{11}$ oil drops. The calculated oil-water interfacial area in the emulsion is 70.3 m^2 which is surprisingly higher than the total surface area of the jar around 0.04 m^2 (shape dependent). The large interfacial area and development of engineered particles have enabled particle-stabilized emulsion application in the field of porous materials[54], energy storage[55], separation[56], and organic semiconductors.[57]

The large interfacial area between oil and water is advantageous for many applications but the isolated drop phase limits the employment of emulsions in continuous process applications.[58] Further, shaping the drops in specific architecture and patterns can allow potential applications in liquid flow devices and 3D fabrication.[59, 60] Now the question arises can particles also stabilize

non-spherical drop shapes? From the previous discussion, we learned that particles depending on the size and wettability can attach to the interface and make a rigid layer to stabilize the drop phase. Interestingly, in the case of amphiphilic particles having non-preferential wetting properties, they can support interfacial bending in either direction to stabilize non-spherical shapes. Although the theoretical shreds of evidence were available for almost a century not much research was done towards stabilizing non-spherical droplets until the late 1980s.

1.4 Non-spherical droplets and Bicontinuous emulsion gels

In the past two decades, there have been recognizable advancements in the field of additive manufacturing fueled by technological advances, computer-aided design, and myriads of material that can be printed layer by layer to form an object.[61] A similar principle is used for microfluidic-based 3D printing of all liquid systems. Recent developments have shown that tuning the interfacial tension and surface properties of nanoparticles enable the formation of reconfigurable liquids.[20]

Adding to the discussion of drop shape deformation, external factors such as force[3], pressure [62], and electromagnetic field [63] have been employed to deform the droplet shape which is consequently stabilized by particle jamming at the interface. In one of the initial studies, Subramaniam *et al*. showed that polystyrene stabilized bubbles can be deformed into stable non-spherical shapes upon compressing between two glass plates.[3] In another study, Cui *et al*. reported spherical to ellipsoidal shape change of a drop by applying the electric field which increases the interfacial area by elongating the drop and simultaneously surface active particle attached to the newly generated interfacial area. Once the field is off liquid drop reconfigures to minimize the surface area leading to the jamming of nanoparticles and forming a layer at the interface to support the ellipsoidal drop shape.[63] Recently, Xubo *et al*. made liquid tubules by lowering the interfacial tension to form a liquid jet stabilized with oppositely charged nanoparticles and polymers.[29] All of these reports describe different tools one can use to form non-spherical droplets using interfacial jamming, however considering the surging demand for additive manufacturing products we need continuous methods which are economic and easy to upscale.

In ***Chapter 2***, we discuss the non-equilibrium shape stabilization of droplets via trivalent Lanthanum ion (La^{3+}) mediated crosslinking of percolating silica nanoparticle layer at the oil-water interface. We reduce the interfacial tension by adding a solvent to the oil phase which facilitates the elongation of drop either via gravitational or hydrodynamic forces. Simultaneously, negatively charged silica nanoparticles (Ludox TM) decorated with positively charged short-chain surfactant hexyltrimethyl ammoniumbromide (C_6TAB) are swept to the interface. These surfactant-modified particles at the

interface are crosslinked with a multivalent cation La^{3+} to rigidify the structure. In this study, we argue that the mechanism of droplet shape stabilization is not interfacial jamming but crosslinking of nanoparticles via La^{3+}. To prove our hypothesis we perform a series of experiments including foam stability, pendant drop (tensiometry), and microfluidics. Obtained results suggest that we need C_6TAB-modified (surface -active) particles with threshold concentrations of solvent and La^{3+} ions to stabilize the nonequilibrium shapes. We introduce models to analyze the hydrodynamic forces and the nanoparticle deposition rates on the droplets. Our technique of forming anisotropic oil droplets and tubules can potentially be used for different types of oil. For instance, acrylic oils can allow for the formation of polymeric microparticles and fibers. Moreover, our approach can be further developed for the 3D-printing of Newtonian fluids, complementing the existing additive manufacturing techniques.

The second approach we consider for liquid shape modeling is internal and involves liquid-liquid demixing. In the literature, two different mechanisms are discussed for liquid-liquid demixing *i*. nucleation and growth (NG) *ii*. spinodal decomposition (SD). Depending on how fast the system moves from the thermodynamically stable conditions (below the binodal curve, Fig 1.4) to the metastable/unstable regions, it either demixes via NG or SD mechanism.[64] The "Ouzo effect" is an example of metastable nucleated oil droplets in water. When a water-rich ternary mixture in the miscible region is mixed with some water, the system shifts to the metastable region and spontaneous emulsification produces a milky oil-in-water emulsion.[65] The metastable region is relatively stable and generated long-lived micron-sized droplets, unlike the unstable spinodal regime. Spinodal demixing results from fast quenching into the two-phase region limited by the spinodal curvature and critical point.[66] The resultant structures are shown in Fig 1.4, NG results in the drop of one phase on the other phase whereas SD forms a continuous network of immiscible liquids.

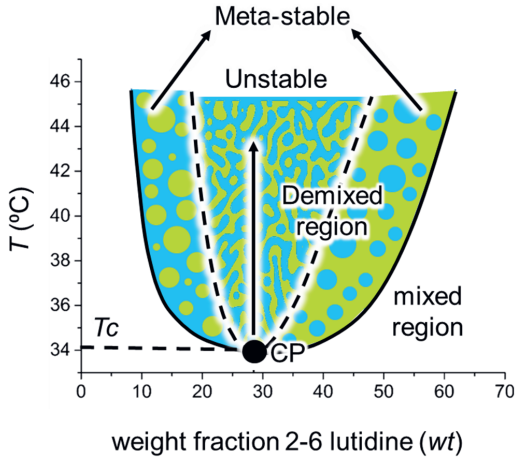

Fig. 1.4 Liquid-liquid phase diagram of 2-6 Lutidine and water with upper critical temperature *Tc* at the critical weight fraction of 2-6 lutidine. Temperature quench into the metastable region leads to demixing by nucleation and growth. Solid arrow shows demixing in the unstable spinodal region. A Binodal curve (solid line) separates the mixed region from demixed region and the dashed line of the spinodal curve separates the metastable and unstable regions.

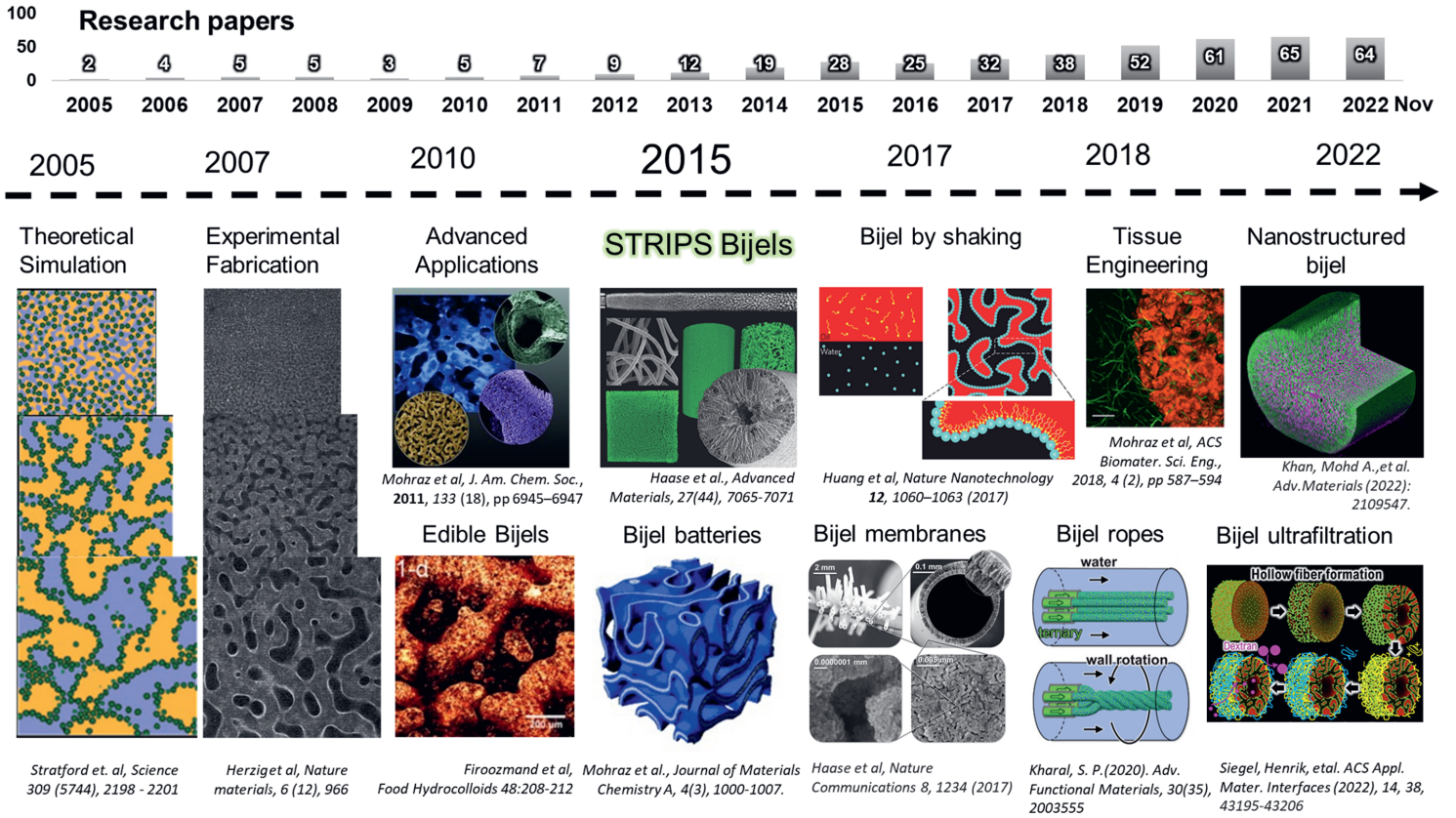

Fig. 1.5 Bijel research time line

In the scope of our discussion about non-spherical liquid structures, we will focus more on SD demixing and the resulting structure. Fig 1.4 shows the two-phase region of a liquid-liquid phase diagram of water and 2-6 lutidine as a function of temperature and liquid compositions.[67] Above the binodal curve, the two-phase region shows two different ways of demixing as discussed earlier. At a critical composition shown as the critical point (CP), the system can enter the spinodal regime of demixing via the shortest path. Spinodal demixing of liquids and formed liquid networks have been studied in past, especially on the mechanistic aspect.[68, 69]. However, applications were limited to mainly in the field of membrane science where phase separation was used to fabricate porous semipermeable membranes.[59, 64]

In 2005 for the first time, a simulation study proposed that spinodal demixing of two immiscible liquids can be arrested by particles jamming at the interface.[50] A century-old discovery by Pickering and Ramsden was employed here in the spinodal demixing of liquids to stabilize the liquid channels with equally wetting particles. Amphiphilic particles attach to the interface with high attachment energy and support curvatures in both negative and positive directions.[4] This new class of material was called as bicontinuous interfacially jammed emulsion gels (Bijels). Immiscible liquids retain their flow properties and the liquid interface is covered with a percolating jammed layer of solid particles providing rigidity and confinement to the liquid phases. In 2005, simulation studies suggested that bijel could form if interfacial tension and particle hydrophobicity were tuned during spinodal phase separation. In the year 2007, Herzig *et al* first time reported the bijel fabrication in the laboratory by heating a selected composition (critical point) of 2-6 lutidine and water mixture above a critical temperature (Tc = 34.1ºC, heating range 24 – 40ºC).[70] This led to the demixing of the liquid in the spinodal regime where equally wetted silica particles attached to the interface and jammed to form a bicontinuous structure of water and lutidine. These two studies pioneered a new soft matter field of bicontinuous emulsion gels and in the past two decades, bijels have seen rampant growth to be engineered as a hosting material for applications ranging from energy storage, tissue engineering, membranes, and reactive separations.[71-74]. Kinetically arrested bijel structure shows statistically significant association with the gyroid-like minimal surfaces and minimal surface structures comprising bicontinuous, symmetric phases are predicted to provide optimal transport properties.[75] Fig. 1.5 captures a comprehensive timeline of bijel research in the course of the past two decades, together with the research outputs, to highlight the variety of applications for bijel as a material.

One of the major limitations of bijel fabrication was the selection of preferential pairs of immiscible liquids which constrained the liquid selection and control over the fabrication process. Generally used liquid pairs are chemically not too dissimilar and have lower interfacial tension upon phase separation. Hence, larger particles are used to compensate for the attachment energy which limits

the domain size and effective surface area.[76] In 2015 Haase *et al* introduced a bijel fabrication method called Solvent Transfer Introduces Phase Separation (STrIPS).[77] Fig. 1.6 nicely captures the sizable research leap taken forward with STrIPS, enabled by the use of different liquids with a cosolvent and nanoparticles (< 50 nm) as stabilizers to generate an enormous interface.[78] Microfluidics combined with STrIPS allows continuous bijel fabrication by introducing a homogeneous precursor mixture of oil-water-solvent with surface-active nanoparticles in a continuous phase, in which solvent diffusion immediately triggers the demixing. During the demixing, nanoparticles attain amphiphilic hydrophobicity and jam at the interface upon coarsening to form bijels.[78] Most of the bijel-associated applications leverage the high interfacial area between the liquids or the templated porous material.

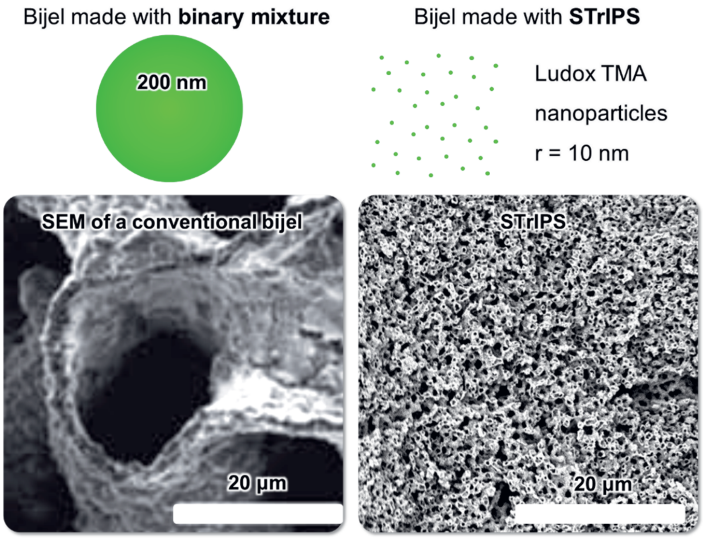

Fig. 1.6 Scanning electron micrographs of bijels made via the conventional binary liquid method and STrIPS bijel stabilized with nanoparticles. Schematics are not drawn to scale.

STrIPS enabled the application of small nanoparticles (< 50 nm) as bijel stabilizers and we further translate this knowledge in ***Chapter 3*** to fabricate nanostructured bicontinuous emulsion gels. This is the first report to show the continuous fabrication of uniform bijel structures with an average domain size range between 300-500 nm to generate a specific area of around 2 m^2/cm^3. This is possible due to the fast quenching of the phase separating fluids as a result of preferential solvent partitioning in the continuous phase. We propose a hypothesis that rapid solvent transfer has two advantages on the STrIPS process *i*. the rapid interfacial tension evolution and *ii*. in-situ particle modification to attain amphiphilic nature. We investigate both interfacial tension evolution and in-situ particle modification with a series of experiments involving tensiometry, confocal, and scanning

electron microscopy. Also, experimental data is validated with complementary simulation studies. A comprehensive study of different parameters has been done including composition, surfactant concentration, salt, and postprocessing to establish a bijel structural-functional relationship. Finally, we also examine the scalability potential of uniform domain size bijels and conclude that screening a set of parameters enables higher control over the bijel structure and allows the variation of domain size of the bijel system for tailored applications.

Bijels are particle-stabilized liquid networks that allow the catalytic, electrical, and magnetic characteristics of solids to permeate through the entire volume of the material. Because of the high interfacial area along the trickling liquids, these characteristics multiply several times in scaled-up applications.[79] Next, ***Chapter 4*** is focused on the functional aspect of the bijel by introducing the catalytic property to the solid interface between immiscible liquids. Since Pickering emulsions have been utilized as microreactors, interfacial reactions have undergone a significant transformation. Particle-stabilized emulsions have contributed significantly towards green chemistry by practicing the reduction (solvents, waste), reuse (catalytic particles and enzymes), and recycling (easy recycling of solid particles).[80] To address the current limitation of batch processing of reactions in Pickering emulsions, we propose using bijel as microreactors in which liquids can selectively supply and continuously remove the chemicals. As proposed in 2005 with the inception of bijel material, it should be possible with two liquid channels to use the bijels as microreactors[50] but there are practical challenges to address. The conventional method of bijel fabrication, in particular, is limited by solvent selection and functional catalysts to support the interfacial reactions and is limited to a small number of reactions.[81, 82] We propose that bijel stabilized with alumina functionalized particles can be used as a reactor for epoxidation reaction at the oil-water interface. Aiming this we discuss three adopted routes *i*. use alumina particles as bijel stabilizers, *ii*. add some alumina particles (as a particle dopant) in the silica precursor mixture, and *iii*. interfacial coating of alumina on silica particles. First, we investigate alumina bijel fabrication using alumina particles as stabilizers, and we show a detailed discussion of various structural dependencies. Following that, we examine the effect of alumina particle doping in the silica nanoparticle precursor mixture on the stability of the precursor mixture and the resulting bijel structure. Finally, we discuss preliminary experiments of alumina interfacial coating and characterization at the silica interface. Although all three methods yield promising results for alumina bijel fabrication, more qualitative and quantitative characterization of the functionalized interface is required. To assess the structural-functional relationship of alumina bijels in terms of fabrication methods and corresponding dependencies, we must test their catalytic efficiency in the epoxidation reaction.

1.5 Bibliography

[1] W. Ramsden, F. Gotch, Proceedings of the Royal Society of London 1904, 72, 477.
[2] S. U. Pickering, J. Chem. Soc., Trans. 1907, 91, 2001.
[3] A. Bala Subramaniam, M. Abkarian, L. Mahadevan, H. A. Stone, Nature 2005, 438, 930.
[4] K. Stratford, R. Adhikari, I. Pagonabarraga, J. C. Desplat, M. E. Cates, Science 2005, 309, 2198.
[5] B. Remant, B. Thapa, P. Xu, Molecular Pharmaceutics 2012, 9, 2719.
[6] A. M. Bago Rodriguez, B. P. Binks, Current Opinion in Colloid & Interface Science 2019, 44, 107.
[7] J. Pu, Z. Shen, C. Zhong, Q. Zhou, J. Liu, J. Zhu, H. Zhang, Advanced Materials 2020, 32, 1903808.
[8] J. A. Witt, D. R. Mumm, A. Mohraz, Journal of Materials Chemistry A 2016, 4, 1000.
[9] H. A. Barnes, J. F. Hutton, K. Walters, *An introduction to rheology*, Vol. 3, Elsevier, 1989.
[10] H. A. Barnes, Journal of Non-Newtonian Fluid Mechanics 1999, 81, 133.
[11] J. O. Hirschfelder, *Intermolecular Forces, Volume 12*, Vol. 12, John Wiley & Sons, 2009.
[12] C. V. Boys, *Soap bubbles, their colours and the forces which mold them*, Vol. 542, Courier Corporation, 1959.
[13] J. J. Jasper, Journal of Physical and Chemical Reference Data 1972, 1, 841.
[14] J. G. Kirkwood, F. P. Buff, The Journal of Chemical Physics 1949, 17, 338.
[15] D. E. Tambe, M. M. Sharma, Journal of Colloid and Interface Science 1994.
[16] B. P. Binks, S. O. Lumsdon, Physical Chemistry Chemical Physics 1999, 1, 3007.
[17] J. Israelachvili, Colloids and Surfaces A: Physicochemical and Engineering Aspects 1994, 91, 1.
[18] G. K. Voeltz, W. A. Prinz, Nature Reviews Molecular Cell Biology 2007, 8, 258.
[19] A. S. Rudolph, B. R. Ratna, B. Kahn, Nature 1991, 352, 52.
[20] J. Forth, X. Liu, J. Hasnain, A. Toor, K. Miszta, S. Shi, P. L. Geissler, T. Emrick, B. A. Helms, T. P. Russell, Advanced Materials 2018, 30.
[21] G. Xie, J. Forth, Y. Chai, P. D. Ashby, B. A. Helms, T. P. Russell, Chem 2019, 5, 2678.
[22] D. Dendukuri, P. S. Doyle, Advanced Materials 2009, 21, 4071.
[23] P. S. Clegg, E. M. Herzig, A. B. Schofield, S. U. Egelhaaf, T. S. Horozov, B. P. Binks, M. E. Cates, W. C. K. Poon, Langmuir 2007, 23, 5984.
[24] D. Lee, D. A. Weitz, Small 2009.
[25] A. R. Studart, H. C. Shum, D. A. Weitz, The Journal of Physical Chemistry B 2009, 113, 3914.
[26] T. Merkel, V. Gräf, E. Walz, H. P. Schuchmann, Chemical Engineering & Technology 2015, 38, 1490.
[27] Y. Renardy, V. Cristini, J. Li, International Journal of Multiphase Flow 2002, 28, 1125.
[28] H. Xu, S. Melle, K. Golemanov, G. Fuller, Langmuir 2005.
[29] X. Liu, S. Shi, Y. Li, J. Forth, D. Wang, T. P. Russell, Angewandte Chemie International Edition 2017, 56, 12594.
[30] B. M. Oosterlaken, G. de With, Accounts of Materials Research 2022, 3, 894.
[31] K. Hill, O. Rhode, Lipid / Fett 1999, 101, 25.
[32] M. Nitschke, S. S. e. Silva, Critical Reviews in Food Science and Nutrition 2018, 58, 631.
[33] I. Kralova, J. Sjöblom, Journal of Dispersion Science and Technology 2009, 30, 1363.
[34] D. Guzey, D. J. McClements, Advances in Colloid and Interface Science 2006, 128-130, 227.
[35] M. C. Fuerstenau, J. Graeme, R. H. Yoon, Society for Mining, Metallurgy, and exploration, Inc., 2007.
[36] I. Akartuna, E. Tervoort, A. R. Studart, L. J. Gauckler, Langmuir 2009.
[37] M. Chappat, Colloids and Surfaces A: Physicochemical and Engineering Aspects 1994, 91, 57.

[38] M. Fingas, B. Fieldhouse, Journal of Hazardous Materials 2004, 107, 37.
[39] K. Y. Yoon, H. A. Son, S. K. Choi, J. W. Kim, W. M. Sung, H. T. Kim, Energy and Fuels 2016, 30, 2628.
[40] B. P. Binks, J. A. Rodrigues, W. J. Frith, Langmuir 2007.
[41] R. Aveyard, B. P. Binks, J. H. Clint, Advances in Colloid and Interface Science 2003, 100-102, 503.
[42] B. P. Binks, Current Opinion in Colloid & Interface Science 2002, 7, 21.
[43] A. Koretsky, P. Kruglyakov, Izv. Sib. Otd. Akad. Nauk USSR 1971, 2, 139.
[44] B. P. Binks, Current Opinion in Colloid & Interface Science 2002, 7, 21.
[45] T. Young, Philosophical Transactions of the Royal Society of London 1805, 95, 65.
[46] R. Aveyard, J. H. Clint, Journal of the Chemical Society, Faraday Transactions 1996, 92, 85.
[47] A. F. Koretsky, P. M. Kruglyakov, Izv. Sib. Otd. Akad. Nauk USSR 1971, 2, 139.
[48] A. Stocco, M. Nobili, Advances in colloid and interface science 2017, 247, 223.
[49] H. Fan, A. Striolo, Physical Review E 2012, 86, 051610.
[50] K. Stratford, R. Adhikari, I. Pagonabarraga, J.-C. Desplat, M. E. Cates, Science 2005, 309, 2198.
[51] R. Aveyard, J. H. Clint, D. Nees, Colloid and Polymer Science 2000, 278, 155.
[52] S. Frijters, F. Günther, J. Harting, Soft Matter 2012, 8, 6542.
[53] S. Razavi, K. D. Cao, B. Lin, K. Y. C. Lee, R. S. Tu, I. Kretzschmar, Langmuir 2015, 31, 7764.
[54] A. Imhof, D. Pine, Nature 1997, 389, 948.
[55] B. K. Debnath, U. K. Saha, N. Sahoo, Renewable and Sustainable Energy Reviews 2015, 42, 196.
[56] N. R. Cameron, Polymer 2005, 46, 1439.
[57] R. Mezzenga, J. Ruokolainen, G. H. Fredrickson, E. J. Kramer, D. Moses, A. J. Heeger, O. Ikkala, Science 2003, 299, 1872.
[58] C. Linke, S. Drusch, Critical reviews in food science and nutrition 2018, 58, 1971.
[59] H. j. Werner, V. Z-H Chan, J. Hoffman, V. Y. Lee, H. Iatrou, A. Avgeropoulos, N. Hadjichristidis, R. D. Miller, E. L. Thomas, J. Chem. Soc. Faraday Trans. 93 1996.
[60] W. Feng, Y. Chai, J. Forth, P. D. Ashby, T. P. Russell, B. A. Helms, Nature Communications 2019, 10, 1095.
[61] Y. He, Y. Wu, J.-z. Fu, Q. Gao, J.-j. Qiu, Electroanalysis 2016, 28, 1658.
[62] S. A. F. Bon, S. D. Mookhoek, P. J. Colver, H. R. Fischer, S. van der Zwaag, European Polymer Journal 2007, 43, 4839.
[63] M. Cui, T. Emrick, T. P. Russell, Science 2013.
[64] S. P. Nunes, T. Inoue, Journal of Membrane Science 1996, 111, 93.
[65] S. A. Vitale, J. L. Katz, Langmuir 2003, 19, 4105.
[66] L. Li, C. Miesch, P. K. Sudeep, A. C. Balazs, T. Emrick, T. P. Russell, R. C. Hayward, Nano Letters 2011, 11, 1997.
[67] M. Reeves, K. Stratford, J. H. J. Thijssen, Soft Matter 2016, 12, 4082.
[68] J. S. Huang, W. I. Goldburg, A. W. Bjerkaas, Physical Review Letters 1974, 32, 921.
[69] T. Izumitani, T. Hashimoto, The Journal of chemical physics 1985, 83, 3694.
[70] E. M. Herzig, K. A. White, A. B. Schofield, W. C. K. Poon, P. S. Clegg, Nature Materials 2007, 6, 966.
[71] M. N. Lee, A. Mohraz, Advanced Materials 2010, 22, 4836.
[72] J. W. Tavacoli, J. H. Thijssen, A. B. Schofield, P. S. Clegg, Advanced Functional Materials 2011, 21, 2020.
[73] H. Firoozmand, D. Rousseau, Food Hydrocolloids 2015, 48, 208.
[74] T. J. Thorson, E. L. Botvinick, A. Mohraz, ACS Biomaterials Science & Engineering 2018, 4, 587.
[75] K. M. McDevitt, T. J. Thorson, E. L. Botvinick, D. R. Mumm, A. Mohraz, Materialia 2019, 7, 100393.

[76] E. M. Herzig, K. White, A. B. Schofield, W. C. Poon, P. S. Clegg, Nature materials 2007, 6, 966.
[77] M. F. Haase, K. J. Stebe, D. Lee, Advanced Materials 2015, 27, 7065.
[78] M. A. Khan, A. J. Sprockel, K. A. Macmillan, M. T. Alting, S. P. Kharal, S. Boakye-Ansah, M. F. Haase, Advanced Materials 2022, 34, 2109547.
[79] P. S. Clegg, *Bijels: Bicontinuous Particle-stabilized Emulsions*, Vol. 10, Royal Society of Chemistry, 2020.
[80] M. Pera-Titus, L. Leclercq, J.-M. Clacens, F. De Campo, V. Nardello-Rataj, Angewandte Chemie International Edition 2015, 54, 2006.
[81] G. Di Vitantonio, T. Wang, M. F. Haase, K. J. Stebe, D. Lee, ACS Nano 2018, 13, 26.
[82] S. Cha, H. G. Lim, M. F. Haase, K. J. Stebe, G. Y. Jung, D. Lee, Scientific Reports 2019, 9, 6363.

Chapter 2

Shaping Liquids

Abstract: Droplets are spherical due to the principle of interfacial energy minimization. Here, we show that nonequilibrium droplet shapes can be stabilized via the interfacial crosslinking of nanoparticles. This principle allows for the stability of practically infinitely long liquid tubules and monodisperse cylindrical droplets. Droplets of oil-in-water are elongated via gravitational or hydrodynamic forces at a reduced interfacial tension. Silica nanoparticles self-assemble and cross-link on the interface triggered by the synergistic surface modification with hexyltrimethylammonium and trivalent lanthanum cations. The droplet length dependence is described by a scaling relationship and the rate of nanoparticle deposition on the droplets is estimated. Our approach potentially enables the 3D-printing of Newtonian fluids, broadening the array of material options for additive manufacturing techniques

This chapter is based on Khan, Mohd A., and Martin F. Haase. "Stabilizing liquid drops in nonequilibrium shapes by the interfacial crosslinking of nanoparticles." *Soft Matter* 17.8 (2021): 2034-2041.

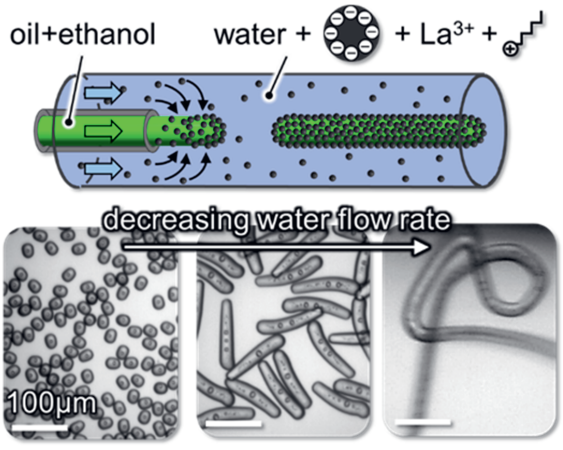

2.1 Introduction

The dripping of water from a faucet is an everyday life example of an interfacial phenomenon. Gravity pulls the droplet down, but surface tension "glues" it to the faucet. When the inflowing water grows the pendant droplet to a critical size, surface tension cannot hold it anymore. The droplet breaks off via the Plateau-Rayleigh instability.[1] Understanding the underlying physics of this process is essential for technologies such as ink-jet printing.

Recent work by Liu et al. shows that the Plateau Rayleigh instability can be completely suppressed, and instead of droplets, stable liquid tubules are formed. This apparent violation of the surface energy minimization principle is possible because a rigid skin forms on the droplet. In their work, cellulose nanocrystals interact with polymer surfactants, causing them to attach to the droplets. The resulting cellulose nanocrystal surfactants adhere so strongly to the droplet interface that they mechanically jam.[2] The shaping of liquids based on interfacial jamming was further explored by Forth et al. to print water into various tubular arrangements within a viscous oil phase.[3]

The possibility to 3D-print Newtonian fluids such as water into different shapes can complement the existing additive manufacturing techniques. Conventional 3D-printing requires yield stress fluids such as polymer melts, metals, or ceramic suspensions as printing materials. Printing yield-stress fluids layer-by-layer followed by solidification allows to fabricate complicated shapes or geometries that would be otherwise impossible to construct by hand. More research is needed to facilitate similar precision printing for Newtonian fluids, but the printing of liquids has already facilitated the construction of devices that are not possible with conventional additive manufacturing techniques. Examples are all-liquid fluidic devices [4] and flow-through-coordinated reaction systems.[5]

Shaping liquids via interfacial jamming also enables the fabrication of droplets with anisotropic shapes with potential applications as reinforcements for structural materials[6], drug delivery vehicles[7] or as photonic crystals.[8] Rigid interfacial assemblies of solid particles have previously been used to stabilize droplets of anisotropic shapes by squeezing droplets through capillaries[9], compression of droplets between plates[10], partial droplet coalescence[11], droplet elongation by electric fields[12], controlled droplet shearing[13], droplet deformation via mechanical tools[14], and shaping of droplets in molds.[15]

In this chapter, we discuss a new technique to generate liquid tubules and droplets of anisotropic shapes. We argue that the nonequilibrium droplet shapes are not stabilized by interfacial jamming[2, 12, 16], but instead by interfacial crosslinking of nanoparticles.

We distinguish these two terms as follows: An interfacially jammed film is composed of densely packed particles with the individual particles adhering so strongly to the interface that their removal is virtually impossible. Reducing the volume of a droplet covered by an interfacially jammed film results in the

buckling of the interface, as the strong attachment of the particles conserves the overall surface area of the droplet. In an interfacially cross-linked film, the particles do not necessarily adhere strongly to the interface but are connected to each other laterally via chemical forces. Reduction of the droplet volume with an interfacially cross-linked film can result in partial detachment of the particles but the rigidity of the remaining film facilitates out-of-equilibrium droplet shapes.

To realize interfacial crosslinking, we previously used tri valent lanthanum cations (La^{3+}) to electrostatically bind interfacially attached particles to each other[17]. Here, we show that interfacial crosslinking allows for the stabilization of nonspherical droplets by flowing a mixture of oil and ethanol through a small needle into an aqueous phase containing silica nanoparticles (SNP), hexyltrimethylammonium (HTA^+) cations and La^{3+}. Pendant drop tensiometry shows that HTA^+ and La^{3+} act synergistically in generating a rigid interfacial assembly of the nanoparticles. We show that the formation of liquid tubules requires a lowering of the interfacial tension, which in our system is facilitated by mass transfer of ethanol from oil to water. Based on our experimental analysis, we demonstrate that liquid tubules can be generated via the action of gravitational forces and monodisperse droplets of anisotropic shape via controlled shear stresses in a microfluidic device. Finally, we describe the mechanics of anisotropic droplet formation with a previously introduced shear stress equation[18] and approximate the interfacial nanoparticle deposition rate.

2.2 Results and Discussion

2.2.1 Interfacial attachment and crosslinking by HTA+ and La3+ modification of SNP

Fig. 2.1a schematically depicts the experimental setup employed to study liquid tubule formation. A mixture of diethyl phthalate (DEP) containing 20 vol % ethanol is flown through a small needle (260 µm inner diameter) into stagnant water containing 5 *wt*-% SNP (Ludox TM, 20 – 30 nm particle diameter), 10 mM hexyltrimethylammonium cations (HTA^+), and variable concentrations of trivalent lanthanum cations (La^{3+}). Fig 2. 1(b) shows photographs of the resulting two-phase-flow at a constant flowrate of 15 ml/hr for different La^{3+} concentrations in the aqueous phase.

Increasing the La^{3+} concentration in the aqueous phase results in a gradual transition from spherical droplets forming below 0.2 mM La^{3+}, to tadpole shaped droplets forming between 0.4 – 0.6 mM, to a liquid tubule forming above 0.8 mM La^{3+}. [19]

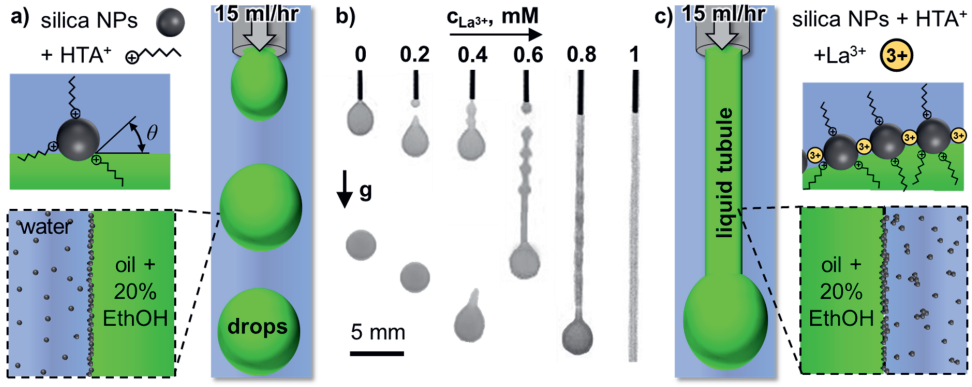

Fig. 2.1 Liquid tubule stabilization by La^{3+} mediated interfacial silica nanoparticle crosslinking. (a) Schematic depiction of the experimental setup, nanoparticle surface modification by hexyltrimethylammonium cations (HTA^+), and their interfacial assembly (not drawn to scale), (b) Photographs of two-phase liquid behavior at different La^{3+} concentrations in the aqueous phase at a constant flowrate of oil+20% ethanol of 15 ml/hr, (c) Schematic depiction of liquid tubule formation and interfacial crosslinking of HTA^+ modified silica nanoparticles with La^{3+} cations.

Why does the increase of the La^{3+} concentration result in this remarkably different two-phase flow behavior? In the following, we attempt to answer this question based on additional experiments. First, we demonstrate the interfacial behavior of the HTA^+ and La^{3+} surface modification of the SNP qualitatively based on testing the foam stability. To this end, we prepare solutions and dispersions of the individual components, as well as their mixtures. These are shown as photographs in Fig. 2.2, taken immediately after vigorous shaking.

Neither the dispersion of 5 *wt*-% SNP (A), nor the solution of 100 mM HTA^+ (B) shows any stable foam phase, indicating that both components alone are not interfacially active. However, the mixture of both (5 *wt*-% SNP, 10 mM HTA^+) shows a foam layer that remains stable for several minutes (Fig. 2.2, A+B). This can be explained as follows. Both, the negatively charged SNP and the HTA^+ cations are hydrophilic and therefore remain in the water phase. However, in the mixture, HTA^+ renders the SNP surface active, as it adsorbs electrostatically on silica, covering the surface partially with hexyl-chains in-situ.[20] This is confirmed by measurements of the contact angles of sessile water droplets on flat HTA^+ modified silica surfaces, which show decreasing hydrophilicity of the surface.[21]

The HTA^+ adsorption on the SNP increases their interfacial attachment energy, given by

$$\Delta G_{attach} = \pi \cdot r^2 \cdot \gamma_{ow}(1 \pm \cos\theta)^2 \qquad (1)$$

with r the particle radius, γ_{ow} the water/oil interfacial tension, and θ the contact angle.[22]

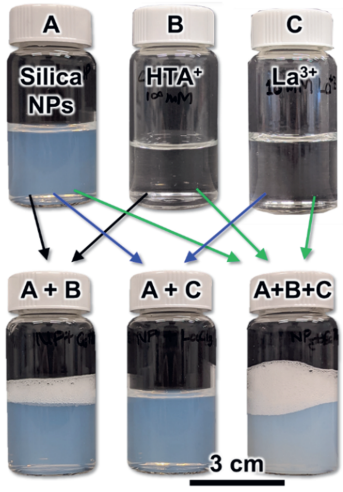

Fig. 2.2 Foam stability test with silica nanoparticles (Ludox TM), hexyltrimethylammonium- (HTA^+) and lanthanum cations (La^{3+}). The photographs show aqueous dispersions and solutions before (top row) and after mixing (bottom row). All photographs were taken immediately after vigorously shaking the vials.

For particles of 10 nm radius, ΔG can reach several hundred times the thermal energy of the particles (in kT), resulting in a densely packed self-assembled particle monolayer at the air/water interface, stabilizing the foam in Figure 2(A+B).[23, 24]

The second component influencing the interfacial assembly of the SNP in our experiments is La^{3+} cations. Fig. 2.2 shows that neither a solution of La^{3+} (C), nor a mixture of the SNP with 1 mM La^{3+} (A+C, 5 *wt*-% silica, 1 mM La^{3+}) allows for a stable foam formation. However, the mixture containing the SNP, 10 mM HTA^+ and 1 mM La^{3+} (A+B+C) shows a stable foam, which even exceeds the height of the foam layer formed with SNP + 10mM HTA^+ (A+B). This indicates that HTA^+ and La^{3+} act synergistically in enhancing the SNP surface activity. The slightly cloudier appearance of the mixture SNP + HTA^+ + La^{3+} (A+B+C) indicates that particle aggregation has occurred. We analyze the colloidal stability of the SNP next. Fig. 2.3 shows zeta potential and dynamic light scattering data for aqueous SNP dispersions at different La^{3+} concentrations.

The zeta potential of the SNP in the absence of La^{3+} is -40 mV. As the La^{3+} concentration increases to 1 mM, the zeta potential increases to -10 mV. La^{3+} ions adsorb specifically on the negatively charged particles, reducing the zeta potential due to ion pairing with the deprotonated silanol groups. The decrease of the negative zeta potential results in partial aggregation of the particles as shown by the increase in the intensity averaged dynamic light scattering (DLS) signal from 30 nm to 75 nm (Fig. 2.3, secondary y-axis).

Fig. 2.4 shows that above 0.2 mM the particle size distributions become bimodal, with a second peak at around 100 nm. The particles flocculate strongly above 1 mM La^{3+}. In contrast, DLS measurements show that HTA^+ causes only minor aggregation with an increase of the intensity averaged size to 40 nm at 10 mM HTA^+ (Fig 2.5).

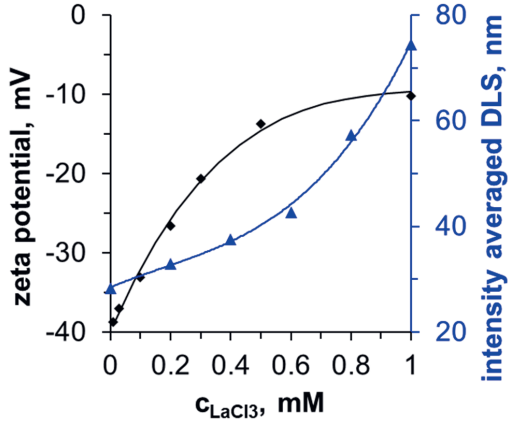

Fig. 2.3 Colloidal stability of Ludox-TM in dependence of the La^{3+} concentration (pH 9). The corresponding DLS polydispersity index range from 0.18 (0 mM)-0.48 (1 mM)

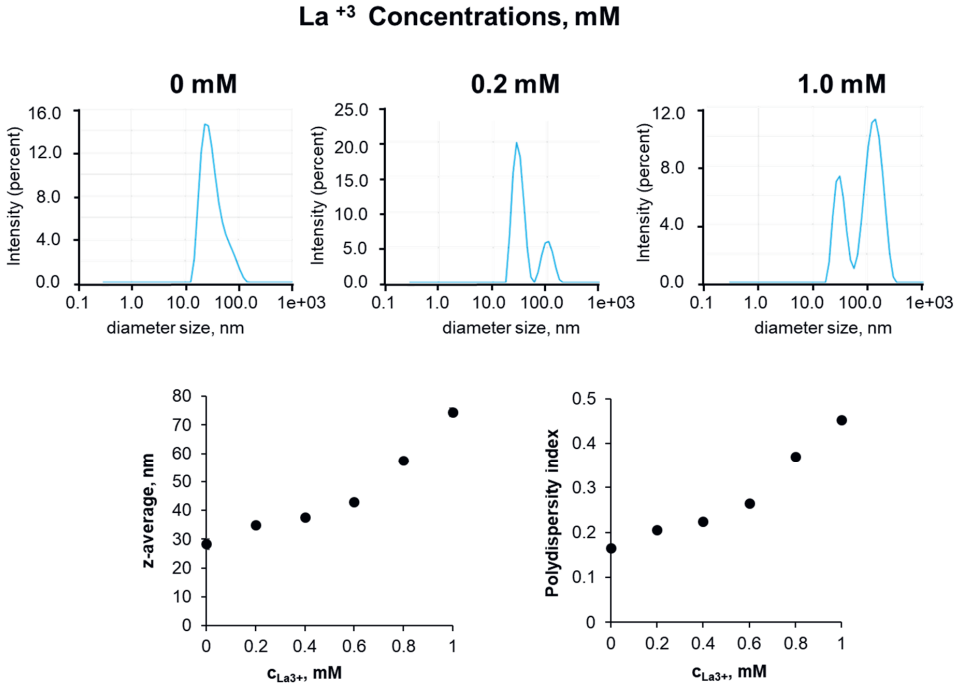

Fig 2.4 Dynamic light scattering measurements of Ludox TMA particles (5 *wt*%) at different concentrations of La^{+3}.

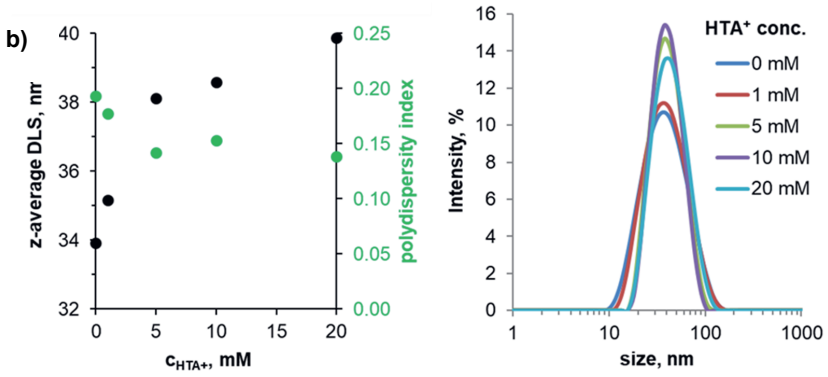

Fig 2.5 Zeta potential and dynamic light scattering measurements of Ludox TMA particles (5 *wt*%) at different concentrations of HTA^+.

The flocculation of the particles can be attributed to La^{3+} mediated cross-linking. Prior studies have found that the La^{3+} induced flocculation of SNP enhances emulsion stability and cryo-SEM images revealed the interfacial assembly of the particles.[25, 26] However, for liquid tubules to form in our experiments, the simultaneous adsorption of 1 mM La^{3+} and 10 mM HTA^+ on the SNP is required (see Fig. 2.1).

Which properties of the HTA^+ and La^{3+} induced interfacial SNP assembly to enable the droplet deformation away from a spherical shape? We explore this in the following based on pendant drop tensiometry. Fig. 2.5a shows photographs of pure DEP droplets hanging on dispensing needles in different aqueous phases. We rapidly withdraw a DEP volume ΔV into the syringe to reduce the droplet area by 50%.

Upon withdrawing DEP from a pendant droplet in a SNP dispersion containing 10 mM HTA^+, the droplet becomes more spherical (Fig. 2.6a, top row). This occurs since the gravitational force on the droplet decreases and the interfacial tension becomes more dominant in the force balance. The same happens when DEP is withdrawn from a droplet in a SNP dispersion with 1 mM La^{3+} (Fig. 2.6a middle row). In sharp contrast, when the droplet volume is reduced in a SNP dispersion containing 10 mM HTA^+ and 1 mM La^{3+}, the droplet shape becomes less spherical and rather ellipsoidal (Fig. 2.6a, middle row). The counterintuitive shape change results from the rigid nature of the self-assembled nanoparticle coating on the droplet, as discussed in the following.

Fig. 2.6b plots the measurements of the droplet volume and interfacial tension γ during the shape change of the droplet shown in the middle row of Fig. 2.6a Before the shape change, γ is ~ 15 mN/m, slightly below the interfacial tension of pure water and DEP (~16 mN/m).

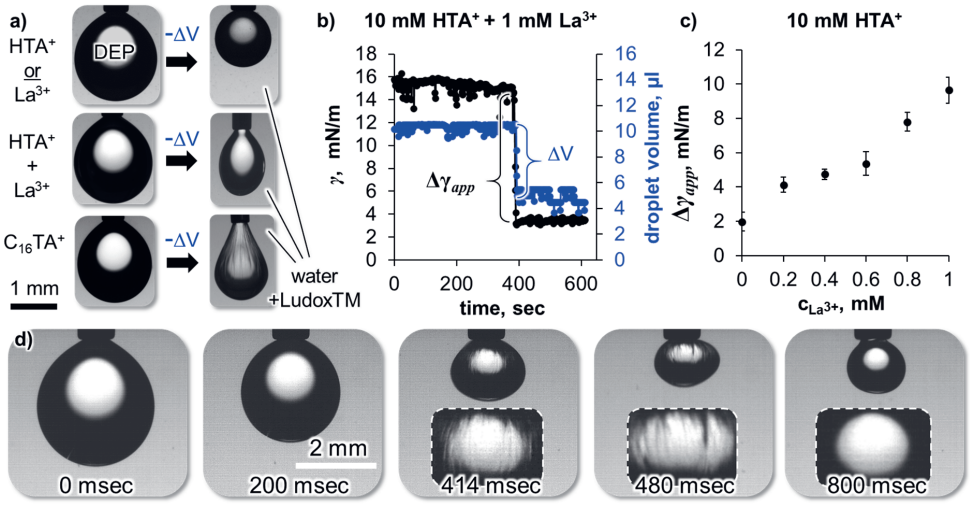

Fig. 2.6 Effect of surface area reduction on droplet shape and apparent interfacial tension reduction ($\Delta\gamma_{app}$). (a) Photographs of DEP droplets in different aqueous phases before and after droplet area reduction by 50 %, (b) Droplet volume and interfacial tension from pendant drop shape analysis against time before, during and after the droplet area reduction, (c) Apparent interfacial tension reduction against La^{3+} concentration. (d) 90% volume reduction of a DEP droplet in a Ludox TM dispersion containing 10 mM HTA^+ and 1 mM La^{3+} (SI video 2 [19]) plots $\Delta\gamma_{app}$ for the DEP droplet volume reduction in a SNP dispersion containing 10 mM HTA^+ as a function of the La^{3+} concentration.

Upon volume reduction, the software of the pendant drop tensiometer interprets the shape change as a reduction of the interfacial tension. To the software, the ellipsoidal shape indicates that gravity is strong enough to elongate the droplet against the surface tension. However, a lowering of the surface tension seems unlikely in our experiment, as there is no change in the chemical composition during the droplet volume reduction. Therefore, we will call the measured interfacial tension change here "apparent interfacial tension change", or $\Delta\gamma_{app}$.

We find that $\Delta\gamma_{app}$ is independent of the droplet age, indicating that the interfacial assembly of the nanoparticles takes place on faster timescales than the timescales of the experiment (~ 18 seconds). $\Delta\gamma_{app}$ increases with increasing La^{3+} concentration, or in other words the droplet shapes become more ellipsoidal.

To understand this further, we show in the bottom row of Fig. 2.6a the droplet shape change in a SNP dispersion containing 1 mM hexadecyltrimethylammonium cations ($C_{16}TA^+$). Upon volume reduction, the droplet also deforms in the $C_{16}TA^+$ system. However, this time permanent wrinkles can be observed on the surface of the droplet. Such wrinkles[27-29] have been previously found for particle coated pendant

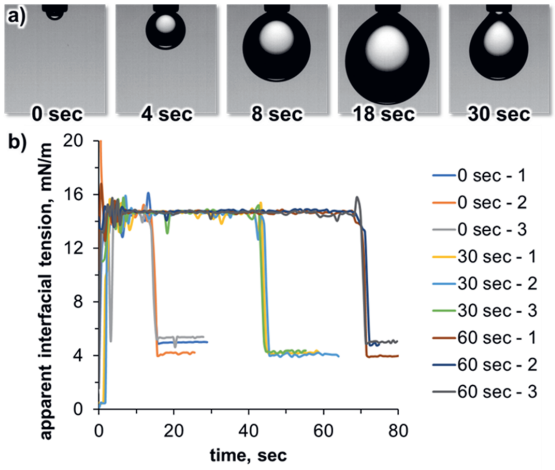

Fig. 2.7 Droplet shrinking experiment for different droplet aging times. a) Photograph time series showing the inflation of a droplet over a duration of ~18 seconds (final volume 15 µl), followed immediately by volume reduction (10 µl) for ~10 seconds. b) Measurement of the apparent interfacial tension for different droplets. The legend shows the aging time of the droplet after the completion of the inflation before the volume reduction is initialized.

droplets[10, 12]. Upon droplet area reduction, the particle monolayer buckles due to interfacial jamming of the particles, resulting in wrinkles.

Why does a volume reduction of the droplets in the SNP dispersion containing 1 mM $C_{16}TA^+$ result in wrinkles, but no wrinkles are observed for the same volume reduction in a SNP dispersion containing 10 mM HTA^+ and 1 mM La^{3+}? We believe that the different behaviors show that the $C_{16}TA^+$ modified particles are interfacially jammed, while the $HTA^+ + La^{3+}$ modified particles are interfacially cross-linked (and not jammed). We explain our interpretation in the following.

As mentioned in the introduction, particles jam on an interface because their high attachment energy does not allow them to escape to the bulk when they experience lateral forces. By using $C_{16}TA^+$ in the aqueous phase, long hydrocarbon chains adsorb on the particles. This results in a high contact angle θ. We do not have precise measurements for the contact angle as this requires advanced electron microscopy characterization[30]. However, we estimate that $C_{16}TA^+$ modified Ludox TM particles have contact angles close to 90°, as they have previously been employed for the stabilization of bijels[31], which requires a contact angle of 90°. With the interfacial tension between DEP and water, the Ludox TM particle radius of 10 nm and $\theta = 90°$, ΔG_{attach} equals to -1220kT (with the Boltzmann constant k and the absolute temperature T). In other words, the particles are 1220 times stronger attached than their

thermal energy to allow them to escape. This high attachment energy forces the particles to stay at the interface when the droplet volume is reduced. Since the particles occupy a fixed area on the droplet, the interface must buckle to accommodate the interfacial particle coverage.

In contrast, the particles modified with 10 mM HTA^+ and 1 mM La^{3+} have a lower contact angle, as the hexyl chain of the HTA^+ and the lower HTA^+ adsorption density does not impart much hydrophobicity to the particles. Macroscopic θ measurements of a sessile water droplet on a flat silica surface give a value of $\theta = 40°$ at a pH value of 9.[21] It is unlikely that La^{3+} increases the contact angle significantly, as it does not introduce apolar chemical groups to the surface of the particles. For $\theta = 40°$, ΔG_{attach} calculates to -66.9 kT. Based on this, the HTA^++ La^{3+} modified particles can detach more easily from the pendant droplet upon volume reduction. To test this hypothesis, we have reduced the volume of the droplet by ~ 90% in Fig 4d (see also SI-video 2[19, 32])

The experiment shows that wrinkles can be observed for a duration of 400 milliseconds during the droplet volume reduction in the presence of Ludox modified with 10 mM HTA^+ and 1 mM La^{3+}. Shortly after, the wrinkles disappear, demonstrating that the particles have detached from the interface. We therefore conclude that HTA^+ and La^{3+} modified particles are not interfacially jammed, as they can leave the interface (likely as aggregated clusters or sheets). However, the La^{3+} mediated crosslinking of the remaining particles at the interface provides rigidity, allowing the stabilization of out-of-equilibrium droplet shapes.

2.2.2 Interfacial tension reduction by ethanol addition to the droplet phase

After analyzing the nanoparticle assembly on the oil/water interface, we next investigate the role of ethanol in the oil phase Fig 2.8a shows photographs of injecting DEP with variable ethanol volume fractions into a 5 *wt*-% Ludox TM nanoparticle dispersion with 10 mM HTA^+ and 1 mM La^{3+} (see also SI-video 3[19]).

Injecting pure DEP or DEP containing 5 vol-% ethanol results in dripping of spherical droplets. At 10 vol-%, tadpole-like droplets pinch-off periodically from the dispensing needle. Once the ethanol content in DEP reaches 15 vol-%, a liquid tubule with periodic bulges forms. Above 20 vol-% ethanol in DEP the liquid tubule has a flat surface, indicating that the Plateau-Rayleigh instability has been completely suppressed.The transition from dripping to liquid tubule formation is correlated with a reduction of the interfacial tension. We arrive at this conclusion based on the effect of the ethanol fraction in DEP on the size of the formed droplets. When increasing from 0 to 10 vol-% ethanol in DEP the pinch off droplet size decreases gradually from 2 mm to 1.6 mm (see Appendix).

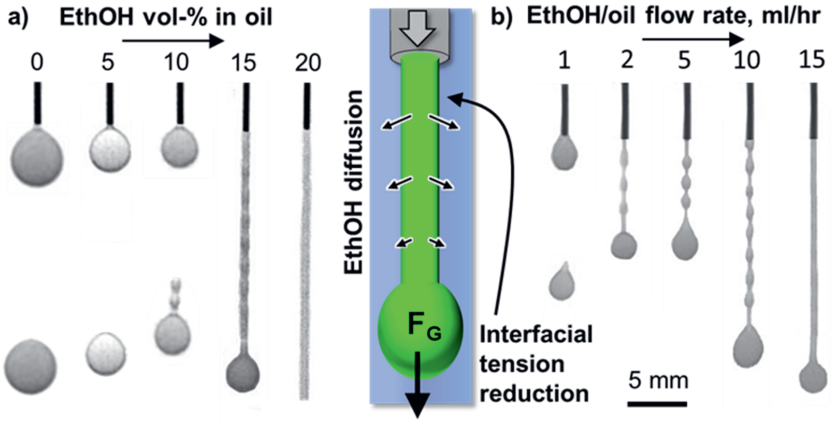

Fig. 2.8 Liquid tubule formation facilitated by ethanol diffusion induced interfacial tension reduction. (a) Photographs showing the two-phase flow upon injecting a mixture of oil (DEP) with variable ethanol vol-% at 15 ml/hr through a dispensing needle into an aqueous dispersion of Ludox TM nanoparticles with dissolved 10 mM HTA^+ and 1 mM La^{3+}. Right: Schematic depiction of liquid tubule formation at 20 vol-% ethanol in DEP. (b) Liquid tubule formation with 20 vol-% EtOH in DEP for different flow rates (5 *wt*-% SNP, 10 mM HTA^+, 1 mM La^{3+}).

This trend continues for the liquid tubules formed from 15 to 20 vol-% ethanol in DEP, for which the diameter of the droplet at the tubule front decreases from 1.4 mm to 1.1 mm. This means, a lower gravitational force During liquid tubule formation, ethanol diffuses from DEP to the surrounding water, lowering the interfacial tension locally. Increasing the ethanol content in water from 0 – 40 vol-% reduces the interfacial tension between pure DEP and water from 16 mN/m to 2 mN/m (Fig 2.8b).

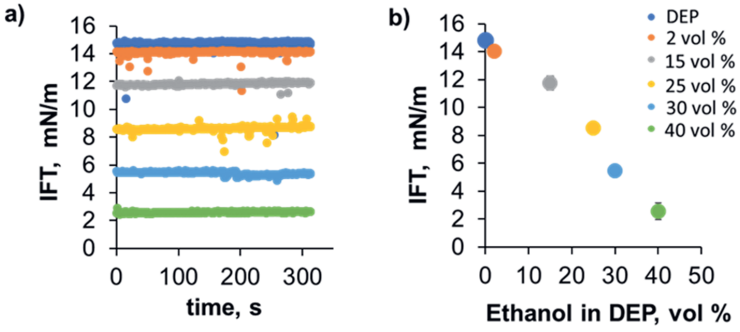

Fig. 2.9 Depicts the effect of surface tension on liquid fiber formation. a) Time dependant measurement of interfacial tension (γ) of DEP-water interface with different ethanol volume % ($\varphi_{ethanol}$). b) Equilibrium interfacial tension measurement with varying $\varphi_{ethanol}$.

15 ml/hr is required to pinch the droplet off, or for ethanol contents above 15 vol-%, to pull the liquid tubule. This finding analogous to the observation of Liu et al [2], where liquid tubule formation is made possible by a polymeric surfactant lowering the interfacial tension.

Fig. 2.8b shows liquid tubule formation in dependence of the flow rate of a mixture of 20% ethanol in DEP (see also SI-video 4 [19]). At 1 ml/hr, dripping occurs. Between 2 – 10 ml/hr a liquid tubule with "beads on a string" like pattern forms. Above 15 ml/hr a continuous cylindrical liquid tubule is generated. The origin of this transition has not been analyzed here in the current study and is subject to further work.

2.2.3 Microfluidic generation of elongated droplets

In the last part of this paper, the principles of droplet elongation by interfacial tension reduction and interfacial rigidification will be used to generate nonspherical droplets in a microfluidic device as depicted in Fig. 2.10a. A perfluorooctyltriethoxysilane coated glass capillary is centered inside a second larger glass capillary. We flow a mixture of ethanol and DEP at a constant rate out of the first capillary

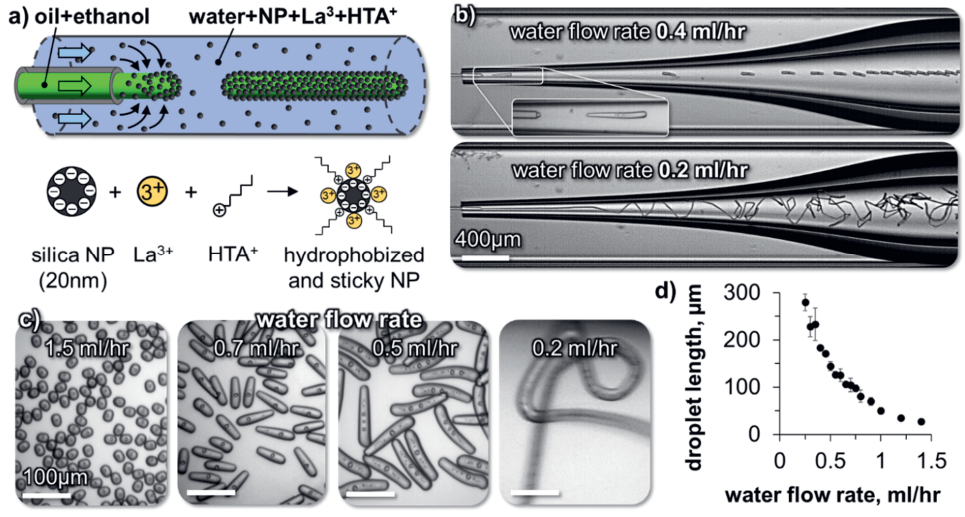

Fig. 2.10 Liquid tubule formation and droplet elongation. (a) Schematics of droplet extrusion and nanoparticle surface modification. (b) Micrographs of elongated droplet and liquid tubule formation. The DEP droplets include internal water droplets which have been formed by phase separation of water, which was taken up by the droplet during the ethanol diffusion, as described in ref [33]. (c) Micrographs of collected droplets and fiber. (d) Droplet length dependence on water flow rate.

into the second capillary.In the second capillary, an aqueous phase of 5 *wt*-% SNP, 10 mM HTA^+ and 1 mM La^{3+} flows at variable rates. Fig. 2.10b shows snapshots of high-speed video microscopy of the droplet elongation for two different flow rates of the aqueous phase. At an aqueous phase flow rate of 0.4 ml/hr, short cylindrical droplets pinch off from the extrusion nozzle. Lowering the flow rate of the aqueous phase to 0.2 ml/hr results in the extrusion of a continuous liquid tubule. The fiber undulates in the widening channel due to the reduced shear stress (see SI-video 5 [19]).

Different shapes of droplets can be obtained by varying the water phase flow rate (Fig. 2.10c and SI-video 6 [19]). The droplet length increases by lowering the water flow rate (Fig. 2.10d). When the water flow rate drops below 0.2 ml/hr a continuous liquid tubule is formed.

The observed flow behavior is the opposite from what one would expect during a microfluidic dripping to jetting transition[34]. Rather than obtaining a continuous jet of the DEP/ethanol mixture via increasing the water flow rate, here increasing the water flow rate results in a transition from a liquid tubule to shorter cylindrical droplets. We show in the following that this behavior originates from the rigid interfacial assembly of the SNP.

High-speed video microscopy shows the individual droplet pinch-off events (Fig. **2.**11a). A single droplet elongates until a critical length and pinches off. The critical length depends on the water flow rate as shown in Fig. **2.**11b & c. At a constant water flow rate, the pinch-off events repeat themselves always at the same critical length, explaining the monodispersity of the elongated droplets.

We hypothesize that the droplet elongation can be described by a simple force balance. While the oil/ethanol mixture flows out of the capillary as a droplet, it experiences a pull from the surrounding water flow. The droplet elongates as a cylinder from the capillary orifice facilitated by the ethanol transfer-induced lowering of the interfacial tension. The cylindrical shape is then stabilized via the interfacial deposition and crosslinking of the SNP.

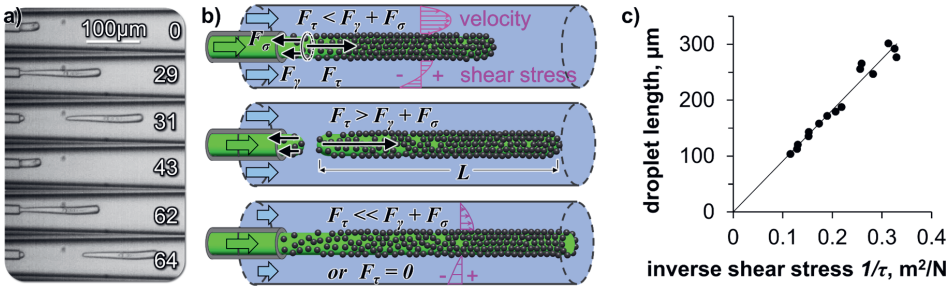

Fig. 2.11 Mechanics of droplet pinch off. (a) High-speed video micrographs of droplet pinch-off with time in milliseconds, (b) Illustration of the force balance during droplet pinch off (not drawn to scale),

illustration includes depiction of calculated velocity and shear stress profiles in water stream, (c) Droplet lengths from Fig. 2.10 (d) plotted against inverse shear stress.

The pulling force on the droplet originates from the shear-force of the surrounding water stream. The resulting shear force can be written as $F_\tau = L \cdot \pi \cdot D \cdot \tau$, with L the droplet length, D the diameter of the droplet, and τ the shear stress. While L increases, F_τ increases proportionally. Two forces are resisting the shear force: (*i*) The surface tension force calculates to $F_\gamma = \gamma_{ow} \cdot \pi \cdot D$, with γ_{ow} the oil/water interfacial tension, (*ii*) A tensile force builds up gradually in the deposited interfacial nanoparticle film on the droplet, equaling to $F_\sigma = \sigma \cdot \pi \cdot D \cdot s$, with σ the tensile strength and s the nanoparticle film thickness. We hypothesize that instantaneously before droplet pinch off, the forces balance each other according to $F_\tau = F_\gamma + F_\sigma$ (see Fig. **2.**11b).

Substituting and rearranging the force balance yields $L = (\gamma_{ow} + \sigma s) \cdot 1/\tau$. If our hypothesis holds true, plotting L against the inverse shear stress $1/\tau$ on the fiber surface will give a linear trend (for constant $\gamma_{ow} + \sigma s$). To obtain the shear stress on the fiber surface, we use the solution for the Navier-Stokes-Equation for pressure driven flow in a cylindrical annulus, with the inner cylinder (the droplet) moving at the velocity U (Appendix 2.5.8)[18]. Indeed, the data points for the droplet lengths fall on a linear line when plotted against the inverse shear stress, suggesting that our force balance model is a valid approximation of the droplet pinch-off physics here.

Last, we discuss the particle attachment rate to the oil/water interface. As the droplet flows out of the tip of the glass capillary, silica nanoparticles attach to the newly formed oil/water interface. The stabilization of the out-of-equilibrium droplet shapes suggests that the particle deposition rate exceeds the droplet area generation rate. We approximate the average particle deposition time t_D to form a monolayer on the interface by combining the Stokes-Einstein equation, the formula for the 1-dimensional mean square displacement, and a formula estimating the diffusion distance (see Appendix 2.5.5).

$$t_D = \frac{2\pi\mu d^3}{3kT}\left(\frac{\rho_p}{\rho_s}\frac{\xi}{w}\right)^2 \qquad (2)$$

With μ the viscosity of water, d the diameter of the nanoparticles, k the Boltzmann constant, T the absolute temperature, ρ_p the density of the nanoparticles (here 2.2 g/ml), ρ_s the density of the particle dispersion (here 1.03 g/ml), ξ the hexagonal packing area fraction (0.907), and w the nanoparticle weight fraction (here 0.05 g/g).

We can now compare the diffusion time with the droplet pinch-off time. Fig. 2.12b shows high-speed video microscopy of the droplet pinch-off. The pinch-off time for the cylindrical droplet is on the order of a few tens of milliseconds. The approximation of the diffusion time and the drop formation process

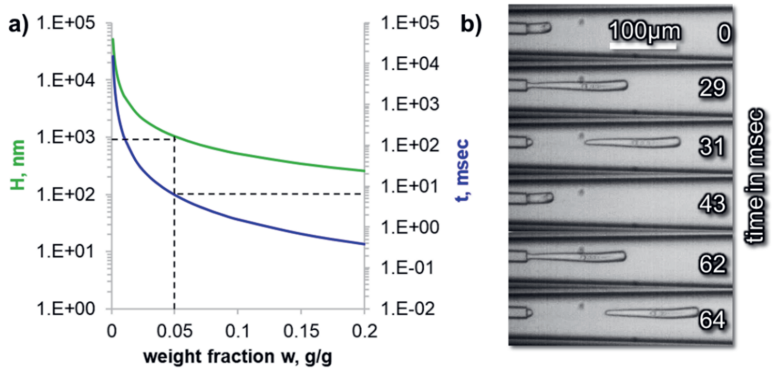

Fig. 2.12 Comparison of approximated nanoparticle diffusion time and droplet formation time. a) Height of aqueous column above the interface with sufficient particles for stabilization and diffusion time t over the average height H/2. b) High-speed video micrographs of the droplet pinch-off in the microfluidic device.

have roughly the same order of magnitude. We calculate t_D to 6 msec, which is on the same order of magnitude as the droplet generation time shown in Fig. **2.**12b (~30 msec). It seems, that the particles have just enough time to stabilize the interface. According to Fig. 2.12a, lowering the particle concentration will result in a significantly longer diffusion time, thus there must be a threshold concentration below which the out of equilibrium droplet shapes cannot be stabilized.

Based on our estimation of t_D, the particles have just enough time to stabilize the interface. This provides an additional explanation (besides the preceding shear stress discussion) to why nonspherical droplets cannot be formed at higher water flow rates (> 1.5 ml/hr, Fig. **2.**d). At higher water flow rates, the droplet pinch-off frequency becomes so high that the particles do not have enough time to cover the droplet surface.

Before we conclude, we briefly state the limitations of our model to estimate t_D. Our calculation neglects that not all particles that diffuse to the interface attach successfully. There can be an electrostatic energy barrier to overcome. Moreover, the more particles attach, the harder it is to find a “free spot”. These two processes can increase t_D. On the other hand, the initial stabilization of the out-of-equilibrium droplet shape may not require full coverage by the nanoparticles, as a partially covered surface can already provide sufficient rigidity based on the formation of a La^{3+} cross-linked silica particle gel like structure on the droplet surface. Another aspect favoring a more rapid stabilization is that the convective flow of water around the droplet replenishes the nanoparticles that have been deposited on the interface, thereby shortening the diffusion distance. Last, the diffusion of ethanol from oil to water during the experiments may induce Marangoni flows that additionally transport particles by convection to the interface.

2.3 Conclusion

In summary, we introduce a facile route to generate stable cylindrical droplets and tubules of oil in water. The anisotropic droplet shapes are stabilized by a rigid interfacial assembly of silica nanoparticles. The nanoparticles self-assemble on the oil/water interface due to their partial wettability by the oil phase, imparted by the adsorption of a small cationic organic molecule on the nanoparticles. The rigidity of the assembled nanoparticle film results from interfacial particle crosslinking, facilitated by their interaction with a three-valent cation. The droplet deformation to cylinders or tubules is realized either via gravitational or hydrodynamic forces. A deformation away from spherical is made possible due to a reduction of the interfacial tension, enabled by the mass transfer of a solvent. We introduce models to analyze the hydrodynamic forces and the nanoparticle deposition rates on the droplets. Our technique of forming anisotropic oil droplets and tubules can potentially be used for different types of oil. For instance, acrylic oils can allow for the formation of polymeric microparticles and fibers. Moreover, our approach can be further developed for the 3D-printing of Newtonian Fluids, complementing the existing additive manufacturing techniques

2.4 Materials and methods

Materials. Aqueous SNP suspensions (Ludox TM-50, pH 9), hexadecyl-trimethylammonium bromide (C_{16}TAB) with purity >98%, hexyltrimethylammonium bromide (C_6TAB, >98%), diethyl phthalate (DEP, 99.5%), Lanthanum(III) chloride heptahydrate ($LaCl_3 \cdot 7H_2O$), 1H,1H,2H,2H-Perfluorooctyltriethoxysilane, 2-Propanol (anhydrous, 99.5%) were purchased from Sigma-Aldrich and used as received. Deionized water and ethanol (>99.5%) were used for all the experiments.

Foam stability. 10 ml stock solutions of 5 *wt*-% Ludox TM-50 (A), 100 mM HTA^+ (B), and 10 mM La^{+3} (C) were prepared in deionized water. As shown in Figure 2, different mixtures were prepared with final concentration of 5 *wt* % nanoparticles, 10 mM HTAB and 1 mM La^{+3}. The pH values of all mixtures was determined to be 9 ± 0.2.

Pendant drop tensiometry. Interfacial tension measurements were carried out using a pendant drop tensiometer (ThetaPhysics OCA15) by fitting the droplet shape with the Young-Laplace equation. Please see appendix for more details about the procedures.

Dynamic light scattering. The size of Ludox TM-50 particles/aggregates was measured at varying La^{3+} concentration by dynamic light scattering (Malvern Zetasizer Ultra) at 633 nm wavelength of a He-Ne laser; the back scattered light was detected at 173°. The hydrodynamic diameter of particle/aggregates was obtained from the number distribution by cumulant analysis.

Zeta potential measurement. Electrophoretic mobility measurements were carried out to measure the zeta potential of the SNP as a function of La^{+3} ion concentration. Zeta potential was calculated from the electrophoretic mobility with the Smoluchowski equation.

Microfluidic device fabrication and experiments. Please see appendix for experimental details about the procedures.

2.5 Appendix

2.5.1 Droplet formation with 10 mM HTA^+, or 1 mM $La3^+$ alone

Fig. 2.13 Shows the extrusion of diethyl phthalate (DEP) with 20 vol % of ethanol at 15 ml/hr flowrate in an aqueous dispersion of 5 *wt* % nanoparticles with either 10 mM hexyltrimethylammonium bromide (HTAB) or 1 mM La^{3+}. In both cases, no tubule formation is not observed only drops are formed with slightly oblate shapes.

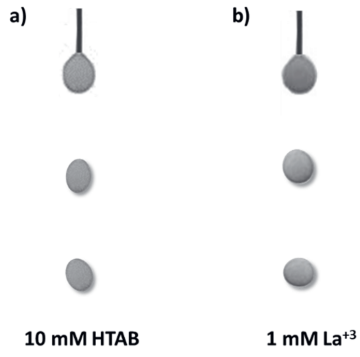

Fig. 2.13 diethylphthalate (DEP) with 20 vol % of ethanol at 15 ml/hr flowrate in aqueous dispersion of 5 *wt* % nanoparticles a) 10 mM HTAB b) 1mM $La3^+$.

2.5.2 Pendant droplet volume reduction with $La3^+$ alone

Fig. 2.14 depicts the control experiment to check the effect of La^{3+} ions alone on interfacial aggregation. A drop of the same volume was exposed to an aqueous suspension of 5 *wt* % nanoparticle with 1 mM La^{3+}. Subsequently, the area was reduced by 50% by withdrawing the oil in one step. No change in shape or wrinkles was observed in this case and the drop seems to be spherical same as in the case of HTA^+.

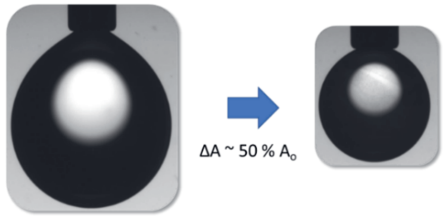

Fig. 2.14 Optical image of 50 % area compression of oil drop in water with 5 *wt* % NPs and 1 mM La^{3+}.

2.5.3 Critical force determination for droplet pinch-off

Fig 2.15a shows drop size reduction as a function of increasing ethanol vol % (0-20) in DEP. The threshold size (*Dc*) of the drop decreases gradually from 2 mm to 1.6 mm before pinching from the extrusion nozzle or forming fiber. This can be understood with the analysis of net force balance on the drop. We assume the density of the drop to be constant and calculate the gravitational force acting against the surface tension. Fig 2.15b shows a schematic of the force balance between surface tension and the gravitational pull on the drop. As we increase the ethanol vol-% in DEP interfacial tension decreases and less gravitational force is required to pinch off or elongate the droplet. Critical force (*Fc*) is defined as the force acting on the drop of critical diameter and causes pinching or elongation. Above 12 vol% of ethanol continuous liquid tubule generation was observed.

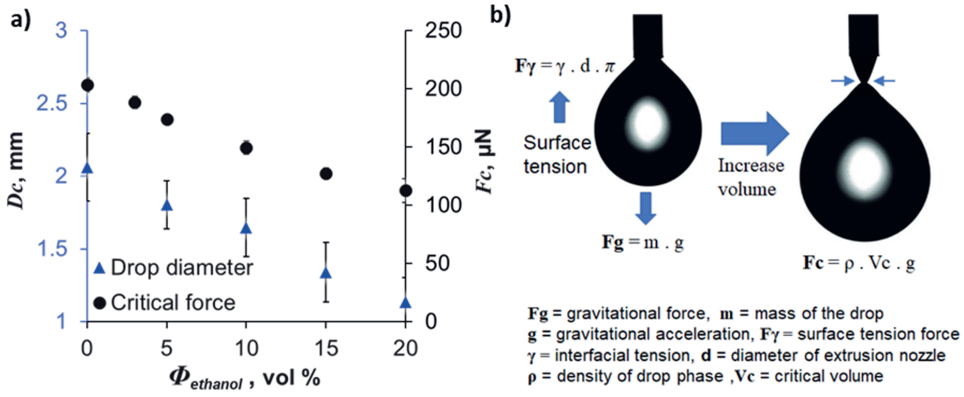

Fig. 2.15 a) shows the variation of critical drop size (Dc) and force (Fc) acting on the drop at the point of detachment from the extrusion nozzle with various φethanol. The concentration of silica particles (5 *wt* %), C_6TAB (10 mM) and La^{3+} ion (1 mM) are kept constant for all the experiments. b) Depicts a schematic of force balance in pendant drop experiments.

2.5.4 Interfacial tension measurements in dependence of the ethanol concentration

In Fig. 2.8a Increasing the ethanol volume % in water from 0 to 40 reduces the interfacial tension between pure DEP and water from ~15 mN/m to ~ 2 mN/m. All the measurements were recorded at room temperature. The dynamic interfacial tension is constant over time in Fig 2.8a we have added ethanol to the surrounding water phase, not the DEP droplet phase. If ethanol would have been added to the droplet phase, the diffusion of ethanol would have caused the interfacial tension to change over

time. Because of the limited reproducibility of this experiment, we have decided to measure the interfacial tension with a constant ethanol concentration in the surrounding water.

2.5.5 Estimation of the nanoparticle deposition rate

The goal of the following calculation is to estimate the time it takes for nanoparticles in dispersion to form a monolayer on an oil/water interface. We consider transport by diffusion from a liquid column above the interface as depicted below.

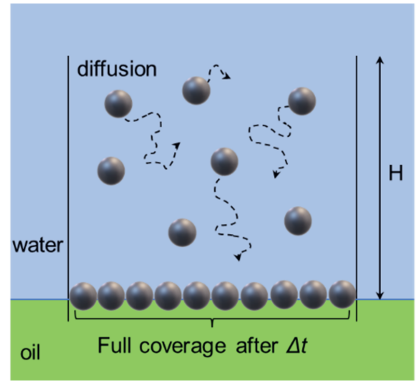

Fig. 2.16 Schematic depiction of particles in a liquid column

The suspension has a particle weight fraction w. How high must H be to provide enough particles for the full coverage of the interface? We assume that half of the particles diffuse upwards away from the interface and other half downward to the interface. The particles cover the surface in hexagonal packing with an area of 91%.

$Coverage: A * \varepsilon$

$A\ is\ area,\quad coverage\ factor\ \varepsilon\ (0.91\ for\ 2D\ particle\ packing)$

cross section area of the particle $a = (\pi/4) * d^2$

maximum number of attached particles $N_{P,A} = \frac{A*\varepsilon}{a} = \frac{A*\varepsilon*4}{(\pi*d^2)}$

volume of suspension above the interface can be calculated considering the depiction above

$V = A * H$

volume fraction of particles in suspension $\rho = w * \varepsilon * (\frac{1}{\varepsilon_p})$

where $w = weight\ fraction, \varepsilon = suspension\ density, \varepsilon_p = particle\ density$

volume of one particle $V_{Pi} = \left(\frac{4}{3}\right) * \pi * r^3 = \left(\frac{1}{6}\right) * \pi * d^3$

volume of partices in suspension $V_p = V * \rho = A * H * \rho$

number of particles in suspension $N_{\mathrm{PA}} = \left(\frac{V_p}{V_{pi}}\right) = (A * H * \rho * 6)/(\pi * d^3) = (A * H * 6 * w * \varepsilon)/(\pi * d^3 * \varepsilon_p)$

two times as many particles in suspension (half diffuse up) as there will be on the surface

$$\left(\frac{1}{2}\right) * N_{P,V} = N_{P,A}$$

$$\frac{A*H*6*w*\varepsilon}{2*\pi*d^3*\varepsilon_p} = \frac{A*\varepsilon*4}{\pi*d^2} = \frac{3*H*w*\varepsilon}{d*\varepsilon_p} = 2\,\varepsilon$$

$$H = \left(\frac{4}{3}\right) * (\varepsilon * d * \varepsilon_p)/(w * \rho)$$

$$5\ wt\ \%\ (w = 0.05), \qquad \varepsilon_p = 2.2\ \left(\frac{g}{ml}\right)\ (silica\ density)$$

$$\varepsilon = 1.03\ \left(\frac{g}{ml}\right)\ (\ density\ of\ silica\ suspension)$$

$$d = 20\ nm\ (Ludox\ TM\ particle\ size)$$

$$H = 1033\ nm$$

That means, if half of the particles from the volume V = H*A diffuse to the interface, the longest distance to travel is 1033 nm. On average, the particles diffuse a distance of H / 2 = 516 nm.

Next, we determine the time it takes for a particle to diffuse the average distance H / 2. To this end, we first calculate the diffusion coefficient of the particles with the Stokes-Einstein relationship.

$D = \frac{kT}{6*\pi*v*r}$ $\qquad D = 2.18 * 10^{-11}\,\frac{m^2}{s}$

$k - Boltzmann\ constant = 1.3806 * 10^{-23}\,\frac{(m^2.kg)}{(s^2\ .k)}$

$T - Temperature = 298\ k$

$v - dynamic\ viscosity = 10^{-3}\ Ps.s$

$r - particle\ radius = 10^{-8}\ m$

The mean square displacement for diffusion in 1D calculates to

$$< (X_t - X_r)^2 > = 2 * D * t$$

$$\left(\frac{H}{2}\right)^2 = < (X_t - X_0) >^2$$

$$t = \frac{H^2}{8D} = \frac{(1033^2)}{8.2*10^{-11}} = 6\ ms$$

The dependence of H and t on the mass fraction of the nanoparticles is shown in Fig 2.11

2.5.6 Experimental procedure for the pendant drop measurements

A rectangular glass container is filled with an aqueous dispersion of 5 *wt* % Ludox TM particles, 10 mM HTA^+ and variable concentrations of La^{3+}. The glass cuvette is placed on the stage of a pendant drop tensiometer Theta Physics OCA. A 1 mL glass syringe with a 20 gauge dispensing needle (OD 0.908 mm, ID 0.603) is filled with diethylphthalate (98%, Sigma Aldrich). The syringe is mounted in the motorized dispensing unit of the pendant drop tensiometer and the needle is submerged in the Ludox dispersion. The camera is focused on the needle and the pixel to millimeter ratio is determined for the CMOS camera at the specific zoom level. A droplet of 15 microliter DEP is formed through the automatic dispensing unit. Based on the shape analysis of the droplet, the software determines the interfacial tension, the droplet volume and the droplet surface area. The volume of the droplet is reduced by 10 – 11 microliter at a rate of 2 microliter/s, resulting in an area reduction of the droplet of ~ 50%, as indicated by the droplet analysis. During this, the interfacial tension is perpetually measured at a camera frame rate of 40 – 110 Hz.

2.5.7 Microfluidic device fabrication and experiments.

A cylindrical glass capillary (OD 1 mm, ID 0.6 mm) is tapered with a Sutter P-1000 Micropipette puller. With the help of a ceramic scoring tile (Sutter), the tapered capillary ends are opened to obtain orifices of 25 µm and 70 µm, respectively. The tapered capillaries are submerged in a saturated solution of KOH in 2-propanol for 12hrs. Next, the capillaries are rinsed with water and ethanol. Then, the capillaries are thoroughly dried with a stream of Nitrogen and under vacuum to remove water. The capillaries are then placed in a desiccator and a few droplets of Trichloro (1H,1H,2H,2H-perfluorooctyl) silane are added in a petri dish next to the capillaries. A vacuum is applied for 2 hours through a vacuum pump to partially evaporate the Trichloro (1H,1H,2H,2H-perfluorooctyl) silane and coat the glass capillaries from the gas phase. After rinsing and drying, the two tapered capillaries are inserted into a square capillary (ID 1.05 mm), interdigitated and aligned under a microscope (see Fig 2.17). Dispensing needles are glued at the ends of the square capillary with 5-minute epoxy glue (12 hrs curing time) and connected with plastic tubing.

A mixture of 50 vol-% ethanol in DEP is flown out of the 25 µm capillary orifice, supplied at a pressure of 2.7 atm. The aqueous phase is flown at variable rates controlled by a syringe pump. A high-speed camera (Phantom Miro C110) is used to visualize the droplet formation on an inverted Nikon Diaphot microscope.

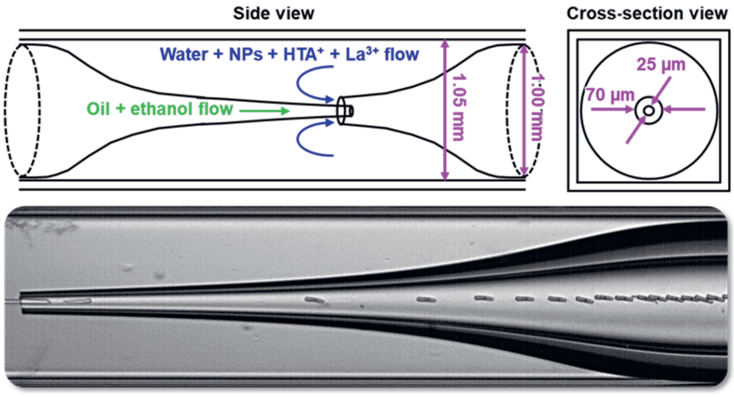

Fig. 2.17 Schematic drawing and micrograph of glass capillary microfluidic device.

2.5.8 Shear stress equation

A detailed derivation of the following equations can be found in the supporting info of Haase, M. F., Sharifi-Mood, N., Lee, D., & Stebe, K. J. (2016). In situ mechanical testing of nanostructured bijel fibers. *ACS nano*, *10*(6), 6338-6344.

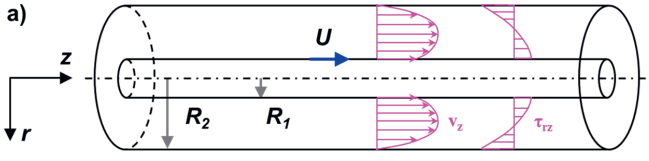

Fig. 2.18 Cylindrical annulus approximation of a cylindrical droplet in a cylindrical capillary. Water flows around the droplet with a volumetric flow rate Q_w. The cylindrical droplet moves with the velocity U (determined by high speed video microscopy). The droplet has a radius of R1 and the inner radius of the capillary is R2.

The radial velocity profile of the water around the cylindrical droplet calculates to

$$u_z(r) = -\frac{dp}{dz}\frac{\left({R_2}^2 - r^2\right)}{4\mu} + \left\{U + \frac{dp}{dz}\frac{\left({R_2}^2 - {R_1}^2\right)}{4\mu}\right\}\frac{ln(R_2/r)}{ln(R_2/R_1)}$$

with

$$\frac{dp}{dz} = \frac{2\mu\, ln(\frac{R_2}{R_1})}{\pi J}\left\{Q_w + \frac{2\pi U}{ln(\frac{R_1}{R_2})}[\frac{R_1^2}{2}ln(\frac{R_1}{R_2}) + \frac{R_2^2}{4} - \frac{R_1^2}{4}]\right\},$$

J is a geometrical parameter and calculates to

$$J = \left(\frac{R_1^4}{4} - \frac{R_2^4}{4}\right)ln\left(\frac{R_2}{R_1}\right) + \left(\frac{R_2^2}{2} - \frac{R_1^2}{2}\right)^2$$

The shear stress on the surface of the droplet calculates to

$$\tau_{rz}|_{R_1} = \mu\frac{(U_0 - U)}{R_1}\frac{1}{ln(R_2/R_1)}$$

With the parameter U_0 (the velocity of the droplet where it experiences 0 shear stress).

$$U_0 = \frac{dp}{dz}\frac{R_1^2}{2\mu}\ln\frac{R_2}{R_1} - \frac{dp}{dz}\frac{(R_2^2 - R_1^2)}{4\mu}$$

2.6 Bibliography

[1] L. Rayleigh, Proceedings of the London Mathematical Society 1878, s1-10, 4.
[2] X. Liu, S. Shi, Y. Li, J. Forth, D. Wang, T. P. Russell, Angewandte Chemie International Edition 2017, 56, 12594.
[3] J. Forth, X. Liu, J. Hasnain, A. Toor, K. Miszta, S. Shi, P. L. Geissler, T. Emrick, B. A. Helms, T. P. Russell, Advanced Materials 2018, 30.
[4] W. Feng, Y. Chai, J. Forth, P. D. Ashby, T. P. Russell, B. A. Helms, Nature Communications 2019, 10, 1095.
[5] G. Xie, J. Forth, Y. Chai, P. D. Ashby, B. A. Helms, T. P. Russell, Chem 2019, 5, 2678.
[6] A. R. S. L. J. Bonderer, L. J. Gauckler, Science 2008, 319, 1069
[7] D. Kohler, M. Schneider, M. Krüger, C.-M. Lehr, H. Möhwald, D. Wang, Advanced Materials 2011, 23, 1376.
[8] Y. Lu, Y. Yin, Y. Xia, Advanced Materials 2001, 13, 415.
[9] S. A. F. Bon, S. D. Mookhoek, P. J. Colver, H. R. Fischer, S. van der Zwaag, European Polymer Journal 2007, 43, 4839.
[10] A. Bala Subramaniam, M. Abkarian, L. Mahadevan, H. A. Stone, Nature 2005, 438, 930.
[11] A. R. Studart, H. C. Shum, D. A. Weitz, The Journal of Physical Chemistry B 2009, 113, 3914.
[12] M. Cui, T. Emrick, T. P. Russell, Science 2013, 342, 460.
[13] T. Merkel, V. Gräf, E. Walz, H. P. Schuchmann, Chemical Engineering & Technology 2015, 38, 1490.
[14] X. Li, Y. Xue, P. Lv, H. Lin, F. Du, Y. Hu, J. Shen, H. Duan, Soft Matter 2016, 12, 1655.
[15] S. Shi, X. Liu, Y. Li, X. Wu, D. Wang, J. Forth, T. P. Russell, Advanced Materials 2018, 30.
[16] Y. Jiang, T. I. Löbling, C. Huang, Z. Sun, A. H. E. Müller, T. P. Russell, ACS Applied Materials & Interfaces 2017, 9, 33327.
[17] L. Tran, H.-N. Kim, N. Li, S. Yang, K. J. Stebe, R. D. Kamien, M. F. Haase, Science Advances 2018, 4, eaat8597.
[18] M. F. Haase, N. Sharifi-Mood, D. Lee, K. J. Stebe, ACS Nano 2016, 10, 6338.
[19] M. A. Khan, M. F. Haase, Soft Matter 2021, 17, 2034.
[20] L. Tran, M. F. Haase, Langmuir 2019, 35, 8584.
[21] M. F. Haase, *Modification of nanoparticle surfaces for emulsion stabilization and encapsulation of active molecules for anti-corrosive coatings*, Universität Potsdam, 2011.
[22] A. F. Koretsky, P. M. Kruglyakov, Izv. Sib. Otd. Akad. Nauk USSR 1971, 2, 139.
[23] B. P. Binks, T. S. Horozov, *Colloidal particles at liquid interfaces*, 2006.
[24] R. Aveyard, B. P. Binks, J. H. Clint, Advances in Colloid and Interface Science 2003, 100-102, 503.
[25] W. J. Frith, R. Pichot, M. Kirkland, B. Wolf, Industrial & Engineering Chemistry Research 2008, 47, 6434.
[26] B. P. Binks, S. O. Lumsdon, Physical Chemistry Chemical Physics 1999, 1, 3007.
[27] J. K. Ferri, C. Kotsmar, R. Miller, Advances in colloid and interface science 2010, 161, 29.
[28] B. Noskov, G. Loglio, R. Miller, Advances in colloid and interface science 2011, 168, 179.
[29] J. Hegemann, S. Knoche, S. Egger, M. Kott, S. Demand, A. Unverfehrt, H. Rehage, J. Kierfeld, Journal of colloid and interface science 2018, 513, 549.
[30] B. P. Binks, L. Isa, A. T. Tyowua, Langmuir 2013, 29, 4923.
[31] M. F. Haase, K. J. Stebe, D. Lee, Advanced Materials 2015, 27, 7065.
[32] M. A. Khan, A. J. Sprockel, K. A. Macmillan, M. T. Alting, S. P. Kharal, S. Boakye-Ansah, M. F. Haase, Advanced Materials, n/a, 2109547.
[33] M. F. Haase, J. Brujic, Angewandte Chemie 2014, 126, 11987.
[34] A. S. Utada, Physical Review Letters 2007, 99, 094502.

Chapter 3

Nanostructured Bicontinuous Emulsion Gels

Abstract: Bicontinuous emulsion gels (Bijels) are a relatively new class of soft materials with a unique arrangement of two immiscible fluid streams separated by a percolating layer of particles. The conventional method uses temperature induced phase separation of a selected binary mixture of fluids to form bijels. This method leads to the formation of fluid channels no smaller than 5 μm and lacks channel size homogeneity, limiting the fluid-fluid interaction interface. In the current chapter, we discuss the control over the non-equilibrium self-assembly process of nanoparticles during spinodal decomposition to form bijel via STrIPS. This control enables the formation of a homogeneous submicron pore (300-500 nm) network and generates a specific surface area of ~2 m^2cm^{-3}. We found that preferential partitioning of the solvent to the oil is the major factor to stabilize the nanostructured liquid channels by controlling the *i.* interfacial tension evolution *ii.* in-situ particle modification. Interfacial tension studies, confocal analysis, and complimentary simulation experiments strongly support our hypothesis of rapid interfacial tension evolution and compatible in-situ hydrophobicity modification facilitate the jamming of particles and stabilize the bicontinuous emulsion gels with submicron channel size.

This chapter is based on
1) Khan, Mohd A., et al. "Nanostructured, Fluid-Bicontinuous Gels for Continuous-Flow Liquid–Liquid Extraction." *Advanced Materials* (2022): 2109547.
2) Fabrication of Bijels with Sub-Micron Domains with a Single-Channel Flow Device; Alessio J. Sprockel[1]; Mohd A. Khan[1]; Mariska de Ruiter; Katherine A. Macmillan; Meyer T. Alting (*submitted*)

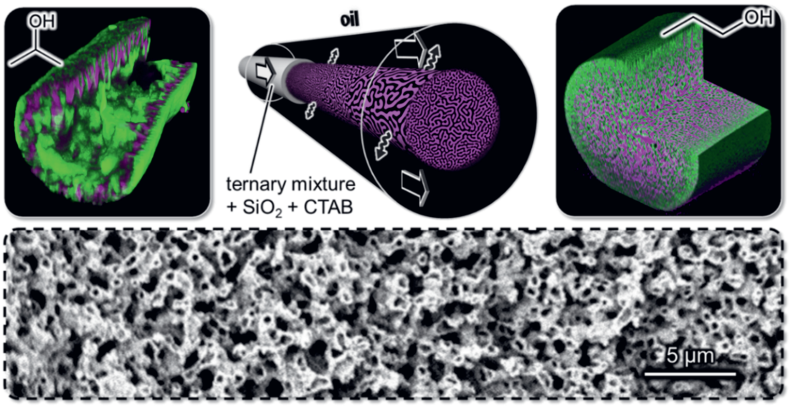

3.1 Introduction

Nanostructured materials formed via the kinetic arrest of non-equilibrium self-assembly processes are an active field of research due to their rich diversity and the complexity of their formation pathways.[1] Fluid-bicontinuous gels are kinetically arrested colloidal gels that facilitate intimate contact between two immiscible liquids, while each liquid remains fully interconnected.[2, 3] Recently, these structures have been employed for the fabrication of separation membranes[4], micro-reactors[5], sensors[6], energy storage devices[7], carbon monoliths[8], micro-ropes[9], and tissue engineering scaffolds[10]. However, limited control over their history dependent formation process and the inability to flow liquids through them has restricted their potentials until now.

Fluid-bicontinuous gels are obtained via the self-assembly of colloids on the interface of two interwoven liquids, such as oil and water. The assembly is driven by the reduction of the interfacial energy because the colloids remove contact area between the immiscible liquids. As a result, a close-packed colloidal monolayer is formed, which arrests the interwoven fluid arrangement mechanically to generate a bicontinuous interfacially jammed emulsion gel (bijel). The main pathway to obtain the bicontinuous fluid arrangement in a bijel is phase separation via spinodal decomposition.[11] Conventionally, spinodal decomposition is initiated by changing the temperature of a solution of two partially miscible liquids containing dispersed colloids.[3, 6, 8] However, the interfacial tension between fluids undergoing thermally-induced spinodal decomposition is not high enough to be able to employ nanoparticles (<100 nm) as interfacial stabilizers because their interfacial binding energy is too low. Instead, larger colloidal particles (>200 nm) are needed, resulting in fluid-bicontinuous gels with micrometer-sized fluid domains (> 5 μm).[3] [12] Submicron domains are crucial for the utilization of bijels in applications because of the larger surface area provided for mass transfer between the two liquids. In recent work, bijels with sub-micrometer domains have been obtained via vigorous agitation of emulsions together with nanoparticles and surfactants.[13] However, this method follows a batch fabrication protocol. Solvent transfer induced phase separation (STrIPS) enables both the use of nanoparticle stabilizers, as well as a continuous and scalable production route for bijels.[14, 15] Prior to this work, STrIPS has only formed irregular bijels with submicron pores on the surface and micron-scaled, internal domains. [15, 16] The high surface area achieved with submicron domains makes bijels ideal candidates to become mass transfer devices, where molecular exchange between the two liquids can take place through the interstitial spaces between the nanoparticles.

Here, we present the successful production of bijels with internal submicron domains of the smallest pore sizes yet reported via a continuous and scalable synthesis method based on STrIPS. In this work, we show that the non-equilibrium self-assembly process of nanoparticles during spinodal decomposition can be fully controlled. This control enables the formation of bijels with pores of 300-500 nm. The results from confocal microscopy, interfacial tensiometry, electron microscopy and

computer simulations are combined to give a complete discussion of the stabilization mechanisms of bijels with submicron-scaled features. With features this small, we find that the bijels have surface areas between the immiscible fluids of up to 2 m^2/cm^3. Based on our experimental results and confirmatory simulations we validate our hypothesis, rapid evolution of interfacial tension and in-situ modification of particles are the two major factors during STrIPS to generate bijel with submicron size structures.

3.2 Results and Discussion

3.2.1 Fabrication of nanostructured fluid-bicontinuous gels

The STrIPS process involves using two immiscible liquids, such as oil and water, that with the addition of a third solvent, such as alcohol, can become miscible. The volumes needed for mixing are given in the white region above the binodal curve in the ternary phase diagram of Fig. 3.1 and Appendix Fig. 3.). Once mixed, the removal of the solvent induces phase separation, often via the formation of water-in-oil or oil-in-water droplets (schematically depicted by black and magenta circles under the binodal curve in Fig. 3.1a). In contrast, below the critical point (marked in green in Fig. 3.1a), phase separation proceeds via the formation of interwoven oil and water channels (spinodal decomposition).[17] Unfortunately, this unique fluid arrangement is short lived because of the associated high interfacial energy. At last, two completely separated phases are formed by coarsening, minimizing the interfacial area between water and oil (Fig. 3.1b-i). Fortunately, the phase separating interwoven fluid arrangement can be stabilized via self-assembly of colloidal particles on the oil/water interface, forming a kinetically arrested soft material named "bijel".[2, 18] In a bijel, a rigid and percolating interfacial film of particles holds the interwoven fluids in place mechanically (Fig. 3.1b-ii).

A stable bijel requires the particles to be equally wetted by both fluids. To this end, we employ silica nanoparticles (20 nm diameter, Ludox TMA) and tune their wettability in-situ via the physisorption of cetyltrimethylammonium cations (CTA^+, Figure 1c-i).[19, 20] A commercially available dispersion of Ludox TMA particles is dialyzed at a pH value of 3 and a NaCl concentration of 50 mmol/L. Next, a homogeneous dispersion of the particles and CTA^+ is prepared in a critical precursor mixture of water, diethylphthalate (DEP) and 1-propanol. Interwoven fluids are formed in the mixture upon removal of 1-propanol via diffusion, a process termed solvent transfer induced phase separation (STrIPS).[14] In the following, STrIPS is initiated either by flowing the mixture through an octadecyl trichlorosilane coated glass capillary into toluene (Fig. 3.1c-ii) or by submerging an untreated glass slide coated with a thin film of the mixture into toluene (Fig. 3.1c-iii). This results in the formation of semi-solid bijel fibers or films with yield stresses of 4 – 6 kPa, please refer to Fig. 3.8 for the experimental details of insitu mechanical strength analysis.[21]

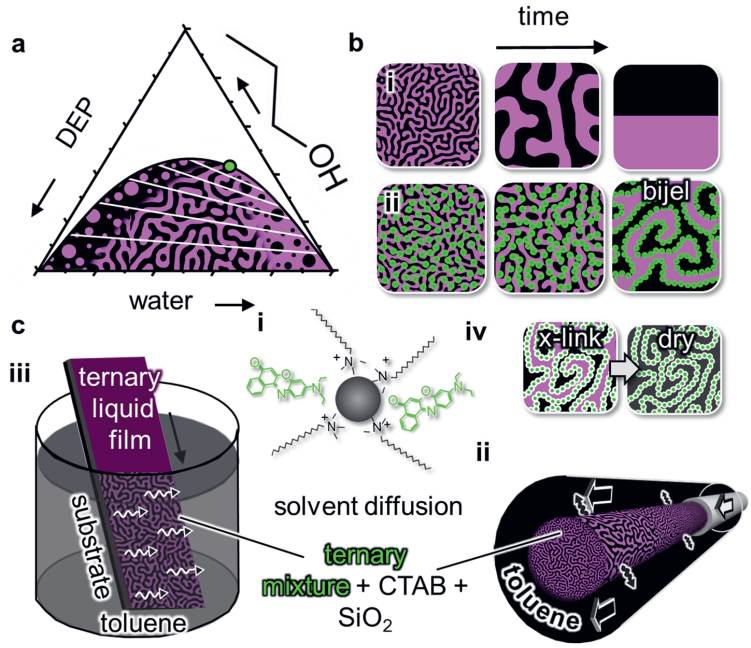

Fig. 3.1 Solvent transfer induced phase separation a) Ternary phase diagram plotting the miscible and immiscible regions in dependence of the volume fractions φ_i of water, diethyl phthalate (DEP) and 1-propanol (Appendix Fig. 3.8), the critical point is located at $\varphi_{DEP} = 0.08$, $\varphi_{1prop} = 0.42$, $\varphi_{water} = 0.50$ b-i) Phase separation via spinodal decomposition of oil (black) and water (magenta), b-ii) Bijel stabilization with nanoparticles (green), c-i) Particle modification with CTA^+ and Nile Red, c-ii) fiber formation, c-iii) film formation, c-iv) cross-linking with TEOS and drying

The suitable CTA^+ concentration to obtain the interwoven fluid arrangement varies among different batches of the commercial grade Ludox TMA and typically ranges from 21 to 26 mmol per liter of the precursor mixture. It can be determined rapidly by confocal microscopy analysis of fibers generated via pipetting the precursor mixture into toluene (Appendix Fig. 3.7). The fibers and films can be rigidified upon replacing the toluene with a solution of tetraethyl orthosilicate (TEOS) in light mineral oil after bijel formation. As was shown previously, TEOS cross-links the nanoparticles by producing additional silica at the particle surfaces[5], enabling drying and visualization of the material with a scanning electron microscope (SEM, Fig. 3.2a-c). SEM analysis shows that the surface pores on fibers and films are connected to the oil filled channels of the interwoven fluid beneath the surface (Fig. 3c).

A vast network of 300 – 500 nm sized oil channels is interwoven with 500 – 1000 nm sized water channels, an arrangement topologically analogous to a “plumber’s nightmare”.[22] Near the surface of the fiber, radially aligned and water filled macrovoids with sizes of several micrometers are observed. The same fluid arrangement can also be obtained in films generated with the precursor mixture shown in Fig. 3.2c.

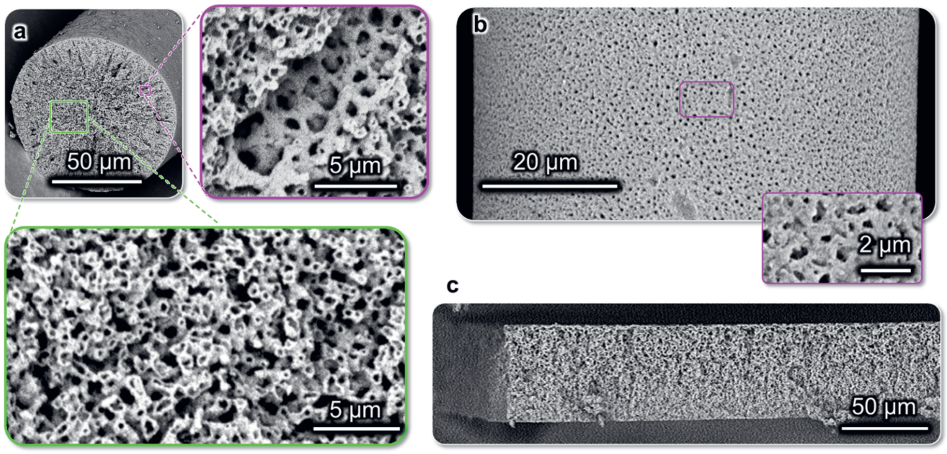

Fig. 3.2 Scanning electron (SE) micrographs of crosslinked bijel structure a) and c) SE micrographs of percolating silica scaffold within the fiber and freestanding film, respectively (Figure S4). b) Scanning electron (SE) micrograph of fiber surface

The unprecedented small oil channel sizes indicate that the coarsening of the interwoven fluids has been arrested at an early stage of the phase separation (Fig. 3.1b-ii). Which factors enable the stabilization of submicron fluid channels here? In the following, we discuss how the stabilization is facilitated by the interfacial tension of the phase separating precursor mixture.

3.2.2 Mechanism of small submicron sized STrIPS bijel formation

The driving force for nanoparticles to self-assemble on an interface is their interfacial attachment energy $\Delta E_{wo} = -\gamma_{wo} \cdot \pi \cdot r^2$, with γ_{wo} the water/oil interfacial tension, and r the radius of the spherical particle with a three-phase contact angle $\theta = 90°$.[23, 24] This simplified formula does not take into account effects arising from line tension k (important for particles < 10 nm, when k ranges from 10^{-11} – 10^{-9} N), which can change θ and result in an adsorption barriers for particles.[25, 26] To effectively stabilize a bijel, ΔE_{wo} must reach several hundred times the thermal energy kT of the particles, because this enables them to support the lateral stresses within the jammed interfacial nanoparticle film. After complete removal of propanol, the toluene/water interface reaches $\gamma_{wo} = 32$ mN/m (see Fig. 3.12). This results in a value for $\Delta E_{wo} = $ -2443 kT for the 20 nm particles employed here, confirming sufficiently strong particle attachment for a stable bijel. In contrast, the most frequently used fluid mixture for thermally induced phase separation (TIPS), lutidine and water, reaches only γ_{wo} = 0.6 mN/m at a temperature needed for a stable bijel (60°C).[27] For 20 nm particles, ΔE_{wo} calculates to -46 kT, insufficient for a stable bijel. This explains why STrIPS facilitates the use of nanoparticles to stabilize

the interwoven fluids, enabling submicrometer channel sizes, while TIPS requires larger colloidal particles, thereby limiting the smallest possible channel dimensions.[3, 8, 12]

Why did previous studies on STrIPS not introduce the formation of sub-micron sized channels throughout the entire bijel structure?[14] Here, we can reproduce the structure of a typical STrIPS bijel by employing 2-propanol as the solvent. The 2-propanol bijel is shown in the confocal laser scanning micrograph z-stack in Fig. 3.3i. Near the surface of the fiber (z = 5 µm) the nanoparticle stabilized interwoven oil/water channels have sizes ranging from 0.4 to 0.6 µm, while the center is composed of channels as big as 30 µm. In contrast, for the bijel formed with 1-propanol the pores in the center are as small as the surface pores of the 2-propanol bijel (Fig. 3.3-ii). To understand this difference, we analyze the mass transfer dynamics during STrIPS as well as their effect on the liquid-liquid interface and the nanoparticles for 1- and 2-propanol.

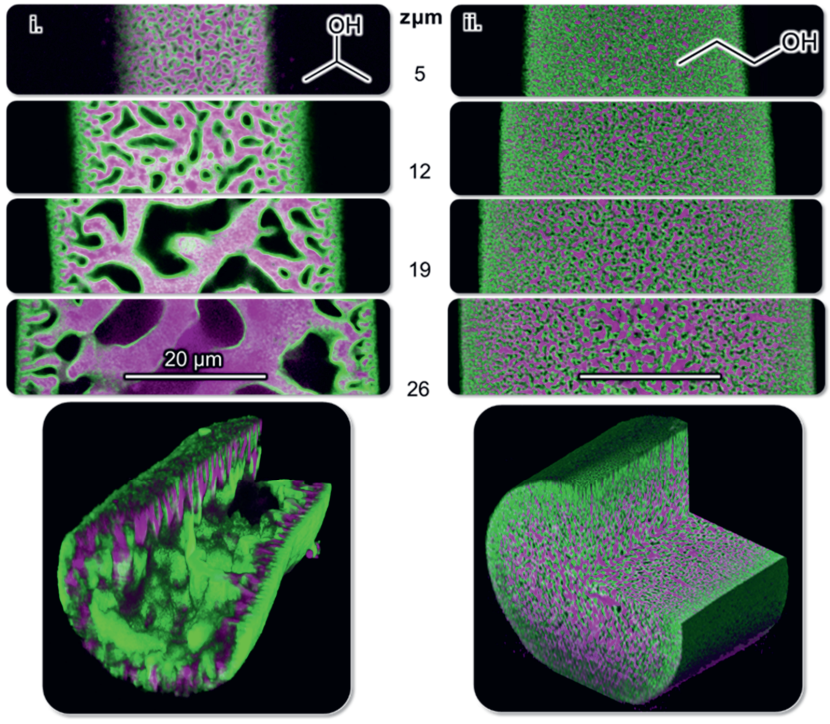

Fig. 3.3 Interwoven fluids formed with 1- and 2-propanol. a) Confocal laser scanning micrographs and their 3D reconstructions (bottom) of bijel fibers at different vertical distances from the surface (given as z-coordinate). For sample preparation, the fibers are submerged in a solution of Nile red in n-hexane. Nile red diffuses into the bijel and adsorbs on the particles (see also Fig. 3.1c-i). Upon blue laser light excitation (480 nm), adsorbed Nile red fluoresces in orange/red (550-700 nm), while Nile red dissolved in n-hexane fluoresces in green (500–550 nm, see Appendix Fig. 3.16). The fluorescenof the particles

is false colored in green and the inverted fluorescence signal from n-hexane (water domains) is false colored in magenta. The water channels of the bijel include 30 vol-% glycerol to enhance the optical transparency.

During STrIPS, propanol diffuses out and toluene diffuses into the precursor mixture as schematically depicted in Fig. 3.4a. The mass transfer near the surface of the fiber is faster compared to the center due to the shorter diffusion distance and steeper propanol concentration gradient. As a result, the homogeneous precursor mixture phase separates radially inwards, forming toluene and water rich interwoven fluid channels over time. Eventually, pure water and toluene channels are obtained because both 1- and 2-propanol are infinitely diluted in the volumetrically larger toluene.

The time evolution of the liquid compositions during STrIPS is schematically depicted with curved arrows in the ternary phase diagrams in Fig 3.4b. Starting from the critical point, the volume fraction of propanol φ_{pr} decreases, crossing multiple tie-lines on its path to the horizontal axis with $\varphi_{pr} = 0$. The tie-lines have different slopes for 1- and 2-propanol (Fig 3.4b).[28] They are flat for 2-propanol, while for 1-propanol they are inclined near the critical point. Since the endpoints of the tie-lines give the compositions of the toluene and water-rich phases, their slopes indicate the partitioning of 1- and 2-propanol. 2-propanol partitions equally between water and toluene. In contrast, 1-propanol partitions more into toluene. Different solvent partitioning behaviors can be explained using intermolecular interactions; in simple terms, as the hydrophobic area of short isomeric alcohols decreases (due to branching), their solubility in water increases.[29] Of course, there are other parameters involved and further research is required to understand the molecular reasoning of solvent partitioning during the ternary phase separation. The partitioning behavior of 1-propanol is the main cause for the smaller bijel structures. The first important role the partitioning has is its influence on the time evolution of γ_{wo}, as discussed next.

Combining measurements of γ_{wo} with mass transfer simulations suggests that the interfacial activity of the nanoparticles increases faster during STrIPS with 1-propanol as compared to 2-propanol. To arrive at this conclusion, we model the non-equilibrium time evolution of γ_{wo} during STrIPS with equilibrium values of γ_{wo}. The validity of this approach is supported by the agreement of experiments with simulations described in Appendix 3.5.7. Fig. 3.4c-i shows equilibrium measurements of γ_{wo} between toluene- and water-rich phases linked with a color code to the tie-lines of Fig. 3.4b. Going downward in the ternary diagram (pink to blue tie-lines) results in an increase of γ_{wo}. The downward direction corresponds to a decreasing propanol volume fraction in the water-rich phase φ''_{pr} (given by the right endpoint of the tie-lines in Fig. 3.4b). The increase of γ_{wo} in Fig. 3.4c-i has a higher slope for 1-propanol as compared to 2-propanol, reflecting the more dissimilar propanol content of the oil- and water-rich phases with 1-propanol.

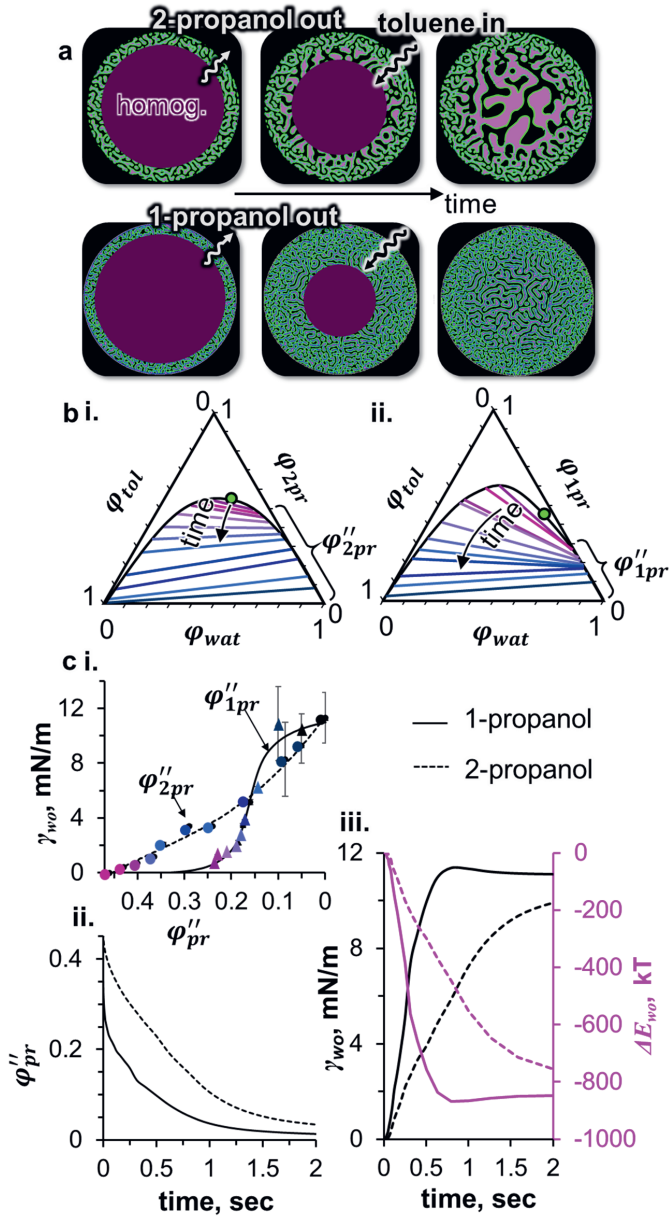

Fig. 3.4 a) Schematic depictions of the fiber cross section and the suggested structure formation dynamics during STrIPS for 1- and 2-propanol, b) ternary phase diagrams (volume fraction $\boldsymbol{\varphi}$ based) for toluene and water with either 2- or 1-propanol, c-i) Equilibrium interfacial tension between water rich (“) and toluene rich (‘) phases in dependence of the propanol volume fractions in the water rich phase $\boldsymbol{\varphi''_{1pr}}$ and $\boldsymbol{\varphi''_{2pr}}$, c-ii) Diffusion simulation predicting average $\boldsymbol{\varphi''_{1pr}}$ and $\boldsymbol{\varphi''_{2pr}}$ within the fiber of 25 µm radius over time, c-iii) Calculated values of the average interfacial tensions γ_{wo} and nanoparticle attachment energies ΔE_{wo} in the fiber over time.

We estimate the non-equilibrium γ_{wo} evolution during STrIPS by combining the trends in Fig. 3.4ci with a diffusion simulation predicting the average value of φ''_{pr} over time in the fiber (Appendix 3.5.7). The accuracy of the simulation has recently been supported by correctly predicting the density evolution of the phase separating liquid mixture.[29]

Our simulation predicts that propanol fraction in water rich phase (φ''_{pr}) decreases faster for 1- as compared to 2-propanol (Fig 3.4c-ii). From the simulated time dependence of φ''_{pr}, the time dependence of γ_{wo} is calculated. Fig. 3.4c-iii shows that γ_{wo} increases faster with 1-propanol compared to 2-propanol. The faster increase of γ_{wo} indicates a higher interfacial activity of the nanoparticles at initial stages of STrIPS due to a quicker increase of the absolute value of $|\Delta E_{wo}|$. The expedited increase of $|\Delta E_{wo}|$ suggests that the interwoven fluids formed with 1-propanol can be stabilized earlier during STrIPS, providing a first possible explanation for the smaller fluid channels.

Before analyzing additional rationales for the fluid channel size dependence, we briefly discuss a limitation of our γ_{wo} measurements. The toluene- and water-rich phases used to measure γ_{wo} contain dissolved CTA^+ with concentrations representative of the precursor mixture employed to fabricate the bijels (Fig. 3.7). Because of the interfacial activity of CTA^+, the maximum value for γ_{wo} = 11.5 mN/m at $\varphi''_{pr} = 0$ (Fig. 3.4c-i) is lower than for pure toluene/water (32 mN/m, Fig. 3.). However, the adsorption of CTA^+ to the interface takes several seconds (see

Fig. **3.**12). Thus, the equilibrium values of γ_{wo} used in our analysis are lower than the nonequilibrium values of γ_{wo} during STrIPS. But, since the nonequilibrium dynamics of the CTA^+ adsorption affect STrIPS for both 1- and 2-propanol, our analysis still allows for a comparison between the two solvents. Nevertheless, more research is needed to fully understand the γ_{wo} evolution in the presence of CTA^+.

The partitioning of 1-propanol has a second important consequence for the bijel stabilization. It controls the partitioning of CTA^+ and the silica nanoparticles between the toluene- and water-rich phases during STrIPS. Confocal micrographs in Fig. 3.5 show that for both 1- and 2-propanol the nanoparticles have formed a fluorescent interfacial film. For 2-propanol there are also aggregated particles in the water phase (Fig. 3.5-i). In contrast, for 1-propanol particles have aggregated in the toluene phase (Fig. 3.5-ii). To investigate the particle partitioning during STrIPS we compare the CTA^+ partitioning and particle dispersibility as a function of solvent fraction for 1- and 2-propanol systems (in Fig 3.22). Results suggest that the presence of the CTA^+ modified particles in the toluene occurs due to the strong partitioning of 1-propanol into this phase, which increases the CTA^+ solubility and therefore the particle dispersibility in toluene.

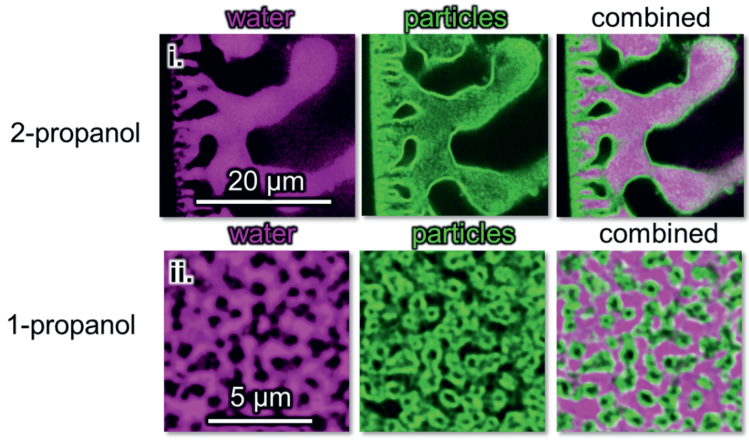

Fig. 3.5 Confocal micrographs of the different fluorescence channels of i) 2-propanol and ii) 1-propanol bijels

Fig. 3.25 shows that for 1-propanol emulsion inversion from oil-in-water to water-in-oil occurs between 21 – 25 mM CTA^+.In contrast, for 2-propanol oil-in-water emulsions are formed for all CTA^+ concentrations. This suggests that $\theta \approx 90°$ for 1-propanol, while $\theta < 90°$ for 2-propanol during STrIPS. With the near neutral particle wettability with 1-propanol, the particles do not impose a curvature on the liquid-liquid interface. As a result, both positive and negative interfacial curvatures of the spinodally demixing oil/water channel network can be stabilized, resulting in the characteristic bijel structure throughout the entire fiber (Fig. 3.3ii).

Last, the distinct particle partitioning also suggests different aggregation mechanisms. In the water phase, strong aggregation of the particles can occur due to the hydrophobic effect, as the CTA^+ covered particles disrupt the hydrogen bonding network of water.[31],[32] Weaker particle aggregation driven by van der Waals interactions occurs in the toluene phase due to the lack of inter-particle repulsion.[33] The strong particle aggregation in water with 2-propanol as the solvent can limit the availability of individual particles for interfacial stabilization. Thus, the oil/water interface can coarsen for a longer period before interfacial jamming occurs. In contrast, the weaker aggregation in toluene with 1-propanol allows the particles to self-assemble more readily at the toluene/water interface, generating a robust interfacial film at early stages of the spinodal phase separation.

To probe the effect of particle hydrophobicity, we prepared the precursor mixture at a composition of $\varphi_{DEP} = 0.07$, $\varphi_{1\text{-}prop} = 0.43$, $\varphi_{water} = 0.5$ with varying concentrations of CTA^+. At 17.2 mM CTA^+ particles

remain hydrophilic and the obtained structures show oil-in-water droplets (Fig. 3.6a-top row). Around 26 mM CTA^+, the most uniform pores are formed with a bicontinuous fiber structure. Further, 39 mM

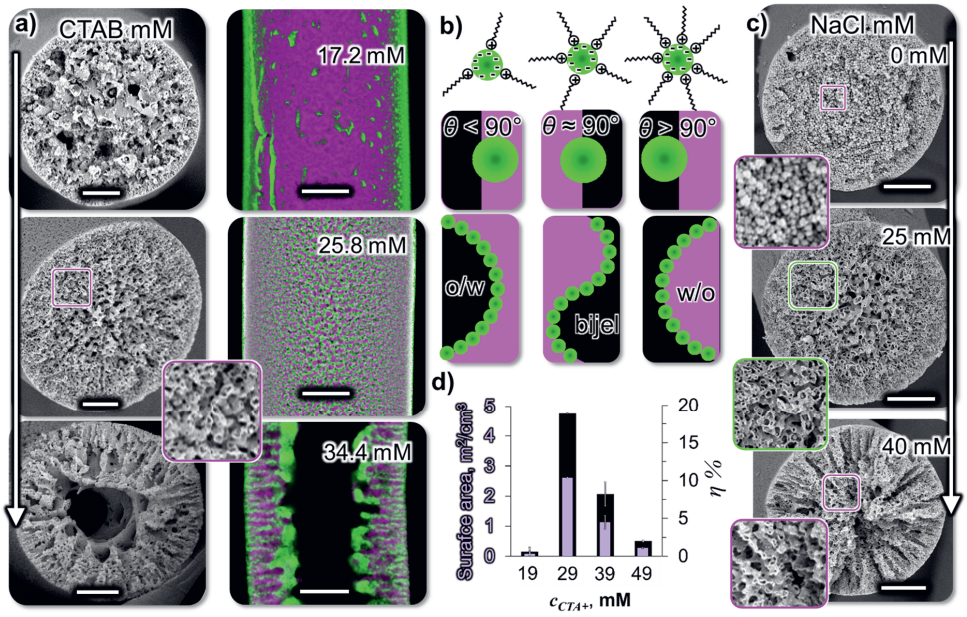

Fig. 3.6 Effect of CTAB and salt concentration on bijel morphology, **a)** Shows the SEM and confocal micrographs upon increasing the CTAB concentration. b) schematics of contact affecting the curvature of the interface. c) SEM micrographs showing the effect of salt variation. d) Surface area and interfacial attachment efficiency of the particles as a function of CTAB concentration. Scale bar 10μm.

CTA^+ results in the appearance of radially aligned channels near the outer surface of the fiber and a central oil-filled cavity. Increasing the CTA^+ concentration to 48.7 mM and higher results in an oil-filled hollow fiber with coarse channels that forms a shell-like structure (Fig. 3.22). Notably, at 48.7 mM CTA^+ water (magenta) appears to have separated from the particles (green), possibly indicating the dewetting from the particle surfaces due to the high hydrophobicity of the particles.

Image analysis can be used to calculate the interfacial area between hexane and water from confocal images obtained with different CTA^+ concentrations (Appendix 3.5.9). We normalize the interfacial area with the fiber volume and find that the most uniform bijels at 25.8 mM CTA^+ have a specific area of 2.6 m^2/cm^3. The number of NPs on the interface can be estimated using this area. To accomplish this, we assume that the NPs form a hexagonally packed monolayer at the interface, with each particle occupying an area equal to its cross-section. The ratio of particles at the interface to particles added to the initial precursor mixture is defined as the NP attachment efficiency (η) (see Appendix 3.5.9).

For 25.8 mM CTA^+, η reaches a maximum of 19 %, while for the highest and lowest CTA^+ concentration, η drops below 2.5%. The last physiochemical parameter analyzed against the bijel structure is salt at constant pH. Fig 3.6c shows the effect of salt concentration, we need a threshold concentration of salt to make a bicontinuous structure. Bijel structure upon salt variation follows a similar trend as CTA^+ variation (Fig 3.25). These results substantiate that tuning of CTA^+ and salt concentrations impart higher regulation over the structural homogeneity and domain size of the bijel.

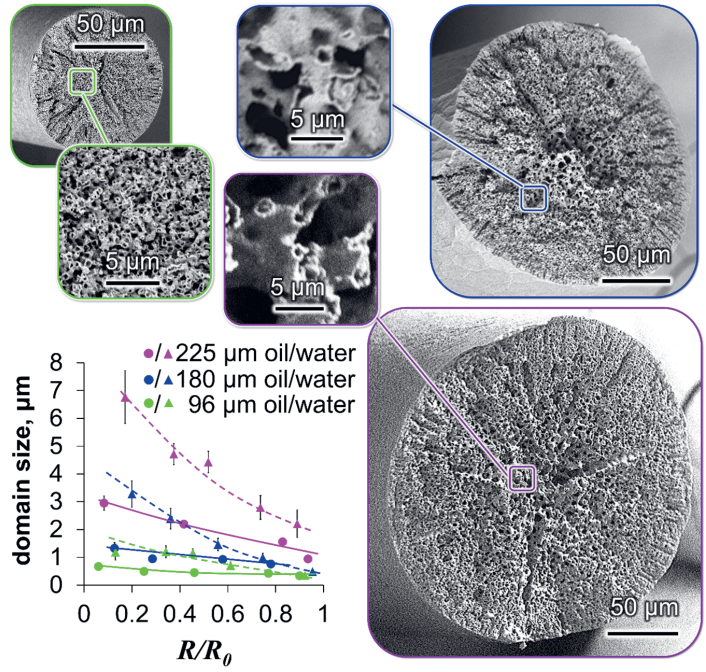

Fig 3.7 SEM images of bijel fibers with variable diameters color coded in green (96 µm), blue (180 µm), magenta (225 µm) show the domain sizes of the oil (rounds) and water (triangles) channels in dependence of normalized fiber radius. Lines in the graph are to guide the eyes.

Further, we also explored the scalability of submicron sized bijels. Fibers with diameters above 100 µm can be extruded with a fluidic device made with larger capillaries. The design of this device is detailed in the Appendix information. The resulting fibers are stored in a solution of TEOS in light mineral oil for 24 hours, washed in hexane, dried, and imaged with the SEM. Fig. 8 compares SEM images of fibers with diameters ranging from 90 – 300 µm.

Larger diameter fibers have an increased pore size gradient over their radius. Fig. 3.7 shows that for a fiber with 96 µm diameter (green frame), oil channels with sizes well below 1 µm are present throughout the structure. However, as the fiber diameter is increased to 180 µm (blue frame) or 225 µm (magenta frame), the oil channel sizes in the center increase to several micrometers. The water channels are

always larger in size. The graph in Fig. 3.7 gives the pore size of the oil and water channels in the fiber over the normalized radial coordinate (radial position R divided by outer radius R_0). Near the outer surface of the fiber ($R/R_0 \approx 1$), the smallest pores are observed. Towards the fiber center ($R/R_0 \approx 0$), the pore size grows for all fibers. The larger the fiber, the stronger the increase in pore size over R/R_0.

3.3 Conclusion

In summary, we have shown how bijels with sub-micrometer, interwoven fluid channels can be synthesized via solvent transfer induced phase separation (STrIPS). The unprecedented small bijel channel sizes are facilitated by combining amphiphilic nanoparticles with immiscible liquids of high interfacial tensions (γ_{wo}). STrIPS with 1-propanol generates nanostructured bijels because of the preferential partitioning of 1-propanol to the toluene-rich phase. The 1-propanol partitioning has two consequences: *i.* it facilitates a faster increase of $|\Delta E_{wo}|$, enabling more rapid bijel stabilization by the nanoparticles, and *ii.* it causes the CTA^+ and the nanoparticles to partition to the toluene-rich phase, resulting in enhanced colloidal stability during STrIPS and the attainment of a 90° contact angle. These two phenomenon work in synergy to quench the spinodal demixing of fluids by interfacial jamming and forms submicron sized emulsion gels. Also in contrast to prior reports, the control of the silica functionalization by CTA^+ facilitates the synthesis of bijels with well-defined submicrometer channels. These findings support the main hypothesis, which states that in order to stabilize the bijel, the nanoparticles require equal wettability for both the oil- and water- phases. It is suggested that this condition can be fulfilled by carefully tuning the nanoparticle/CTA^+ interaction via the pH value, CTA^+ concentration, and NaCl. Last, it is demonstrated how the production of bijel fibers with variable diameters at rates of milliliters per hour can be accomplished. It is shown that the bicontinuous channels increase in size from hundreds of nanometers to several micrometers upon increasing the fiber diameter. The findings from this work will help researchers to synthesize bijel fibers via STrIPS in the future. In our view, more research on STrIPS bijels is needed to transform these unique bicontinuous fluid structures into materials for energy storage, membrane separations, fuel cell components, and catalytic reactors.

3.4 Materials and methods

Chemicals: All solvents used in the experimental study are HPLC grade. Silica nanoparticles (Ludox TMA), Hexadecyl-trimethylammonium bromide (C_{16}TAB, >99%), 1-propanol (>99.5%), 2-propanol (>99.5%), Nile red, Tetraethyl orthosilicate (TEOS, >99%), Sodium hydroxide (≥99%), and mineral oil are purchased from Sigma-Aldrich UK. Diethyl phthalate (DEP, 99%), Toluene (99.85%), n-Hexane (99% HPLC), Glycerol (>99%), hydrochloric acid (HCl, 37% pure) were received from Acros organics. Ethanol and Triethylamine (TEA, >99.5%) are purchased from VWR international Ltd.

Ternary phase diagram measurement: We use turbidity analysis to determine the ternary phase diagram and emulsion inversion for critical point determination. Please refer to the appendix for the details of the experimental methods.

Interfacial tension measurement: Interfacial tension measurements were carried out using a pendant drop tensiometer (ThetaPhysics OCA15) by fitting the droplet shape with the Young-Laplace equation. Please see the appendix for more details about the procedures.

Confocal analysis: Confocal analysis was used to visualize the fluorescently tagged bicontinuous immiscible phases. The oil phase of the bijel was exchanged with hexane having a fluorescent dye Nile red. Nile red shows the solvatochromism property and fluoresces as per the solvent. Please refer to the appendix for details of the experiments and sample preparation.

Scanning electron microscopy analysis: A Phenom Pro X Scanning Electron Microscope has been employed for imaging the dried bijel fibers. Dry samples are sputter-coated with platinum (8-10 nm) before imaging. An accelerating voltage of 10 kV was used for the image acquisition.

COMSOL simulation: The Transport of Diluted Species module was used for the diffusion based simulation studies of 1 and 2-propanol in COMSOL. Macroscopic variables are provided as input from the literature and have been cited accordingly.

3.5 Appendix:

3.5.1 Measurement of ternary phase diagrams

Fig. 3.8A illustrates the measurement of the binodal curve in the ternary phase diagrams by turbidimetry. In brief, water is added to a miscible mixture of oil and solvent until the mixture becomes cloudy.

The critical point is determined as the ternary liquid composition for which a transition from an oil-in-water (o/w) to a water-in-oil (w/o) emulsions occurs. We determine this composition by adding the fluorescent dye Nile Red to immiscible precursor mixtures at different points next to the binodal line. Nile red partitions to the oil and the fluorescence emission can be used to determine the type of emulsion as shown in 8B. The critical point is determined for 2-propanol, DEP and water as $\varphi_{DEP} = 0.22$, $\varphi_{2Prop} = 0.48$, $\varphi_{water} = 0.30$ and for 1-propanol, DEP and water as $\varphi_{DEP} = 0.08$, $\varphi_{2Prop} = 0.42$, $\varphi_{water} = 0.50$.

With the critical point, the tie lines can be found graphically as illustrated in Fig. 3.8C. First, the binodal curve is plotted in rectangular coordinates and fitted with a polynom (for 1-propanol with DEP and water $y = 0.2922x^4 - 0.6874x^3 - 0.9552x^2 + 1.3554x - 0.0019$, for 2-propanol $y = -0.7786x^3 - 0.462x^2 + 1.2348x$). The critical point is then assigned the x-coordinate value c. Values for the corners of the ternary triangle α and β are determined. To obtain an arbitrary tie-line at the position x_1 between α and c, the corresponding position of point x_2 is calculated with the relation $\frac{|M-x_1|}{|M-\alpha|} = \frac{|M-x_2|}{|M-\beta|}$. Based on the polynomial fit, the corresponding values for y_1 and y_2 can now be found. Fig 3. 7D**.** shows the ternary diagrams measured by the aforementioned steps. Table 1 gives the volume fractions φ_i at the end points of the tie-lines for the water rich (“) and oil rich (‘) phases in equilibrium.

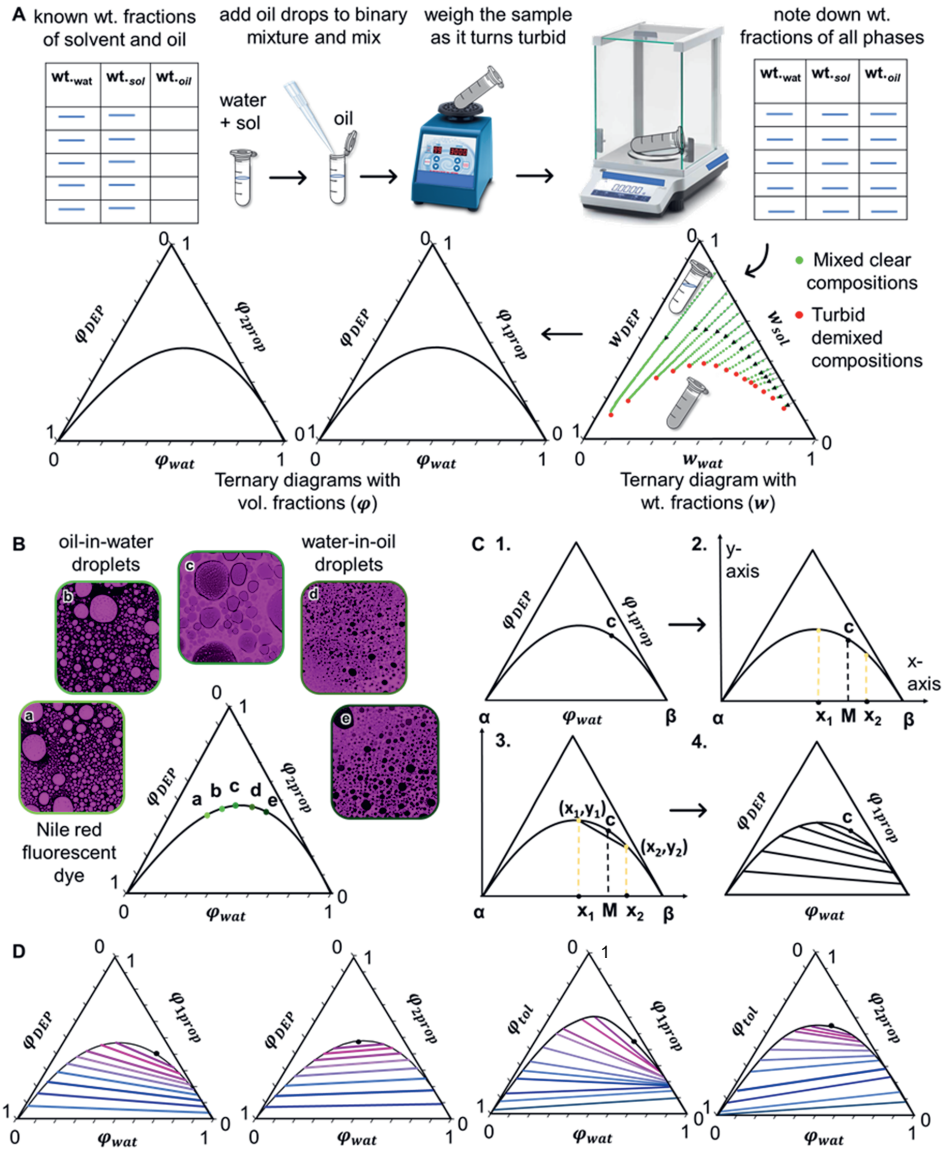

Fig. 3.8 (A) Schematic representation of plotting ternary phase diagram for 1 and 2-propanol with water and diethyl phthalate (DEP). (B) Phase inversion screening for critical point determination. Micrograph c shows the transition from o/w to w/o emulsion. (C) Graphical method depicting the determination of tie lines. (D) Volume fraction based ternary phase diagrams for water/DEP/1-propanol, water/DEP/2-propanol, water/toluene/1-propanol, and water/toluene/2-propanol [28].

DEP/1prop/water

φ'_{1prop}	φ'_{wat}	φ''_{1prop}	φ''_{wat}
0.470	0.270	0.320	0.645
0.450	0.200	0.280	0.680
0.420	0.150	0.240	0.745
0.380	0.115	0.210	0.775
0.340	0.085	0.180	0.805
0.280	0.070	0.150	0.084
0.225	0.050	0.115	0.875
0.155	0.030	0.075	0.910
0.080	0.010	0.035	0.960

DEP/2prop/water

φ'_{2prop}	φ'_{wat}	φ''_{2prop}	φ''_{wat}
0.425	0.200	0.450	0.450
0.395	0.165	0.425	0.485
0.355	0.140	0.395	0.545
0.310	0.105	0.350	0.600
0.260	0.080	0.305	0.670
0.205	0.060	0.250	0.745
0.145	0.045	0.175	0.820
0.080	0.025	0.100	0.900

toluene/2prop/water

φ'_{1prop}	φ'_{wat}	φ''_{1prop}	φ''_{wat}
0.600	0.220	0.265	0.725
0.580	0.175	0.260	0.730
0.535	0.100	0.235	0.760
0.510	0.095	0.230	0.765
0.415	0.050	0.209	0.790
0.330	0.040	0.190	0.809
0.265	0.030	0.185	0.814
0.135	0.005	0.170	0.830
0.080	0.000	0.150	0.850

toluene/1prop/water

φ'_{2prop}	φ'_{wat}	φ''_{2prop}	φ''_{wat}
0.555	0.230	0.530	0.380
0.540	0.150	0.480	0.460
0.520	0.130	0.460	0.495
0.475	0.095	0.430	0.540
0.400	0.070	0.400	0.580
0.330	0.450	0.365	0.620
0.260	0.035	0.345	0.645
0.075	0.010	0.240	0.760
0.030	0.000	0.150	0.850

Table 1 Ternary phase diagrams including compositions of oil-rich (φ') and water-rich phases (φ'') for DEP and toluene with 1- and 2-propanol and water.

3.5.2 Yield stress measurement of small domain bijel fiber

To measure the yield strength of bijel fibers, we adopted the same procedure described by Haase *et al* 2016 [21]. Analysis of the stress field allows yield strength to be estimated by using the following equation:

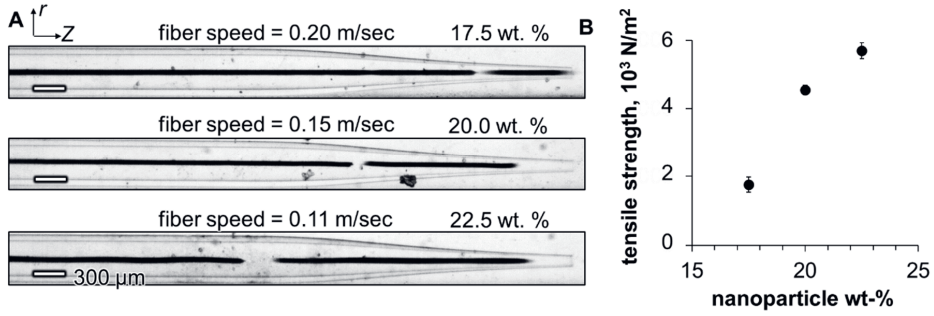

Fig. 3.9 Measurement of the tensile strength of bijel fibers with different *wt*. fractions (A) high speed video microscopy snapshots for fiber of different silica weight fractions breaking in a microfluidic constriction (B) Shows the measured tensile strength against nanoparticle *wt*. fraction.

Yield strength $(\sigma) = \frac{2}{R_1}\int_{Z_1}^{Z_2} r(Z)\,\tau_{rZ}\;dZ\,(1)$, where R_1 = fiber radius, Z_1 = location of the fiber where it snaps off, Z_2 = location of the fiber's leading end, $r(Z)$ = channel radius as a function of Z from Z_1 to Z_2, and τ_{rZ} = shear stress applied on the fiber surface. A bijel fiber enters a conical constriction after traveling through a channel at a constant speed Fig. 3.9A. The velocity of the coflowing toluene increases at the constriction, and shear forces locally accelerate and strain the fiber, resulting in fracture

of fiber. The yield stress of the fiber can be calculated by counterbalancing the shear force with tensile force at the time of fracture. Increasing the nanoparticle concentration in ternary results in higher yield stresses and is found to be maximum (4-6 kPa) at 22.5 *wt* %.

3.5.3 Bijel fiber preparation, structure analysis and composition optimization

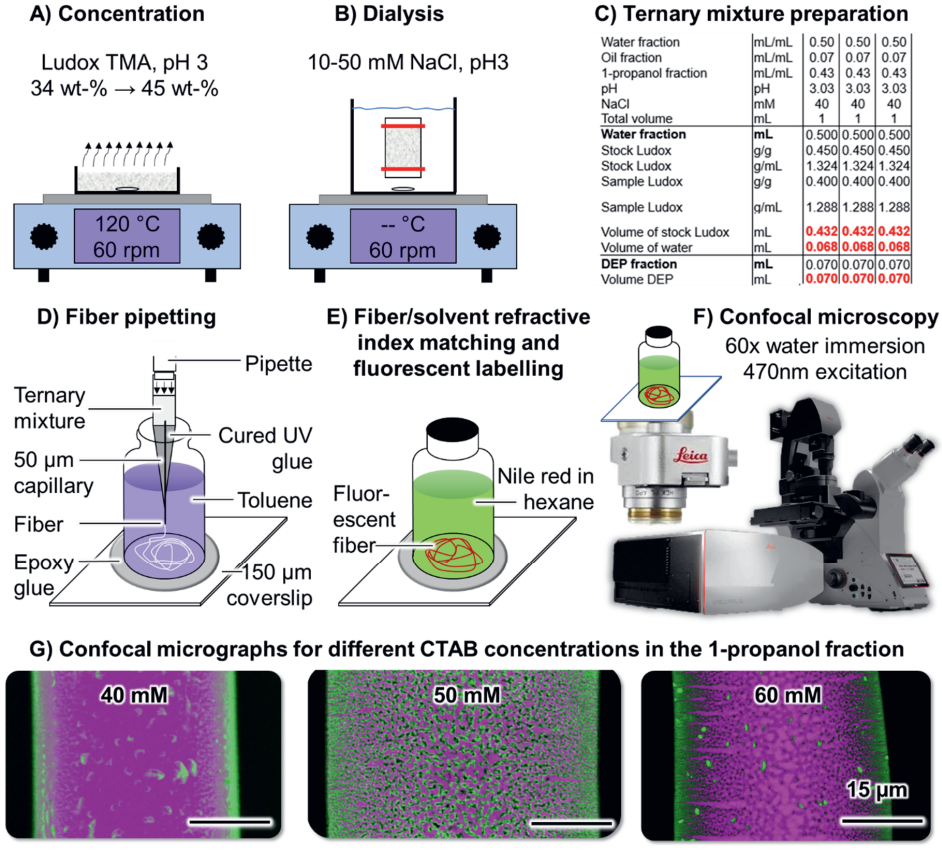

Fig. 3.7 Bijel fiber preparation, structure analysis and composition optimization.

Interbatch variations of the commercial grade Ludox TMA poses a need for rapid screening of parameters such as pH, NaCl, CTAB, and particle concentrations to generate well defined bijels. To rapidly determine suitable compositions of the precursor mixture, the following high throughput screening method is employed. First, the Ludox TMA dispersion is concentrated from 34 *wt*.% to 45 *wt*.% by evaporation of water Fig. 3.10A. The concentrate is centrifuged to remove aggregates and 0.1 M HCl is added to lower the pH to 3. The particle dispersion is dialyzed in water of pH 3 at a NaCl concentration of 50 mM Fig. 3.10B. After dialysis the pH, the particle concentration, and density are

Batch name	**Units**	**Formula**	C40	C50	C60
Water fraction	mL/mL	φ_{wa}	0.50	0.50	0.50
Oil fraction	mL/mL	φ_{DEP}	0.07	0.07	0.07
1-propanol fract.	mL/mL	φ_{1prop}	0.43	0.43	0.43
pH	pH		3.03	3.03	3.03
NaCl	mM	C_{NaCl}	40	40	40
Total volume	mL	V_{total}	1	1	1
Water fraction	**mL**	$\boldsymbol{V_{water}^{total}}$	0.500	0.500	0.500
Stock Ludox	g/g	w_{TMA}^{0}	0.450	0.450	0.450
Stock Ludox	g/mL	ρ_{TMA}^{0}	1.324	1.324	1.324
Sample Ludox	g/g	w_{TMA}^{1}	0.400	0.400	0.400
Sample Ludox	g/mL	$\rho_{TMA}^{1} = \frac{\rho_{TMA}^{0} - \rho_{water}}{w_{TMA}^{0}} * w_{TMA}^{1} + \rho_{wa}$	1.288	1.288	1.288
Volume of stock Ludox	mL	$V_{TMA} = V_{wa}^{total} * \frac{w_{TMA}^{1} * \rho_{TMA}^{1}}{w_{TMA}^{0} * \rho_{TMA}^{0}}$	**0.432**	**0.432**	**0.432**
Volume of water	mL	$V_{wa} = V_{wa}^{total} - V_{TMA}$	**0.068**	**0.068**	**0.068**
DEP fraction	**mL**	$\boldsymbol{V_{DEP}^{total} = V_{total} * \varphi_{DEP}}$	0.070	0.070	0.070
Volume DEP	mL	$V_{DEP} = V_{total} * \varphi_{DEP}$	**0.070**	**0.070**	**0.070**
1-propanol fraction	**mL**	$\boldsymbol{V_{1prop}^{total} = V_{total} * \varphi_{1prop}}$	0.430	0.430	0.430
Stock CTAB	mM	C_{CTAB}^{0}	200	200	200
Sample CTAB	mM	C_{CTAB}^{1}	**40**	**50**	**60**
Volume of CTAB stock	mL	$V_{CTAB} = V_{1prop}^{total} * \frac{C_{CTAB}^{0}}{C_{CTAB}^{1}}$	**0.086**	**0.108**	**0.129**
Stock glycerol	g/g	w_{gly}^{0}	0.500	0.500	0.500
Stock glycerol	g/mL	ρ_{gly}^{0}	1.000	1.000	1.000
Sample glycerol	g/g	w_{gly}^{1}	0.300	0.300	0.300
Sample glycerol	g/mL	$\rho_{gly}^{1} = \left(\rho_{gly}^{0} - \rho_{1prop}\right) \frac{w_{gly}^{1}}{w_{gly}^{0}} + \rho_{1prop}$	0.921	0.921	0.921
Volume of gly stock	mL	$V_{gly} = V_{1prop}^{total} \frac{w_{gly}^{1} * \rho_{gly}^{1}}{w_{gly}^{0} * \rho_{gly}^{0}}$	**0.238**	**0.238**	**0.238**
Volume of 1-propanol	mL	$V_{1prop} = V_{1prop}^{total} - V_{CTAB} - V_{gly}$	**0.106**	**0.085**	**0.063**

Table 2 Mixing table for ternaray preparation with CTAB variation

measured. Next, the bijel casting mixture is prepared with the obtained particle dispersion upon mixing it with stock solutions of CTAB and glycerol in propanol, DEP and water. Example compositions for this are given in Table 2 Fig. 3.7C.

A one-time-use pipette/capillary fiber extrusion device is assembled by inserting a 50 µm round glass capillary into a 200 µL pipette tip. A small amount of Norland 89 UV-glue is filled into the front part of the pipette tip and UV-light is applied. Separately, the bottom of a 2-3 mL glass vial is cut off (for instance with a band-saw) and the vial is attached with 5-min Epoxy glue on a thin microscope coverslip.

The vial is filled with toluene. A small amount of the precursor mixture is added into the pipette tip/capillary device and a pipette is connected. The 50 µm capillary protruding out of the pipette tip is submerged into the toluene filled vial and pressure is applied to flow the precursor mixture into toluene (Fig. 3.10D). After collecting sufficient amount of the fiber, toluene in the vial is decanted and replaced with a saturated solution of Nile Red in hexane (Fig. 3.10E).

The vial is placed on a confocal microscope and a blue laser is used to excite two separate fluorescence signals in the wavelength ranges 500-550 nm and 600-700 nm Fig. 3.10F shows example confocal micrographs obtained via this method for variable CTAB concentrations with compositions given in Table 2.

3.5.4 Scanning electron micrographs of small domain bijels

The structure of the bijel remains intact after 3 *wt* % TEOS treatment for 18 hrs. The following micrographs show the interconnectivity and uniformity of the structure in the radial direction. The vastness of the interwoven tunnel network formed during STrIPS becomes apparent in the electron micrographs of Fig. 3.11. These images were obtained by generating a bijel with 1-propanol as the solvent into toluene. A Phenom Pro Scanning Electron Microscope has been employed for imaging. Dry samples are sputter-coated with platinum (8-10 nm) before imaging.

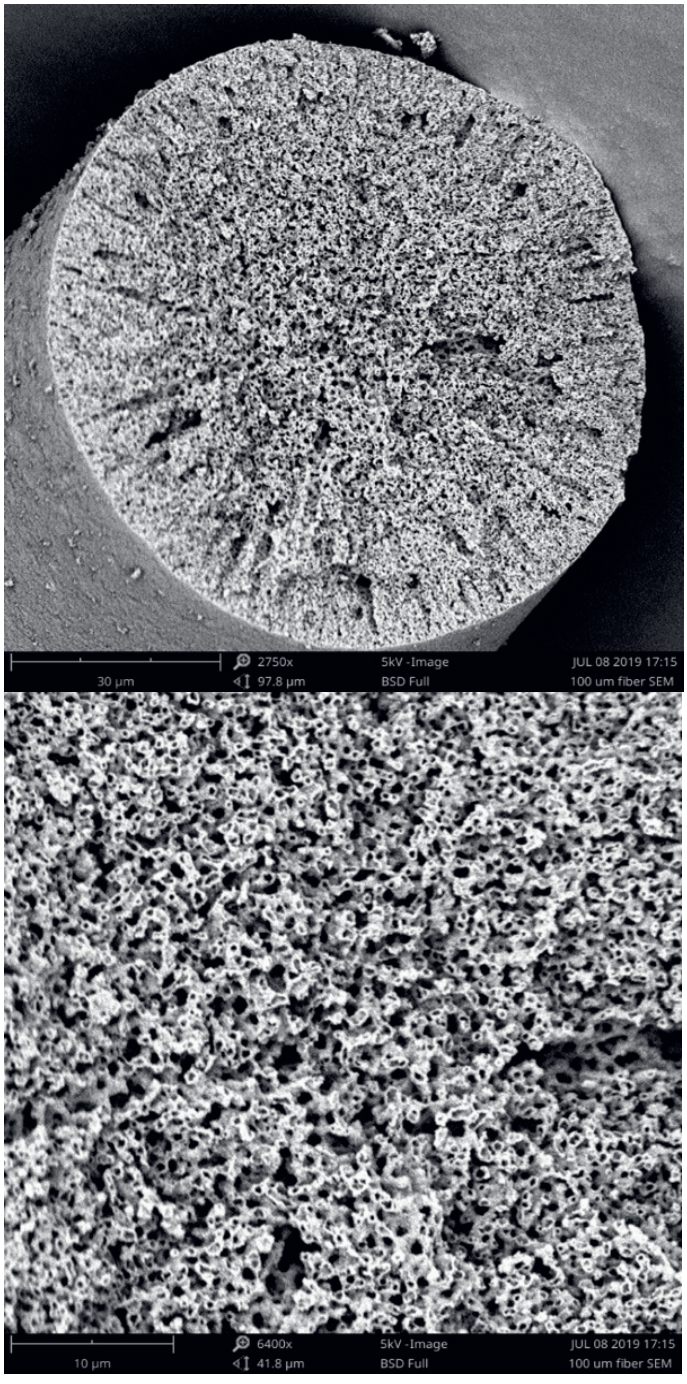

Fig. 3.11 Scanning electron micrographs of 100 µm diameter bijel fiber at different magnifications.

3.5.5 Equilibrium interfacial tension measurements

A pendant drop tensiometer (OCA 200 dataphysics) is used to measure the interfacial tension between water- and oil-rich phases. Fig. 3. 12 A illustrates the experimental procedure.

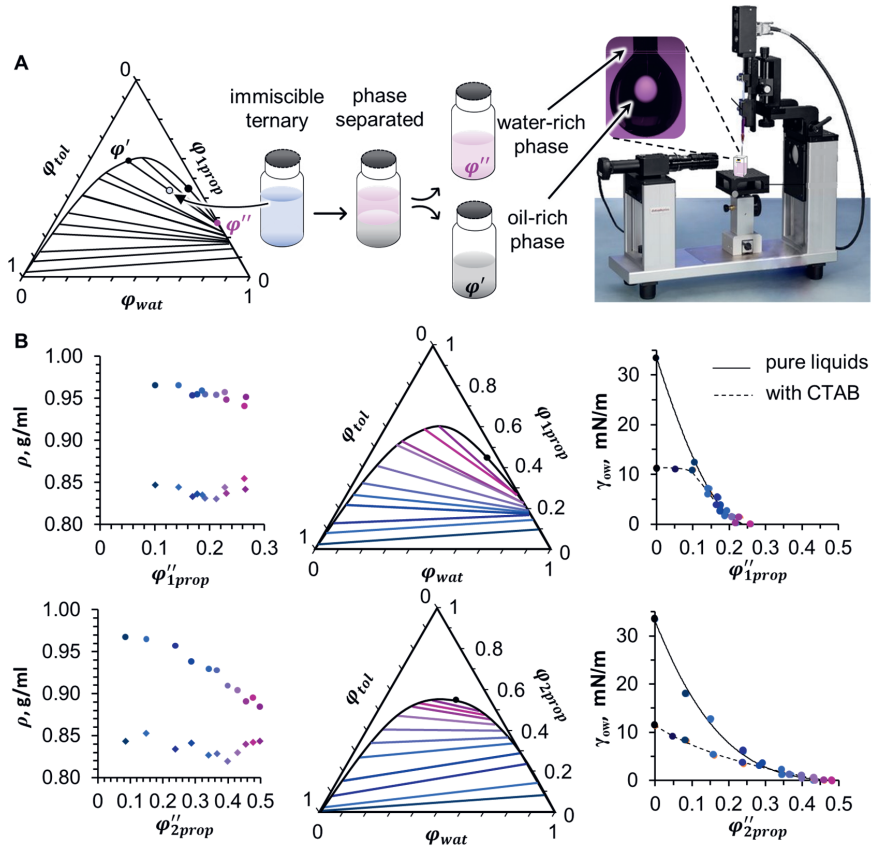

Fig. 3.12 Interfacial tension measurement using pendant drop. (A) Schematic showing the preparation of water- and oil-rich phases. (B) Density measurements of the water- and oil-rich phases, interfacial tensions between water- and oil-rich phases connected via color code to the tie lines in the ternary phase diagram.

A composition in the middle of an arbitrarily chosen tie-line is prepared, equilibrated by shaking for several hours, allowed to phase separate, and separated by decanting. The density of each phase is measured and droplets of the heavier phase are formed in a reservoir of the lighter phase. To include the effect of CTAB on the interfacial tension, we add CTAB and nanoparticles to the water-rich phase. The amount of added CTAB and nanoparticles is the same as in the precursor mixture used to fabricate the bijel. The particles aggregate strongly in the water-rich phase due to CTAB adsorption. The aggregated particles are centrifuged at 18000 rpm for 2 hrs. The interfacial tension of the supernatant containing excess CTAB is measured against the toluene-rich phase. Analysis of the droplet shape

provides the interfacial tension via shape analysis based on the Young-Laplace equation. Fig. 3.12B shows the obtained density and interfacial tension measurements.

3.5.6 CTA^+ effect on the interfacial tension time evolution

The values for the interfacial tension (γ_{ow}) shown in Fig. 3.13 represent equilibrium states between both the ternary liquid mixture compositions of the toluene- and water-rich phases, as well as the interfacial CTA^+ coverage.

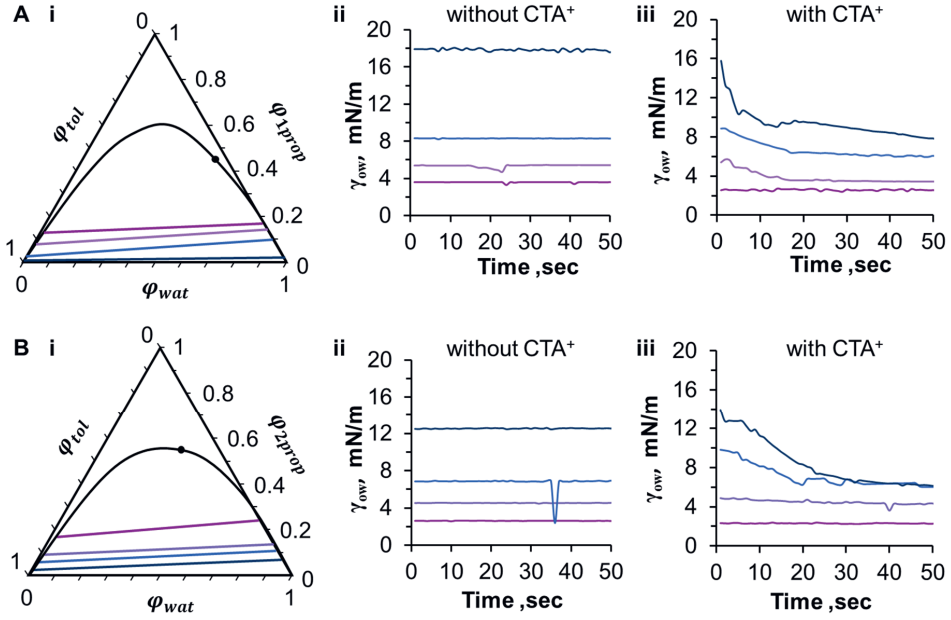

Fig. 3.13 Time dependent interfacial tension ($\boldsymbol{\gamma_{ow}}$) measurements between equilibrated liquid phases. (A) 1-propanol, (B) 2-propanol. The colors of the tie-lines in the ternary diagrams are linked to the curves of $\boldsymbol{\gamma_{ow}}$ against time.

In this section we show that without CTA^+, γ_{ow} reaches the equilibrium rapidly (< 1 second). Moreover, we also show that with CTA^+ it takes several seconds to attain an equilibrium for γ_{ow}. Fig. 3.13B shows the time dependence of γ_{ow} between equilibrated water- and toluene- rich phases with/without CTA^+.

For the measurements, a droplet of the water-rich phase is formed rapidly in the toluene-rich phase (within a few hundred milliseconds). The droplet shape analysis starts immediately to obtain values for

γ_{ow}. We analyze only tie-lines in the lower half of the immiscible region, because the droplets at the higher up tie-lines easily fall off from the needle due to their low values of γ_{ow}.

If the precursor mixtures do not contain CTA^+, γ_{ow} does not change over the course of 10 minutes (Fig 3.13A-ii & B-ii). In contrast, with CTA^+, γ_{ow} can decrease with time. For the two pink tie lines ($\varphi_{prop} > 0.15$), no change of γ_{ow} is observed over time. Here, the elevated propanol volume fraction inhibits the interfacial activity of CTA^+. In contrast, for the blue tie lines ($\varphi_{prop} < 0.15$) a decrease of γ_{ow} is observed with time. The decrease of γ_{ow} can be related to the adsorption kinetics of the CTA^+ molecules to the toluene/water interface.

3.5.7 Interfacial tension evolution for nonequilibrium water- and oil-rich phases

During STrIPS, the compositions of the water- and toluene- rich phases evolve over time. We have modeled this time dependence in Fig 3.4c of the chapter with numerical mass-transfer simulations, predicting the average propanol volume fraction in the water-rich phase (φ''_{pr}) of the fiber (see also Appendix 3.5.6). To estimate the time evolution of the interfacial tension (γ_{ow}) in the fiber, the calculated values for φ''_{pr} have been correlated with the equilibrium values for γ_{ow}. Is this correlation valid? Does a change of φ''_{pr} result in an instantaneous change of γ_{ow} to its equilibrium value? To answer this question, we combine nonequilibrium γ_{ow} measurements with mass transfer simulations in the following.

We measure the nonequilibrium interfacial tension evolution of millimeter sized droplets by video microscopy. To this end, pendant droplets of water-rich compositions are formed in a toluene-rich phase. No CTA^+ is added in these experiments in order to only probe the propanol equilibration. Fig. 3.14A shows the selected compositions for the experiments.

Point (1) at the left end of the blue tie-line in Fig. 3.14A gives the toluene-rich phase composition, which always surrounds the pendant droplet in our experiments. The points (a), (b), (c) give the compositions of the water-rich droplets in the different experiments (increasing φ''_{pr} from (c) to (a)). By forming a droplet of composition (a) in a continuous phase of composition (1), the diffusion of 1-propanol from the droplet to the surroundings begins.

Over time, the initial composition (a) in the droplet evolves along the binodal curve towards the right end-point of the blue tie-line in Fig. 3.14A. The same will occur for droplets of compositions (b) and (c), but smaller amounts of 1-propanol need to diffuse to reach the blue tie-line of the surrounding toluene-rich phase.

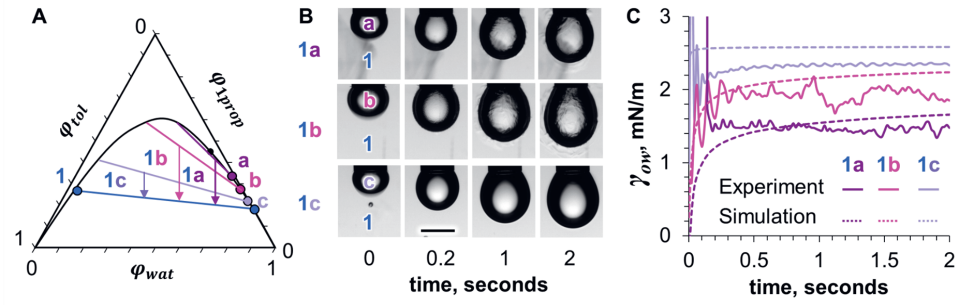

Fig. 3.14 Nonequilibrium interfacial tension measurements and simulations. (A) Ternary phase diagram depicting the initial compositions of the experiments 1a, 1b, and 1c. (B) Pendant drop micrograph time series. In all experiments, the liquid surrounding the droplets is the toluene-rich phase with the composition 1. The droplets are composed of the water-rich phases with compositions a, b, c that are flown out of a 1 mm metal needle at a rate of 1 mL/min. The videos are recorded at a framerate of 50 s^{-1} and the best Young-Laplace fit is determined via image analysis. Based on this and the density difference of water- and toluene-rich phases the interfacial tension is determined. Scale bar 1 mm. (C) Time dependence of the measured interfacial tension for experiments 1a, 1b, 1c. The dashed curves show the simulation results.

Fig. 3.14B shows snapshots of pendant droplets of compositions (a), (b), and (c) at different times. The mass transfer is visible from optical inhomogeneities in the surrounding toluene resulting from refractive index differences. The droplet shapes are fitted with the Young-Laplace equation to obtain γ_{ow} at different times. Fig. 3.C shows the resulting time dependence of γ_{ow}. During the first 200 milliseconds, the droplets oscillate strongly, impeding accurate Young-Laplace fitting of the shape. After 200 milliseconds the more stable droplet shape allows measurements of γ_{ow}. γ_{ow} appears to remain constant after 200 milliseconds. The higher the initial φ''_{pr} in the droplets (compositions (c) to (a)), the lower the value of γ_{ow} after 200 milliseconds.

In the following, Dr. Martin Haase provides comparisons between the experimental time evolution of γ_{ow} from the pendant droplet shape fitting agrees with the calculated values of γ_{ow}. This finding supports the validity of our approach to predict the time evolution of γ_{ow} during bijel formation with equilibrium measurements of γ_{ow} because the calculation for the pendant drop here also combines mass transfer simulations with equilibrium measurements of γ_{ow}.

Fig. 3.15A illustrates mass transfer simulations of pendant droplets with nonequilibrium compositions. The measured shape and size of the experimental droplets are reproduced in the axisymmetric geometry of the simulated pendant droplets Fig. 3.15A. A mesh with extra fine resolution around the droplet interface is formed (Fig. 3.B). Inside and outside of the droplet, concentration dependent diffusion coefficients for 1-propanol in toluene and water are employed. At the droplet interface, the concentration dependent partitioning coefficient of 1-propanol between toluene and water is set as a boundary condition (also taken from Fig. 3. 12B). The initial concentrations in the droplets are chosen

to correspond to points (a), (b) or (c) in Fig. 3.14A. The initial concentration of the toluene outside of the droplet corresponds to point (1) in Fig. 3.15A.

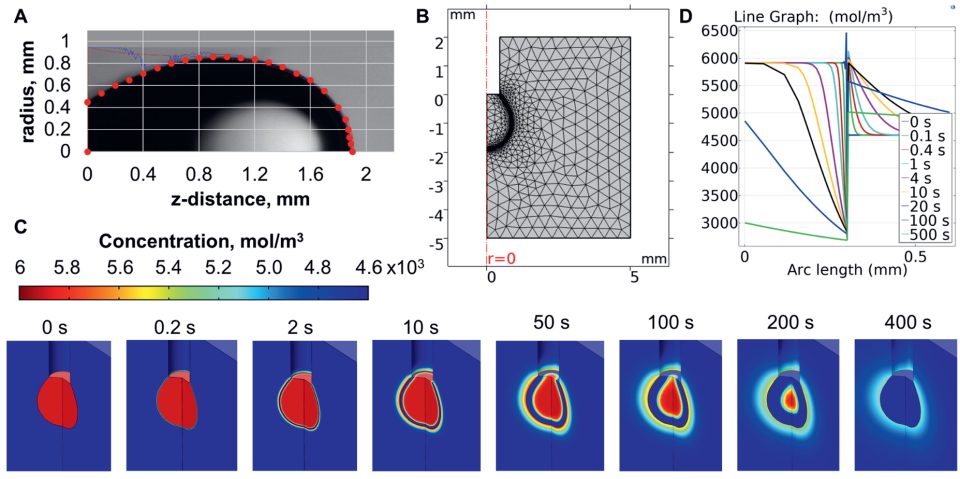

Fig. 3.15 Mass transfer simulation of 1-propanol diffusion from pendant drop. (A) Droplet shape reconstruction. (B) Axisymmetric droplet geometry employed with simulation mesh. (C) 3D-surface plots showing the 1-propanol concentrations at different times. (D) Radial concentration profiles of 1-propanol from the droplet center into the toluene at different times.

Fig. 3.C shows three-dimensional surface plots of the 1-propanol concentration distribution around the droplet for the initial conditions equivalent to the experiment 1a. Within the first few seconds, the concentration inside of the droplet hardly changes. After several tens of seconds also the concentration deeper inside the droplet decreases. In contrast, at the droplet interface the concentration decreases rapidly within a hundred milliseconds from 6000 to 3000 mol/m^3 (Fig. 3.15D). The fast concentration decrease at the interface results from the strong partitioning of 1-propanol to the surrounding toluene-rich phase.

Next, the simulated values for the 1-propanol concentration at the droplet interface of the water-rich side (φ''_{pr}) are used to calculate γ_{ow} with the equilibrium measurements of γ_{ow} from Fig. 3.13. The resulting γ_{ow} time evolution is plotted in Fig. 3.14C alongside with the experimental γ_{ow} dependence from fitting the shape of the nonequilibrium pendant drop during the experiment. Simulation and experimental results agree reasonably well, indicating that the assumption of employing equilibrium values to model the nonequilibrium γ_{ow} evolution is justified. Minor differences between experimental and simulated data likely result from experimental inaccuracies, originating from limited precision of fluid density determination, sample composition preparation and droplet shape fitting errors.

Last, we briefly discuss the concentration and γ_{ow} evolution at longer time scales. The dashed curves in Fig. 3.14A seem to indicate that for each experiment 1a, 1b and 1c different final γ_{ow} value are

reached. This false impression results from the short time scale of the horizontal time axis in Fig. 3.14A. In fact, after several hundreds of seconds all γ_{ow} curves converge at 2.8 mN/m, because only after these prolonged times the 1-propanol is sufficiently diluted by diffusion. Only then will the equilibrium compositions of the toluene- and water- rich phases be attained. Fig. 3.16A shows the short (Fig. 3.16A) and long (Fig. 3.16B) time scale of the 1-propanol concentration evolution of the water- and toluene-rich phases at the interface of the pendant droplets. The convergence of the dashed curves in Fig. 3.16B at 2500 mol/m^3 shows that equilibrium is attained after hundreds of seconds.

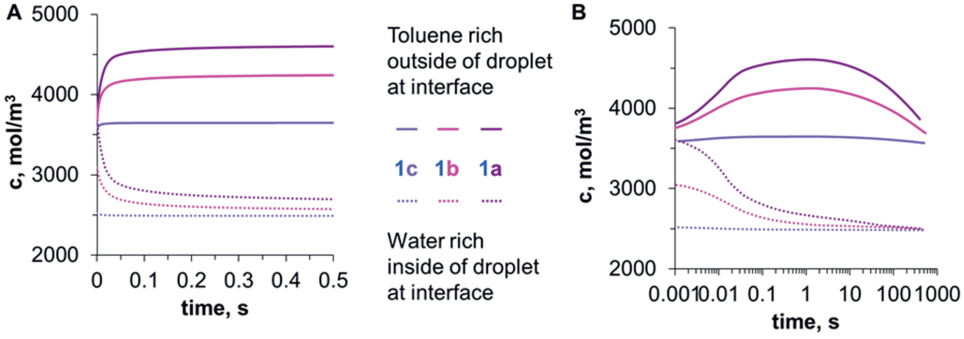

Fig. 3.16 Simulated time dependence of interfacial 1-propanol concentration. (A) Linear time plot for short timescale, (B) Logarithmic time plot for long time scale.

3.5.8 Fluorescence spectra of Nile red

Fig. 3.17 shows spectral scans of the full fluorescence spectra of Nile red in hexane (green) and Nile red adsorbed on the CTAB modified silica nanoparticle scaffold (red).

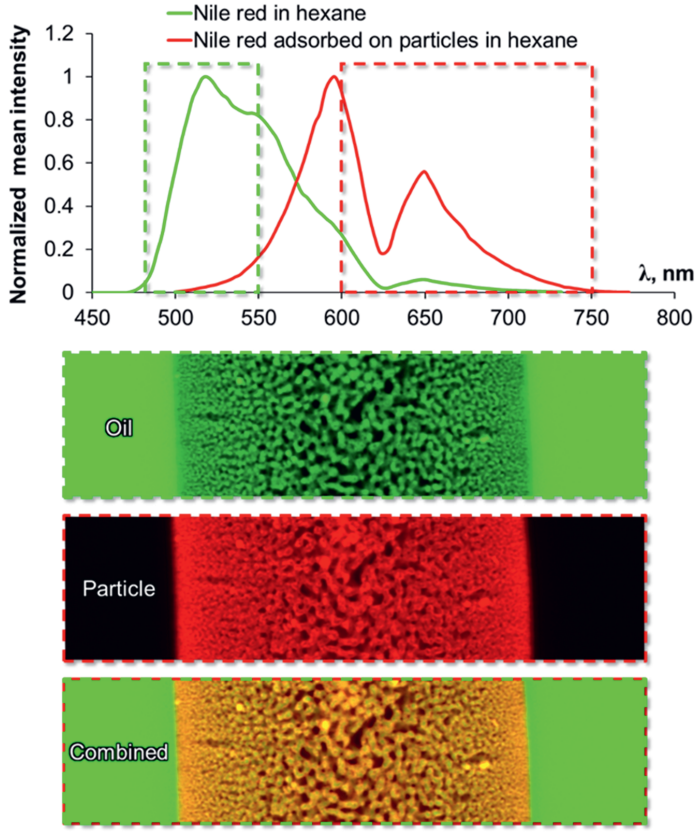

Fig. 3.17 Fluorescence spectra of Nile red in hexane and adsorbed onto the particles.

3.5.9 Surface area analysis and attachment efficiency

We describe a method to measure the specific surface area of the bijel fibers using equatorial plane confocal micrographs of the bijel. Fig. 3.18 shows a confocal micrograph used for the analysis here. The image is processed in ImageJ via the menu “Process”, “FFT”, “Bandpass Filter” to enhance the contrast. Next, an outline of the interface between oil and water is obtained via thresholding the image. The binarized image is now skeletonized via the menu “Process”, “Binary”, “Skeletonize”. Skeletonization turns the network of pixels into lines with a thickness of 1 pixel.

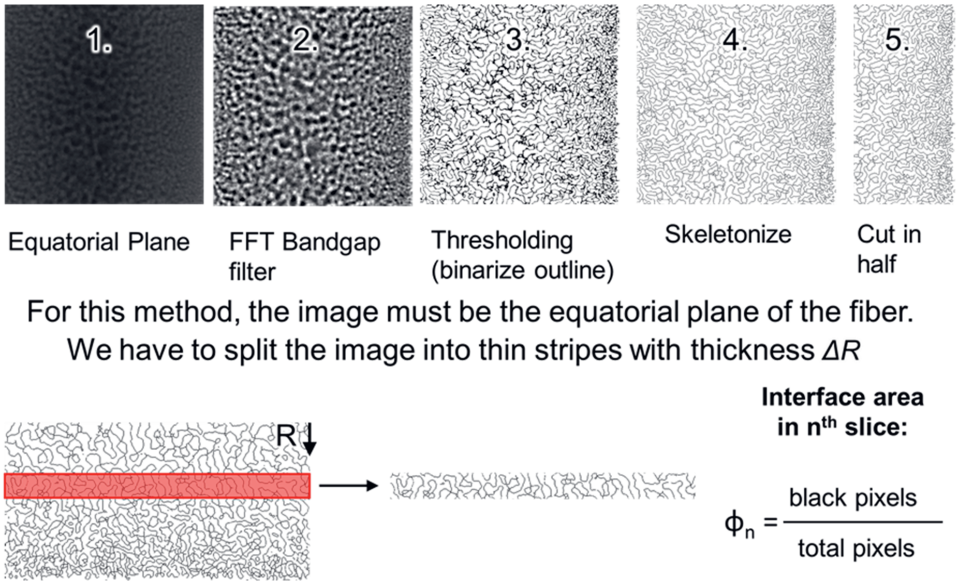

Fig. 3.18 Left: Confocal micrograph of the equatorial plane of bijel fiber. Right: Product of bandpass filter processing (see for geometric considerations)

The skeletonized image is cut in half for further analysis. To analyze the image, the skeletonized half is divided into thin strips with radial positions R_n as depicted in Fig 3.18 Within each strip, the number of pixels is measured and multiplied with the factor converting pixels to µm. Then, the measured value in µm is divided by the area of the strip $\Delta R \cdot L$ to obtain ϕ_n.

This procedure is repeated for all strips of the skeletonized half of the fiber cross-section. The interfacial length in one plane is converted into a surface by rotation via multiplication with $2\pi R_n$. To obtain the specific oil/water interfacial area, the interfacial areas of each ring are added and divided by the total volume of the cylinder.

Next, we measure the attachment efficiency of particles (η) to probe the stability of the particles during the STrIPS upon varying CTA^+ and glycerol concentrations. The attachment efficiency of particles (η) is defined as the percentage of particles attached to the oil-water interface to the total number of particles. We calculate the η by analyzing the confocal micrographs. The maximum number of particles attached to the interface is given by equation (1).

We assume a 2D hexagonal packing (packing factor ε = 90.64) forming a jammed monolayer of particles at the oil-water interface. This is divided by the total number of particles available in the analyzed segment of the fiber (2). The total number of the particles is calculated with the 30 % volume loss correction during the STrIPS bijel fiber formation. Finally, particle efficiency (η) is given by equation (3).

$$N_a \text{ (number of nanoparticles at the surface)} = \frac{A_i^* 90.64}{\pi * R_p^2} \quad (1)$$

$$N_m \text{ (number of nanoparticles in fiber segment volume)} = \frac{w * \rho * V_f}{\rho_{NP} * 4/3 * \pi * R_p^3 * 0.7} \quad (2)$$

$$\text{Attachment efficiency } (\eta) = \frac{N_a}{N_m} * 100\ \% \quad (3)$$

Where N_a and Nm are the numbers of nanoparticles at the interface and in the fiber segment respectively. The particle weight fraction in suspension is w, ρ the density of the Ludox® TMA dispersion. The volume of the fiber is V_f, ρ_{NP} the density of the nanoparticles (2.2 g/mL), R_p is the nanoparticle radius (10 nm).

3.5.10 Analysis of the nanoparticle interfacial attachment energy

A time dependent COMSOL diffusion simulation allows us to predict the decreasing volume fraction of propanol in a fiber undergoing STrIPS. With this information, the time evolution of the interfacial tension and the nanoparticle attachment energy in the phase separating precursor mixture can be calculated. In the following, we do this for both 1- and 2-propanol.

During STrIPS, water and toluene-rich phases are formed. The total volume of the toluene rich phase V' is given by

$$V' = V'_{wat} + V'_{tol} + V'_{prop} \quad (1)$$

And the total volume of the water-rich phase V'' is given by

$$V'' = V''_{wat} + V''_{tol} + V''_{prop} \quad (2)$$

The total volume of propanol in the fiber calculates to

$$V'_{prop} + V''_{prop} = V'\varphi'_{prop} + V''\varphi''_{prop} = (V' + V'')\varphi_{prop} \quad (3)$$

with the propanol volume fractions φ'_{prop} and φ''_{prop} in the toluene- and the water-rich phases, respectively and the overall propanol volume fraction φ_{prop}. Dividing both sides by the total volume $V' + V''$ yields

$$\varphi'\varphi'_{prop} + \varphi''\varphi''_{prop} = \varphi_{prop} \quad (4)$$

with the volume fractions of the toluene- and water-rich phases φ' and φ''.

We will solve this equation later to obtain the time dependence for $\varphi''_{prop}(t)$, allowing us to connect our COMSOL diffusion simulation to interfacial tensions γ_{wo} and nanoparticle attachment energies ΔE_{ow}. To this end, we assume that φ' and φ'' are constant over time. They will be determined by analyzing confocal micrographs of bijel fibers. The equation writes then

$$\varphi'\varphi'_{prop}(t) + \varphi''\varphi''_{prop}(t) = \varphi_{prop}(t) \tag{5}$$

To extract ΔE_{ow} from this model, 5 steps are required:

1. Determination of relationship $\varphi'_{prop}\left(\varphi''_{prop}\right)$
2. Measurement of the toluene- and water-rich phase volume fractions φ' and φ''
3. Calculation of $\varphi_{prop}(t)$ via COMSOL Multiphysics
4. Solve equation (6) for $\varphi''_{prop}(t)$ and $\varphi'_{prop}(t)$
5. Correlate measurements of γ_{wo} with $\varphi''_{prop}(t)$ and calculate ΔE_{ow}

3.5.10.1 Determination of relationship $\boldsymbol{\varphi'_{prop}\left(\varphi''_{prop}\right)}$

We can write a function $\varphi'_{prop}\left(\varphi''_{prop}\right)$ with the ternary phase diagram, by plotting the propanol volume fractions of the tie-line endpoints against each other Fig. 3.18.

$$\varphi'\varphi'_{prop}\left(\varphi''_{prop}(t)\right) + \varphi''\varphi''_{prop}(t) = \varphi_{prop}(t) \tag{6}$$

To express $\varphi'_{prop}\left(\varphi''_{prop}\right)$, linear interpolation functions $\varphi'_{prop} = a_i\varphi''_{prop} + b_i$ between the data points in Fig. 3.13 are evaluated. Equation (7) rewrites then to

$$\varphi''_{prop} = \frac{\varphi_{prop}(t) - \varphi' b_i}{\varphi' a_i + \varphi''} \tag{7}$$

The relation $\varphi'_{prop}\left(\varphi''_{prop}\right)$ assumes that at any given time during STrIPS, the toluene- and water-rich phases are at equilibrium. Then equation [6] writes to

Equation (8) is later solved iteratively to determine the corresponding values of a_i and b_i for φ''_{prop}.

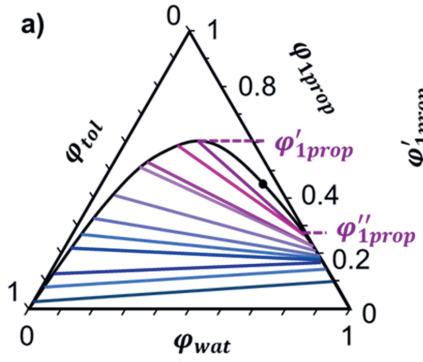

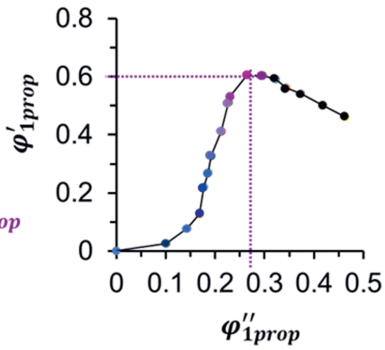

φ'_{1prop}	φ''_{1prop}
0.0266	0.1003
0.0778	0.1430
0.1277	0.1687
0.2197	0.1770
0.2691	0.1864
0.3279	0.1910
0.4126	0.2116
0.5114	0.2275
0.5305	0.2297
0.6063	0.2647
0.6040	0.2950
0.5920	0.3220
0.5010	0.4180
0.4630	0.4630

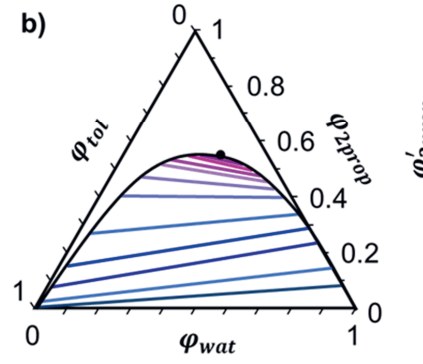

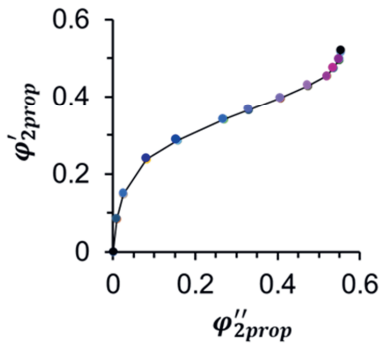

φ'_{2prop}	φ''_{2prop}
0.0098	0.0852
0.0250	0.1491
0.0815	0.2376
0.1560	0.2867
0.2686	0.3401
0.3291	0.3659
0.4060	0.3974
0.4729	0.4287
0.5194	0.4539
0.5350	0.4755
0.5488	0.4950
0.5498	0.5000
0.5532	0.5170

Fig. 3.19 Determination of $\boldsymbol{\varphi'_{prop}}\left(\boldsymbol{\varphi''_{prop}}\right)$ for 1- and 2-propanol from ternary phase diagram

3.5.10.2 **Measurement of the toluene and water rich phase volume fractions φ' and φ''**

φ' and φ'' are measured from confocal microscopy. To this end, confocal micrographs of the equatorial planes of bijel fibers made with 1- and 2-propanol are acquired (Fig. 3. A&B).

The fluorescence signal of Nile red in hexane is inverted to obtain the regions filled with water in the fiber (colored in magenta in Fig. 3.20 A&B). These regions can be binarized via thresholding in ImageJ (Fig. 3.20 A&B). To determine φ', we simplify the problem by assuming rotational symmetry for the water domains.

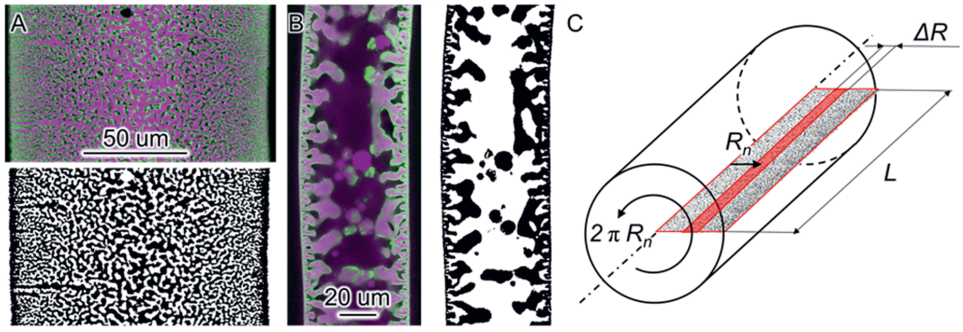

Fig. 3.20 Confocal micrographs of the equatorial plane of cylindrical bijel fiber segments made with (A) 1-propanol and (B) 2-propanol. Magenta color - water, green color - nanoparticles, black color - oil. Binarized images: Black-water (C) Rotational symmetry used to approximate volume fractions.

This approximation neglects the percolating arrangement of the water pores in space, but the error is expected to be low since the rotational symmetry provides an average value of the pore volume. We divide the binarized images of Fig. 3.20A&B into 2 halves. Each of these halves is broken up into stripes at radial positions R_n, with width ΔR, and length L as depicted in Fig. 3.20C. The area fraction of black pixels φ_n in each stripe is measured from the binarized image. The cylindrical geometry then allows calculating the water-rich phase volume V_n' in a cylindrical annulus, which is obtained by rotating the stripe around the central axis

$$V_n' = \varphi_n \cdot \Delta R \cdot L \cdot 2\,\pi \cdot R_n \tag{8}$$

The total volume of the water rich phase V' in a fiber segment is then calculated by summing the volumes of the cylindrical annuli over all R_n values

$$V' = \sum_1^n \varphi_n \cdot \Delta R \cdot L \cdot 2\,\pi \cdot R_n \tag{9}$$

Last, the water- and oil-rich phase volume fractions φ', φ'' are obtained by dividing V' with the total cylinder volume

$$\varphi' = \frac{\sum_1^n \varphi_n \cdot \Delta R \cdot L \cdot 2\,\pi \cdot R_n}{\pi \cdot R^2 \cdot L} \tag{10}$$

This analysis results in $\varphi' = 0.782$ (1-propanol) and $\varphi' = 0.371$ (2-propanol) ($\varphi'' = 1 - \varphi'$).

3.5.10.3 Calculation of $\varphi_{prop}(t)$ via COMSOL multiphysics

To obtain concentration profiles for propanol in the precursor mixture and the surrounding toluene a transient diffusion simulation is employed. To this end, a COMSOL Multiphysics simulation with the physics engine "Transport of Diluted Species" is introduced in the following. The model neglects the influence of the laminar flow around the bijel fiber on the diffusion process. The laminar flow layers can "smear" out the concentration of propanol c_{prop} due to the different flow velocities in radial direction, a phenomenon known as Taylor dispersion. However, by performing a COMSOL simulation coupling flow and diffusion, we find that for the present flow geometry, dimensions and velocities the flow has only a small influence on the diffusion process. Therefore, a simplified model is employed here. The

simplified model uses only Fick's second law of diffusion, describing c_{prop} in the precursor mixture and the surrounding toluene with the differential equation

$$\frac{\partial c_{prop}}{\partial t} = D_{prop}\frac{\partial^2 c_{prop}}{\partial r^2} \tag{11}$$

To describe the fiber during extrusion we use axis-symmetric cylindrical coordinates (Fig. 3.21A).

A cylinder with a diameter of 50 µm is placed inside a larger cylinder of 300 µm. The inner cylinder represents the precursor mixture, the outer cylinder is the toluene filled glass capillary into which the precursor mixture flows. At the beginning of the simulation (t = 0), the inner cylinder has a concentration of $c^0_{1prop} = \frac{\varphi^0_{1prop}\cdot\rho_{1prop}}{M_{1prop}} = \frac{0.43\cdot 790\frac{kg}{m^3}}{0.0601\frac{kg}{mol}} = 5652\,\frac{mol}{m^3}$ for the simulation with 1-propanol and a concentration of $c^0_{2prop} = \frac{\varphi^0_{2prop}\cdot\rho_{2prop}}{M_{2prop}} = \frac{0.5\cdot 790\frac{kg}{m^3}}{0.0601\frac{kg}{mol}} = 6572\,\frac{mol}{m^3}$ for the simulation with 2-propanol. The outer cylinder has an initial concentration of 0 mol/m^3 for both 1- and 2-propanol. We refine the transient diffusion model by considering (i) concentration dependent diffusion coefficients, (ii) a thin diffusion barrier on the surface of the fiber to model the smaller bijel surface pores, and (iii) partitioning coefficients for propanol between water and toluene.

(i) The concentration dependence of the diffusion coefficients D_{prop} for both 1-propanol in water and toluene are plotted in Fig. 3.21B. [34, 35]

For the diffusion simulation, D_{prop} is evaluated via linear interpolation functions between the data points in Fig. 3.21B to solve the equation

$$\frac{\partial c_{prop}}{\partial t} = D_{prop}\big(c_{prop}\big)\frac{\partial^2 c_{prop}}{\partial r^2} \tag{12}$$

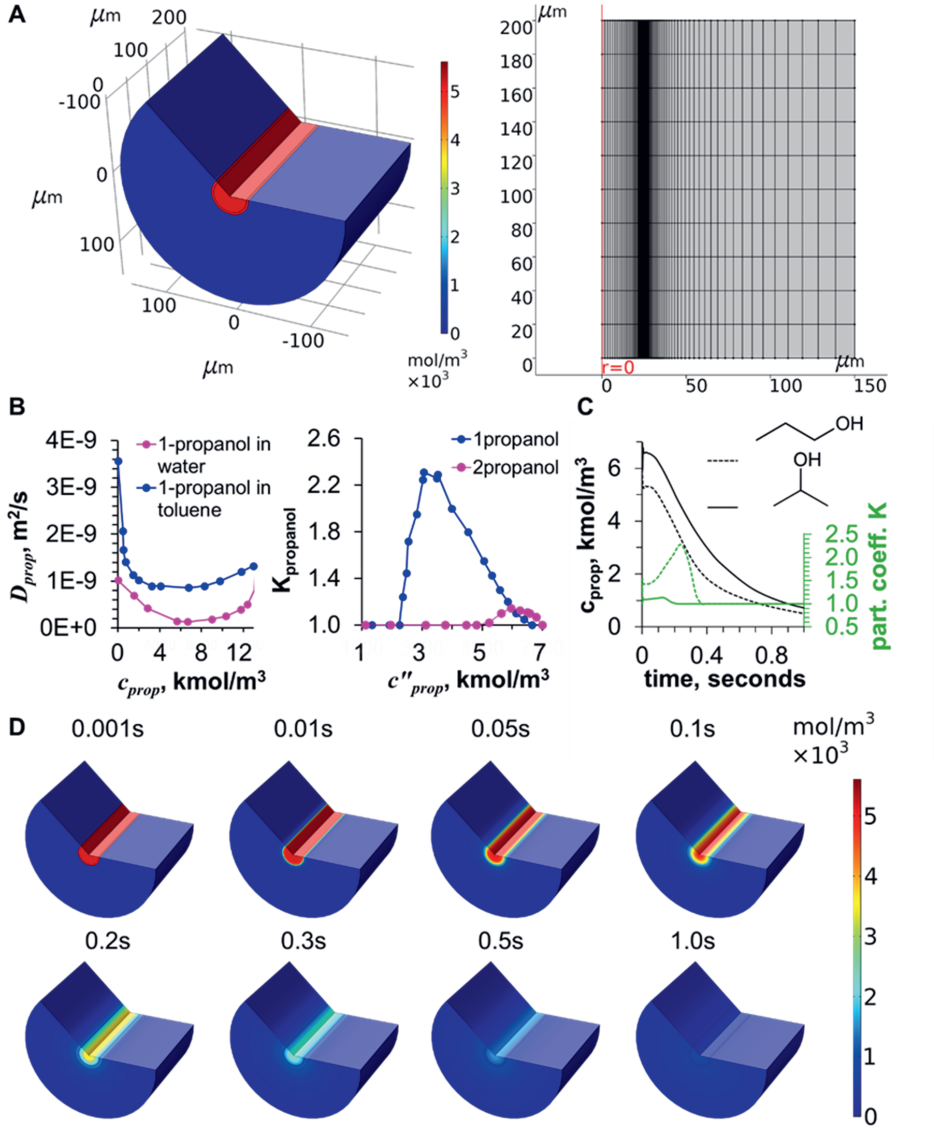

Fig. 3.21 (A) Cutaway 3D drawing of a short fiber segment at the beginning of the simulation (t = 0) and Mesh representing nodes for the numerical calculation of the concentrations used in the simulation. (B) Diffusion coefficients for 1-propanol in toluene and water in dependence of the propanol concentration and partitioning coefficients for 1- and 2-propanol in water and toluene in dependence of the propanol concentration in the water-rich phase. (C) Center concentration and partitioning coefficient from the COMSOL simulation over time. (D) 3D concentration plots of 1-propanol in and around the fiber

The diffusion coefficients for 1- and 2-propanol do not differ significantly in toluene. Thus, we employ $D_{1prop,tol} = D_{2prop,tol}$ in the blue region outside of the fiber in Fig. 3.21A. Also in water the diffusion coefficients for 1- and 2-propanol do not differ significantly and we employ $D_{1prop,wat} = D_{2prop,wat}$. For the region inside of the fiber (red in Fig. 3.21A) we define an average diffusion coefficient $D_{prop,av} = \left[D_{prop,wat}(c_{prop}) + D_{prop,tol}(c_{prop})\right]/2$ for both 1- and 2-propanol.

(ii) Thin diffusion barrier on the surface of the fiber: The bijel fiber typically forms a surface covered with silica particles with reduced porosity. To account for this in the model, we assume over a thickness of 3 µm below the fiber surface a diffusion coefficient of $D_{prop,av} = \left[D_{prop,wat}(c_{prop}) + D_{prop,tol}(c_{prop})\right]/6$.

(iii) Partitioning coefficients for propanol between water and toluene: The partitioning coefficient is defined as $K_{prop} = \frac{c'_{prop}}{c''_{prop}}$ with c'_{prop} and c''_{prop} the molar concentrations of propanol in the toluene-, and the water-rich phase, respectively. The ternary phase diagram provides the basis for determining K_{prop}. To obtain the molar concentrations from the volume fractions, we employ the formulas $c'_{prop} = \frac{\varphi'_{prop} \cdot \rho_{prop}}{M_{prop}}$ and $c''_{prop} = \frac{\varphi''_{prop} \cdot \rho_{prop}}{M_{prop}}$ with ρ_{prop} and M_{prop}, the density and molar mass of propanol, respectively. K_{1prop} and K_{2prop} are plotted against c''_{prop} in Fig. 3.21B. K_{1prop} reaches values values larger than 2 due to the strongly inclined tie-lines near the critical point, while K_{2prop} remains close to 1 at all concentrations. In COMSOL, a partitioning condition is employed on the surface of the fiber. The concentration dependence of K_{1prop} or K_{2prop} is modelled by using the concentration c_{prop} in the center of the fiber as reference.

The resulting center concentration and the partitioning coefficient in the fiber from the COMSOL simulation are plotted over time in Fig. 3.21C. The partitioning effect takes place during the first 300 milliseconds for 1-propanol whereby it is almost absent for 2-propanol. The 3-dimensional distribution of the 1-propanol concentration evolution is shown in Fig. 3.21D. The radial concentration profiles are plotted in Fig. 3.21A. 1-propanol has a lower starting concentration compared to 2-propanol due to the lower critical point in the ternary phase diagram. The partitioning effect is visible for 1-propanol at 0.2 seconds by the jump in the profile at r = 25 µm. It takes about 2 seconds for both 1- and 2-propanol until the propanol concentration reaches close to 0.

From the radial concentration profiles in Fig. 3.22A we can determine the volume fractions $\varphi_{prop}(t)$ of 1- and 2-propanol in the fiber:

$$\varphi_{prop}(t) = \frac{\int_0^L \int_0^{2\pi} \int_0^R \varphi_{prop}(r,t) \cdot r dr \cdot d\theta \cdot dz}{\int_0^L \int_0^{2\pi} \int_0^R r dr \cdot d\theta \cdot dz} = \frac{M_{prop}}{\rho_{prop}} \frac{\int_0^{2\pi} \int_0^R c_{prop}(r,t) r dr d\theta}{\pi R^2} \quad (13)$$

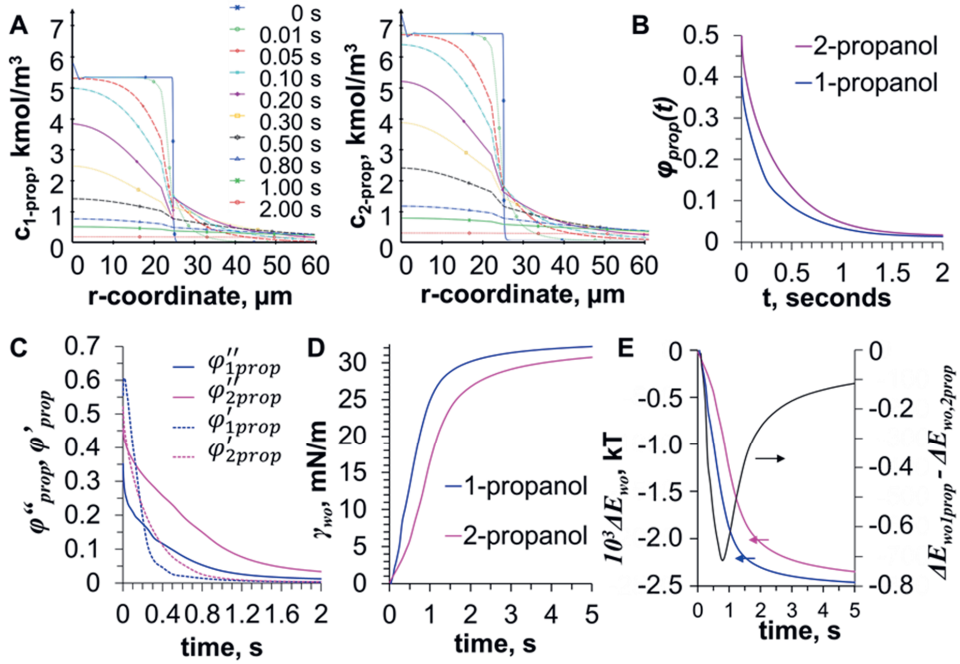

Fig. 3.22 (A) Radial concentration profiles of 1-propanol (left) and 2-propanol (right). (B) $\boldsymbol{\varphi_{prop}(t)}$ over time, obtained by integrating the concentration profiled from the COMSOL simulations. (C) Time dependence of $\boldsymbol{\varphi''_{prop}}$ and $\boldsymbol{\varphi'_{prop}}$ for 1- and 2-propanol. (D) Calculated time evolution of the interfacial tension $\boldsymbol{\gamma_{wo}}$ within the precursor mixture (here no CTAB considered, but in manuscript with CTAB). (E) Calculated interfacial attachment energy $\boldsymbol{\Delta E_{wo}}$ of 20 nm particles with a contact angle of 90°. Arrows indicate the corresponding y-axis.

With $\varphi_{prop}(r,t)$ the local volume fraction, r the radius coordinate, θ the angular coordinate, z the axial coordinate, R the outer radius of the fiber, L the length of the analyzed fiber segment, and $c_{prop}(r,t)$ the local propanol concentration. The integration step is done in COMSOL and results in $\varphi_{prop}(t)$ plotted against the time in Fig. 3.22B.

3.5.10.4 Solve the equation for $\varphi''_{prop}(t)$ and $\varphi'_{prop}(t)$

We can now solve equation (8) $\varphi''_{prop} = \frac{\varphi_{prop}(t) - \varphi' b_i}{\varphi' a_i + \varphi''}$ with the known $\varphi_{prop}(t)$, φ', a_i and b_i from the dependency $\varphi'_{prop}(\varphi''_{prop})$. This is done iteratively in Excel, by implementing an if/elseif algorithm (if $\varphi''_{prop}<$ value_1, then a_1 and b_1, elseif $\varphi''_{prop}<$ value_2, then a_2 and b_2, elseif …). The resulting volume fractions $\varphi''_{prop}(t)$ and $\varphi'_{prop}(t)$ are plotted in Fig. 3.22C. The 1-propanol fraction in the water-rich phase $\varphi''_{1prop}(t)$ starts at a lower value and decreases more rapidly than $\varphi''_{2prop}(t)$. This results

directly from the higher slope of the tie-lines of the ternary diagram for 1-propanol, toluene and water. Next, the measurements of the interfacial tension γ_{wo} (Section 3) are correlated with $\varphi''_{1prop}(t)$.

2.1.1.1 Correlate measurements of γ_{wo} with $\varphi''_{prop}(t)$ and calculate ΔE_{ow}

With the data in Fig. 3.12 the values for $\varphi''_{prop}(t)$ from Fig. 3.22C can now be converted into values of $\gamma_{wo}(t)$. The resulting time dependence of γ_{wo} is plotted in Fig. 3.22D **(**with γ_{wo} measurements excluding CTAB)**.** γ_{wo} increases significantly faster for STrIPS employing 1-propanol as compared to 2-propanol as the solvent. This results directly from the faster decrease of φ''_{1prop} compared to φ''_{2prop} shown in Fig. 3.22C**.** With the time dependency of γ_{wo}, ΔE_{wo} can now be calculated with the formula

$$\Delta E_{wo} = -\gamma_{wo} \cdot r^2 \cdot \pi \cdot (1 - \cos\theta)^2 \tag{14}$$

With r the radius of the particle, and θ the contact angle. For nanoparticles of $\theta = 90° = \pi/2$ the relationship simplifies to $\Delta E_{wo} = -\gamma_{wo} \cdot r^2 \cdot \pi$, which is plotted in Fig. 3.22E.

The absolute value of $\Delta E_{wo,1prop} > \Delta E_{wo,2prop}$ by several hundred kT during the first seconds of STrIPS (see secondary y-axis Fig. 3.22E). This provides an explanation why the bijel formed with 1-propanol shows smaller and more uniform pore sizes over the fiber radius.

3.5.11 CTAB variation at pH -3

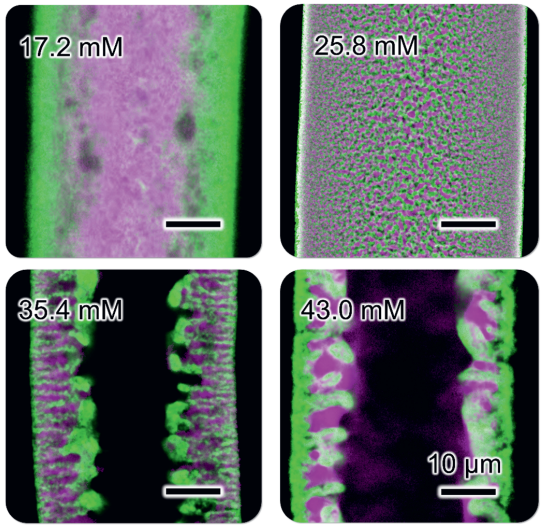

Fig. 3.23 shows the CTAB concentration variation at pH 3. Precursox mixtures are made with different concentrations (17.2, 25.8, 35.4, 43.0 mM). Bijel fibers are made using microfluidic extrusions and washed with hexane having Nile red to acquire the confocal images. Confocal images of the fiber equatorial planes are captured to show the domain size gradient in the radial direction as we increase the concentration of CTAB.

Fig. 3.23 Equatorial plane confocal images of bijel fibers with varying CTAB concentration at pH -3

3.5.12 CTAB partitioning between water- and toluene-rich phases

These experiments are carried out with the help of Dr. Katherine A Macmillan. The partitioning of the CTAB surfactant between the water-rich and toluene-rich phases of unstable precursor mixtures prepared with 1-propanol or 2-propanol was determined. First, the unstable mixtures containing 2 *wt*% CTAB are prepared at the midpoint of selected experimental tie lines (Fig. 3.24A). These mixtures are then shaken overnight on a shaker plate before being left to stand until the two phases have separated. A sample of the toluene-rich and water-rich phase for each unstable mixture is then placed in a preweighed vial and weighed. The liquid phase is then evaporated off by first heating on a hotplate at 120 °C then drying fully in a drying oven at 115 °C. Once the samples are cool, they were weighed again

to determine the mass of CTAB in each phase. Fig. 3.24B shows images of the phase-separated mixtures and dried CTAB in each phase. From the mass of CTAB, the mass of the liquid mixture, and also the density values determined for the different phases Fig 3.24A), the CTAB concentration (c_{CTAB}) in each phase was determined. From the concentrations, the partition coefficient ($K_{tw,CTAB}$) can then be determined.

$$K_{tw,CTAB} = \frac{c_{CTAB,tol}}{c_{CTAB,wat}} \quad (15)$$

The partition coefficient values found are shown in Fig. 3.24C values of the partition coefficient above 1 indicate that there is more CTAB in the oil-rich phase and values of the partition coefficient below 1 indicate that there is more CTAB in the water-rich phase.

Fig. 3.24C shows that for 1-propanol the values of the partition coefficient increase to above 1 when the volume fraction of 1-propanol in the water-rich phase is above approximately 0.2. This then indicates that at the higher mass fractions of 1-propanol the CTAB partitions into the oil-rich phase. In contrast, for 2-propanol the CTAB remains predominantly in the water-rich phase because the values of the partition coefficient all remain below 1.

These measurements show that the CTAB solubility in the oil-rich phase is increased when using 1-propanol rather than 2-propanol as the solvent. The solubility increase can be explained by the strong partitioning of the 1-propanol into the oil-rich phase.

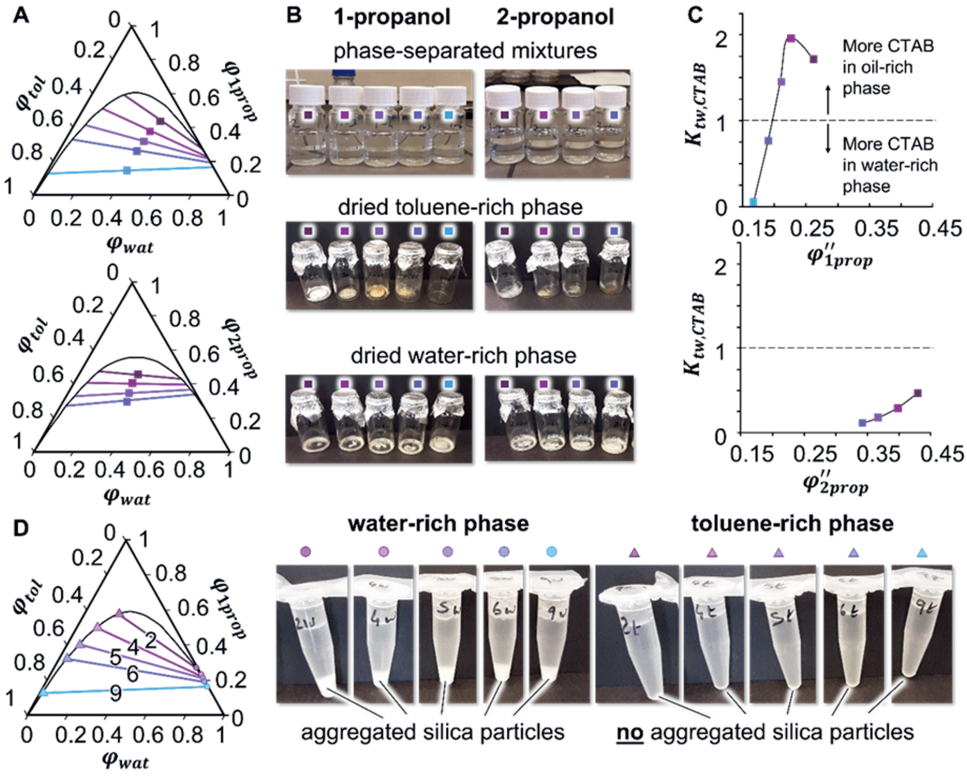

Fig. 3.24 (A) Ternary phase diagrams with mid tie line points (B) Photographs of the phase-separated mixtures and the dried CTAB from each phase for 1-propanol and 2-propanol. (C) Graphs showing the CTAB partition coefficient determined from phase-separated mixtures with compositions at the end points of the tie-lines (given by the color code) plotted against the propanol volume fraction in the water-rich phase φ''_{prop}. (D) The ternary diagram for water/toluene/1-propanol showing the chosen tie lines and compositions of the oil-rich and water-rich phases. Photographs showing the particle dispersions in the oil-rich (t) and the water-rich (w) phases

The particle stability in the oil-rich phase and water-rich phase for the system water/toluene/1-propanol was determined. First, the particles were transferred from water into 1-propanol. This was achieved by first mixing a stable dispersion of particles in water with 1-propanol and a small quantity of CTAB. This mixture was then dialyzed overnight twice to ensure the water and CTAB was removed from the suspension.

The compositions of the oil-rich phase and water-rich phase for chosen tie lines were prepared using the particles dispersed in 1-propanol. The CTAB concentration was varied for a fixed low particle mass fraction (1 *wt*%) for both the oil-rich and water-rich phases of one tie line to determine whether a stable particle suspension could be produced. A stable particle suspension was found for the oil-rich phase at

90 mM CTAB but only aggregated particles were observed for the water-rich phase. The same CTAB concentration was used for the oil-rich and water-rich phases for a selection of tie lines (see Fig. 3.24D). The results show that the particles were stable in the oil-rich phase but not in the water-rich phase for all the compositions tested. This finding indicates that the particles are less aggregated in an oil-rich phase compared to a water-rich phase.

3.5.13 Emulsion inversion for 1-propanol with CTAB

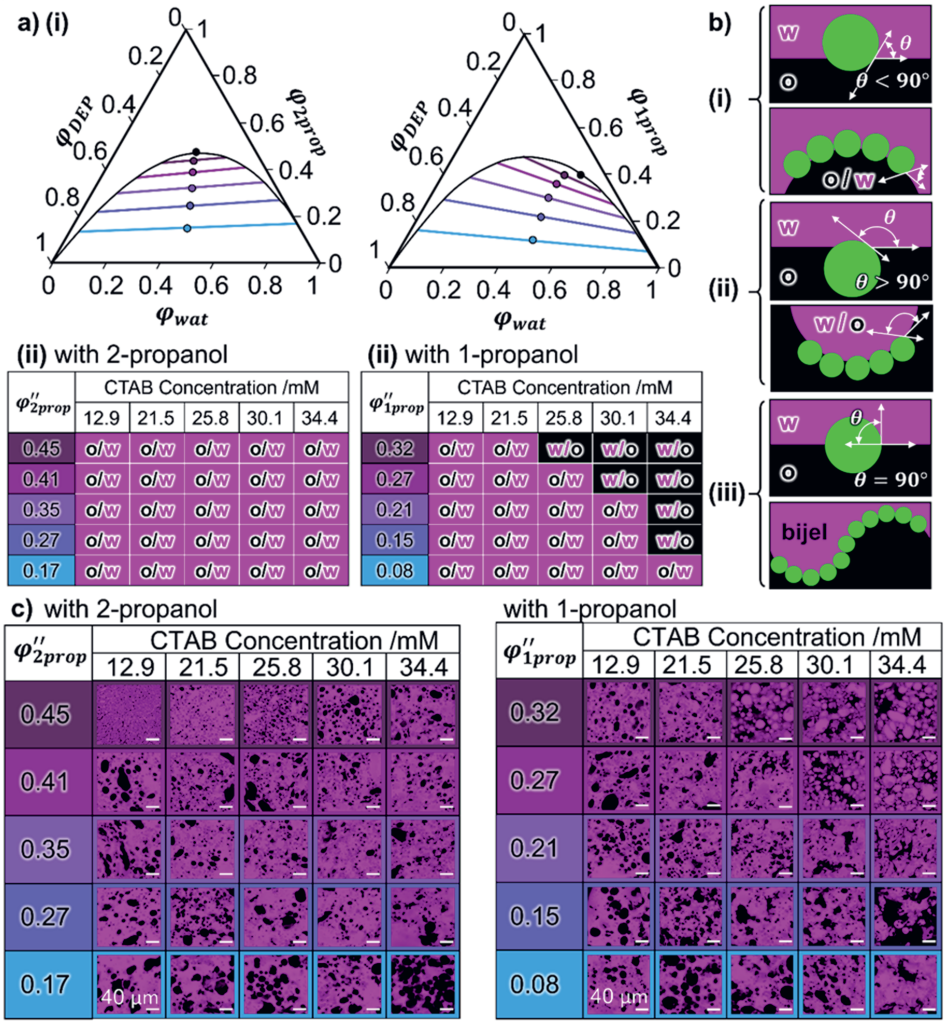

Fig. 3.25 (A) (i) The ternary phase diagrams for 2-propanol and 1-propanol with water and DEP showing the midpoints of the tie lines that were the chosen compositions for the emulsion inversion

experiments and (ii) the resulting emulsion type for 2-propanol and 1-propanol with CTAB concentration. (B) A diagram showing the how the contact angle the particle makes at an oil-water interface influences the type of emulsion formed for (i) hydrophilic particles, (ii) hydrophobic particles and (iii) neutrally-wetting particles. (C) Tables showing the confocal microscope images obtained for the emulsions prepared at the given compositions with CTAB concentration. The water-rich phase is colored magenta and the oil-rich phase is colored black.

The particle contact angle can, in turn, determine the type of emulsion formed by inducing a curvature on the interface (see Fig. 3.25B). By determining the type of emulsion formed with different surfactant concentrations, we can observe how the particles change hydrophilicity with the surfactant concentration. By extending this to include different starting ternary compositions, we can observe if and how the particle hydrophilicity changes with the composition and thus with the phase separation during STrIPS. The ternary diagrams in Fig. 3.25A show the chosen midpoints of the tie lines which are used as the compositions for the precursor mixtures prepared. The CTAB concentrations used for each experiment are 0 mM, 12.9 mM, 21.5 mM, 25.8 mM, 30.1 mM and 34.4 mM in the precursor mixture which correspond to 0 mM, 30 mM, 50 mM, 60 mM, 70 mM and 80 mM in the 1-propanol fraction of the ternary at the composition we use to make bijels for 1-propanol. The same volume of the same particle suspension is used in every precursor mixture to keep the particle mass constant. This corresponds to 35.5 *wt*% of particles in the water fraction of the ternary at the composition we use to make bijels for 1-propanol. For these experiments, 1 mL of each precursor mixture is prepared.

First, the solid CTAB is weighed out into each sample tube followed by adding the desired volumes of 1- or 2-propanol and 50 *wt*% glycerol in 1- or 2-propanol. Next, the CTAB is dissolved into the solvent by sonication. The DEP labelled with nile red is then added followed by the particles and the water. The samples are first hand shaken to mix then vortex mixed. A small droplet of each formed emulsion is placed on a cover slide with a second cover slide placed on top. These are then viewed using a Leica Stellaris confocal microscope and a 561 nm laser to excite the nile red dye.

Fig. 3.25A and C show the results of this study for 1- and 2-propanol. For 1-propanol, there is an obvious transition from oil-in-water emulsions (hydrophilic particles) at low CTAB concentrations to water-in-oil emulsions (hydrophobic particles) at higher CTAB concentrations. As the 1-propanol content in the water phase decreases, the CTAB concentration where the emulsion inverts increases. This indicates that the particles are more hydrophobic at earlier stages of the phase separation. For 2-propanol, only oil-in-water emulsions were observed indicating that the particles are hydrophilic for all the CTAB concentrations measured. These results can be explained by the CTAB partitioning strongly into the oil-rich phase for 1-proponal compared to for 2-propanol.

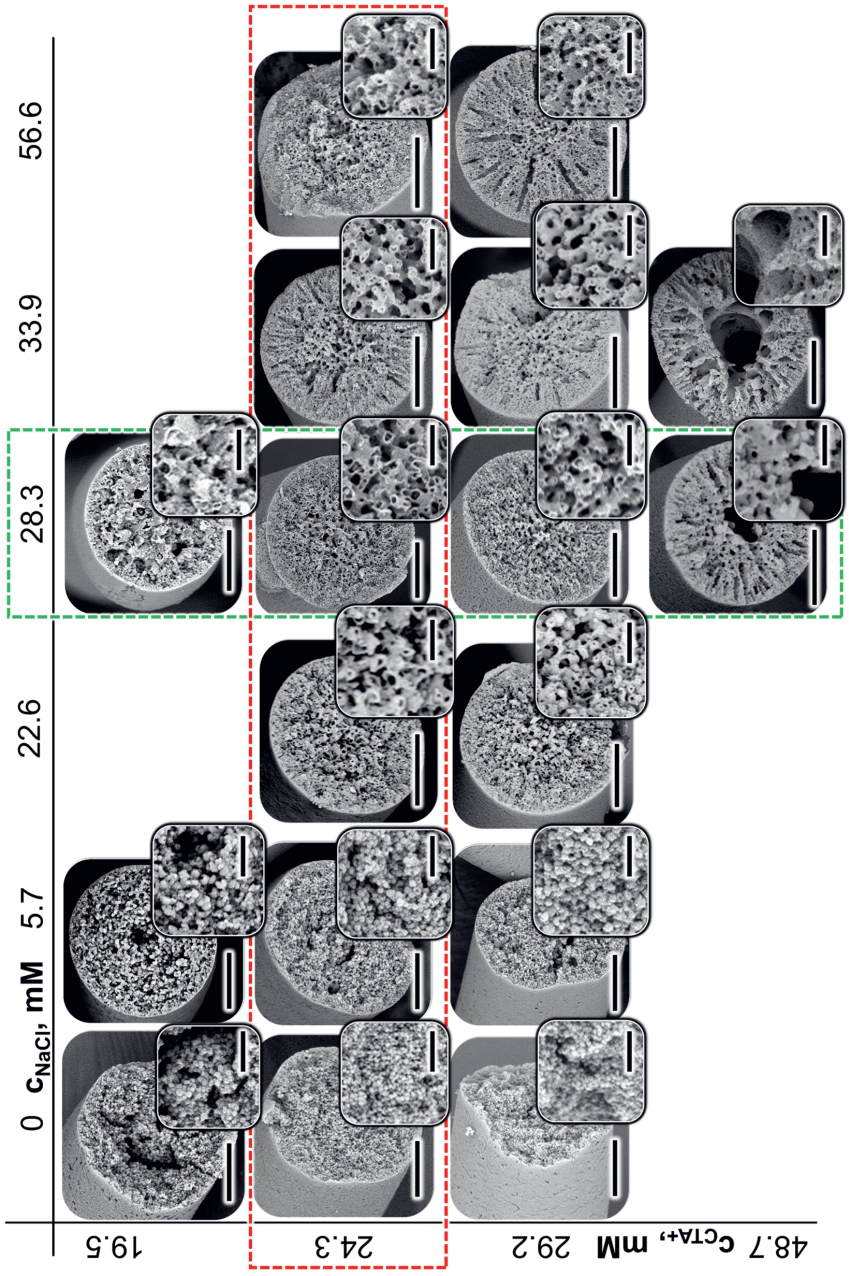

Fig. 3.26 Effect of salt and CTA^+ variation on bijel structure at pH 3. Scale bars are 20 µm for the main micrographs and 5 µm for the insets.

3.5.14 Salt and CTAB concentration variation

To evaluate the effect of surfactant and salt concentration on the STrIPS process and resultant bijel structure we varied both variables at constant pH of 3. As described in Fig. 3.26 Ludox TMA particles are dialyzed at pH 3 with varying concentrations of salt. For each background salt concentration, precursor mixtures are prepared with varying CTAB concentrations. At low salt and CTAB concentrations, precursor mixtures are mostly phase separated whereas above optimal concentration aggregation of particles is observed in the ternary. The following table shows the structural variation upon CTAB and salt variation at pH 3.

3.5.15 Surface pore size modulation via post-processing

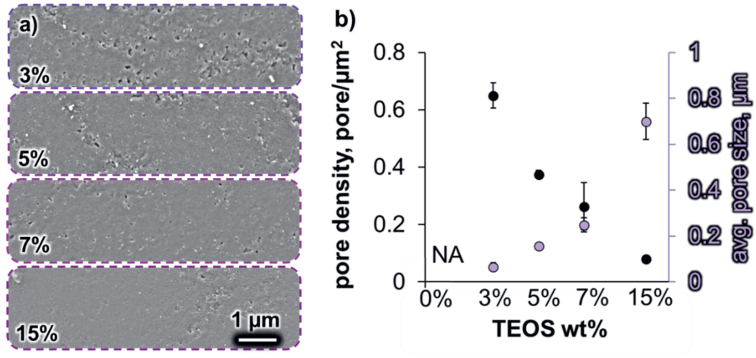

Fig. 3.27 Surface pore tuning with TEOS treatment a) SEM micrographs show the effect of TEOS treatment on the surface pores of bijel fiber.b) Shows the effect of pore density and average pore size as a function of TEOS concentration.

We also discuss the post-fabrication surface pore modification of the bijel. Vintantonio *et al.* has introduced tetraethyl orthosilicate (TEOS) mediated crosslinking of silica nanoparticles at the interface to impart additional mechanical strength [5].In our experiments, we introduce TEOS to the bulk oil phase and via diffusion reactive deposition of silica happens at the oil water interface of bijel. The ease of post-processing allows large variations of TEOS concentration. Nanoparticles crosslinking is required especially when we wash away the constituent immiscible liquid phases and dry the silica monolith. In the absence of the oil-water interface particles just fall apart and do not support the porous structure. Fig 3.27 shows as we increase the TEOS concentration the smaller surface pores get clogged hence the pore density decreases and the average pore size increases. This tuning of the surface pores could be very useful for tailored applications in purification and separation processes.

3.6 Bibliography

[1] R. Freeman, M. Han, Z. Álvarez, J. A. Lewis, J. R. Wester, N. Stephanopoulos, M. T. McClendon, C. Lynsky, J. M. Godbe, H. Sangji, E. Luijten, S. I. Stupp, Science 2018, 362, 808.
[2] K. Stratford, R. Adhikari, I. Pagonabarraga, J.-C. Desplat, M. E. Cates, Science 2005, 309, 2198.
[3] E. M. Herzig, K. White, A. B. Schofield, W. C. Poon, P. S. Clegg, Nature materials 2007, 6, 966.
[4] M. F. Haase, H. Jeon, N. Hough, J. H. Kim, K. J. Stebe, D. Lee, Nature communications 2017, 8, 1.
[5] G. Di Vitantonio, T. Wang, M. F. Haase, K. J. Stebe, D. Lee, ACS nano 2018, 13, 26.
[6] M. N. Lee, A. Mohraz, Advanced Materials 2010, 22, 4836.
[7] D. Cai, F. H. Richter, J. H. Thijssen, P. G. Bruce, P. S. Clegg, Materials Horizons 2018, 5, 499.
[8] M. A. Santiago Cordoba, J. S. Spendelow, A. N. G. Parra‐Vasquez, L. A. Kuettner, P. M. Welch, C. E. Hamilton, J. A. Oertel, J. G. Duque, E. J. Meierdierks, T. A. Semelsberger, Advanced Functional Materials 2020, 30, 1908383.
[9] S. P. Kharal, R. P. Hesketh, M. F. Haase, Advanced Functional Materials 2020, 30, 2003555.
[10] T. J. Thorson, E. L. Botvinick, A. Mohraz, ACS biomaterials science & engineering 2018, 4, 587.
[11] P. S. Clegg, *Bijels: Bicontinuous Particle-stabilized Emulsions*, Vol. 10, Royal Society of Chemistry, 2020.
[12] J. W. Tavacoli, J. H. Thijssen, A. B. Schofield, P. S. Clegg, Advanced Functional Materials 2011, 21, 2020.
[13] C. Huang, J. Forth, W. Wang, K. Hong, G. S. Smith, B. A. Helms, T. P. Russell, Nature nanotechnology 2017, 12, 1060.
[14] M. F. Haase, K. J. Stebe, D. Lee, Advanced Materials 2015, 27, 7065.
[15] S. Boakye-Ansah, M. S. Schwenger, M. F. Haase, Soft matter 2019, 15, 3379.
[16] J. Li, H. Sun, M. Wang, Langmuir 2020, 36, 14644.
[17] A. J. Bray, Advances in Physics 2002, 51, 481.
[18] M. E. Cates, P. S. Clegg, Soft Matter 2008, 4, 2132.
[19] B. P. Binks, J. A. Rodrigues, W. J. Frith, Langmuir 2007, 23, 3626.
[20] L. Tran, M. F. Haase, Langmuir 2019, 35, 8584.
[21] M. F. Haase, N. Sharifi-Mood, D. Lee, K. J. Stebe, ACS nano 2016, 10, 6338.
[22] D. A. Huse, S. Leibler, Journal de Physique 1988, 49, 605.
[23] A. Koretsky, P. Kruglyakov, Izv. Sib. Otd. Akad. Nauk USSR 1971, 2, 139.
[24] B. P. Binks, T. S. Horozov, *Colloidal particles at liquid interfaces*, Cambridge University Press, 2006.
[25] A. Stocco, M. Nobili, Advances in colloid and interface science 2017, 247, 223.
[26] R. Aveyard, J. H. Clint, T. S. Horozov, Physical Chemistry Chemical Physics 2003, 5, 2398.
[27] C. A. Grattoni, R. A. Dawe, C. Y. Seah, J. D. Gray, Journal of Chemical and Engineering Data 1993, 38, 516.
[28] A. Skrzecz, D. G. Shaw, A. Maczynski, A. Skrzecz, Journal of Physical and Chemical Reference Data 1999, 28, 983.
[29] G. L. Amidon, S. H. Yalkowsky, S. Leung, Journal of Pharmaceutical Sciences 1974, 63, 1858.
[30] S. P. Kharal, M. F. Haase, Small 2022, 2106826.
[31] D. Chandler, Nature 2005, 437, 640.
[32] S. Boakye-Ansah, M. A. Khan, M. F. Haase, The Journal of Physical Chemistry C 2020, 124, 12417.
[33] M. Farrokhbin, B. Stojimirović, M. Galli, M. K. Aminian, Y. Hallez, G. Trefalt, Physical Chemistry Chemical Physics 2019, 21, 18866.
[34] K. Pratt, W. Wakeham, Proceedings of the Royal Society of London. A. Mathematical and Physical Sciences 1975, 342, 401.
[35] G. H. Shroff, L. Shemilt, Journal of Chemical and Engineering Data 1966, 11, 183.

Chapter 4

Alumina Bijels

Abstract: The miniaturization of reactors is a sustainable way to upgrade and upscale the capacity of chemical reactors for industrial applications. Self-assembled systems are attractive methods for the formation of batch and continuous reaction models. Bijels are particle-stabilized bicontinuous emulsion gels having a unique architecture of two intertwined liquid channels which provides high interfacial area and selective flow of fluids. The major limitations of bijel as an interfacial chemical reactor are complex fabrication methods and structural control. Recently we reported a continuous and scalable synthesis of submicron sized STrIPS bijels having an interfacial area of 2 m^2/cm^3 [1]. STrIPS submicron bijels are ideal mass transfer devices as they provide high surface area, scalable fabrication, and selective flow of fluids. In this chapter, we discuss the fabrication methods of catalytic alumina bijels and their structural dependencies. We focus on the physiochemical dependencies (pH, surfactant, salt) of the STrIPS process using alumina particles and compare it with other methods (alumina particle doping and interfacial alumina coating) of imparting alumina functionality to the bijel.

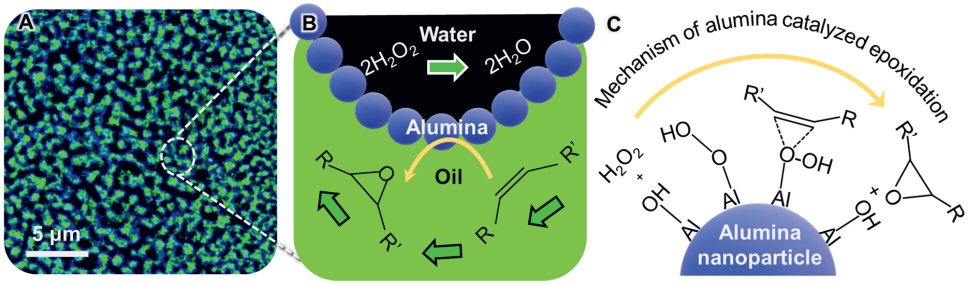

4.1 Introduction:

Bijel is a torturous interwoven network of immiscible liquid channels providing a large interfacial area for applications in the fields of energy storage[2], bijel-templated hydrogel for cell delivery[3], and membrane separation.[4, 5] The evolution of bijel preparation methods has equipped us with higher control over the fabrication processes to form micro to nanometer domain-sized bijel structures in a scalable manner. In our recently published work, we introduced unprecedented submicron sized bijel structures via the STrIPS method.[6] The full potential of the bijel having the intertwined liquid channels is leveraged through the active flow of liquids using electro-osmosis.[6] With this, we circumvent the limitations of diffusion-based interfacial reactions and product separation in the bijel system. These findings encourage us to realize the initial idea of using bijels as a microreactor.[7]

In this work, we employ the knowledge gained from the submicron-sized STrIPS bijel system and introduce catalytic properties to the bijel by using alumina functionalization. Alumina is chosen because it is inexpensive, active, and has the potential to act as a selective catalyst for the epoxidation reaction in the bijel.[8] Here, we aim to fabricate bijel using alumina particles and interfacial coating of alumina to explore the potential of alumina bijel as a catalytic microreactor system.[8] Epoxy resins and chemical compounds are used in many materials such as adhesives, plastics, paints, medical devices[9], and implants[10] with a global market of $8.7 billion worldwide.[11] The surging demand for epoxy compounds has facilitated the evolution of different synthesis methods aiming for high productivity, efficient scalability, and innocuous environmental impact. Among the various available methods, heterogeneous catalysis of alkenes in the presence of hydrogen peroxide (H_2O_2) is an attractive method for the production of epoxides in industrial settings.[12] In comparison to conventional methods, peroxide is a cleaner method that produces only water as a byproduct in conjugation with catalytic amounts of cheap and nontoxic metals.[13] Major shortcomings of the traditional methods are either related to catalytic efficiencies such as low utilization of H_2O_2[14], epoxide selectivity[15], or long reaction times upon scaling up reactions in batch reactors.[16]

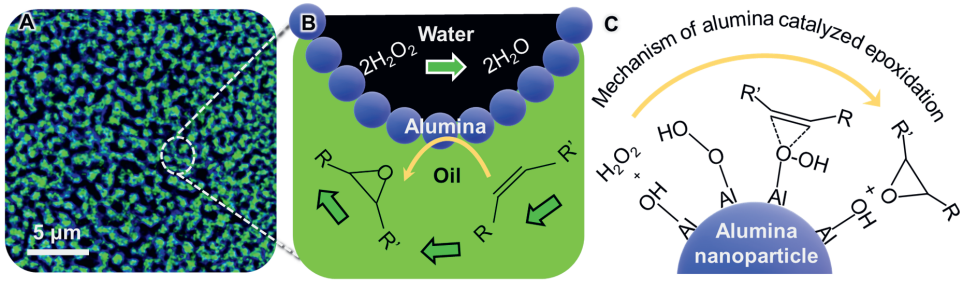

Fig. 4.1 Epoxidation of alkenes in alumina bijel. A) A confocal micrograph of a bijel showing water in black, oil in green and particles in blue. B) An illustration showing the interfacial epoxidation reaction

and flow of constituent reagents and products inside the liquid channels. C) Proposed reaction mechanism of the alumina-catalyzed epoxidation of alkenes.

In Fig. 4.1, we show bijel as a microreactor to continuously support the catalytic production of epoxides. Bijel liquid networks provide a high interfacial area system for the selective supply of reagents and removal of products in a continuous fashion. As a cheap and selective catalyst, alumina in conjugation with hydrogen peroxide provides an efficient catalytic system. To realize the interfacial epoxidation reaction we need to employ catalytic properties to the bijels. In this work, we discuss three strategies to make bijels catalytically active *i*. using alumina particles as the stabilizer, *ii.* alumina particle doping in silica bijel and *iii*. coating bijel with the alumina precursor.

As learned in the previous chapter there are two major driving forces to form submicron-sized bijel via STrIPS *i.* the rapid interfacial tension evolution and *ii.* in-situ particle modification to attain near-neutral wettability. To form bijel stabilized with alumina particles, we used the same ternary system of 1-propanol-DEP-water to leverage the fast interfacial tension evolution. Instead of silica, Ludox CL particles (diameter, ⌀ =12 nm) are used as stabilizing alumina particles. Ludox CL particles are core silica particles with alumina coating. At acidic pH (3-6) Ludox CL particles are positively charged and have different surface chemistry as compared to the silica nanoparticles. One major difference between silica and alumina particles is the colloidal stability near the isoelectric point. Modified silica particles, Ludox TMA have relatively higher colloidal stability in the highly acidic region than pure silica even as a concentrated dispersion of colloids. This can be explained by the modification with aluminum, the trivalent aluminum combines with the surface of the silica particle, replacing a tetravalent Si atom previously present in the lattice which forms the surface of the particle thus rendering a negative charge ($Al(OH)_4^-$) even at lower pH.[17] Whereas alumina particles like other metal-oxide particles are not stable near the isoelectric point and aggregate due to Van der Waal interactions.[18]

In this chapter, we discuss the physiochemical dependencies such as pH, surfactant, the weight fraction of nanoparticles, and salt concentration on alumina bijel formation using Ludox CL particles. We also study other methods to fabricate the alumina bijels such as doping of silica particles (Ludox TMA) with alumina particles and interfacial deposition of alumina. Further, we explore the characterization of alumina bijels using confocal and electron microscopy. Energy-dispersive X-ray spectroscopy (EDX) is used for the preliminary characterization of alumina deposition. Finally, aiming towards the main goal of the project using “bijels as microreactors” we tested the suitability of alumina bijels for the active flow of liquids using electroosmosis. Post-fabrication modifications are employed to facilitate the electroosmosis and future outlooks are discussed focusing on the catalytic alumina bijel fabrication and characterizations.

4.2 Results and Discussion

We first start with alumina bijel fabrication using alumina particles (Ludox CL) as stabilizers and later also discuss doping and interfacial coating as potential routes. As discussed in the previous chapter phase separation of a precursor mixture is a complex process involving multi-component dependencies. In the result section, we discuss the physiochemical variables of STrIPS process such as pH, salt and surfactants probing alumina particles. We will analyze these properties of alumina particles to discuss the possibilities and limitations of alumina particles as a bijel stabilizer. We used the same precursor mixture composition $\varphi_{DEP} = 0.07$, $\varphi_{1Prop} = 0.43$, $\varphi_{water} = 0.50$ as for the silica particle shown in Fig 4.2. Commercially available Ludox CL particles are 30 *wt* % aqueous dispersion of spherical (diameter 12 nm) particles having silica core and surface modified with alumina. These particles are positively charged in the acidic pH range. The small size results in high surface to volume ratio and at higher concentrations the dispersions gel significantly in comparison to Ludox TMA particles.

We use particles at pH 3.8 (positively charged) as supplied by the manufacturer. To tune the hydrophobicity of particles during STrIPS via in situ hydrophobization we add negatively charged surfactants. Sodium lauryl sulfate surfactants are used with varying alkyl chain lengths to analyze the effect of surfactants on the bijel structure. We also tested double chain surfactant dioctyl sodium sulfosuccinate (AOT) to screen the effect of a more hydrophobic surfactant.

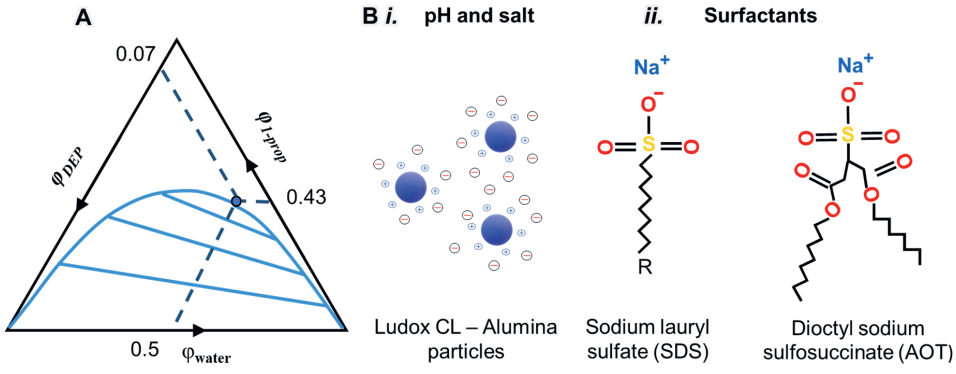

Fig 4.2 A) shows the ternary phase diagram of DEP-water-1-propanol and the blue dot shows the selected composition for the precursor mixture preparation. B) *i.* effect of pH and salt on colloidal stability (illustration not drawn to scale) *ii.* Surfactant type and concentration variation for in-situ modification of hydrophobicity.

In combination with these, we varied the pH of the Ludox CL particles and tested structural dependence with varying concentrations of sodium dodecyl sulfate. Zeta potential measurements indicated that particles are positively charged for a broad range of pH (3 - 6.8). Varying the pH range of particles is studied to analyze the colloidal stability in aqueous dispersion as well as in the precursor mixture.

Previous studies with Ludox TMA particles reveal that the zeta potential of the particles making the optimal bijel structure is around ~ -15 to -20 mV. Therefore the pH range near the isoelectric point having positive zeta potential in the same range is investigated for Ludox CL particles to reproduce the submicron sized structure of STrIPS bijel. Fig 4.2B shows the three main variables *i.* surfactant, *ii*. salt, and *iii*. pH of the particles studied for tuning the hydrophobicity of the particles. Further, we also varied the weight fraction of the particles to screen the structural dependence.

4.2.1 Surfactant variation

4.2.1.1 **dioctyl sodium sulfosuccinate (AOT)**

We use the alumina particles (Ludox CL) from Sigma Aldrich UK without any further treatment for these experiments. It's an aqueous dispersion of 30 *wt* % alumina functionalized silica particle of pH 3.8. At such a high weight fraction 12 nm diameter particles gel significantly and form a viscous aqueous dispersion. A series of precursor mixtures are prepared with 20 *wt* % particles and varying concentrations of dioctyl sodium sulfosuccinate (AOT). Fig 4. 3 shows that all the tested concentrations of AOT in the precursor mixture phase separate and particles aggregate at the bottom phase. The turbidity of the bottom phase increases to an extent that we see the white aggregates of particles formed at the higher (80 and 90 mM) AOT concentration.

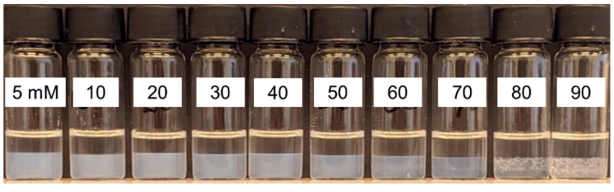

Fig. 4.3 A series of precursor mixtures made with varying concentrations of AOT in mM

4.2.1.2 **Sodium lauryl sulphate**

These results indicate that double-chain anionic surfactant fails to stabilize the precursor mixture resulting in phase separation. The exact mechanism of particle-induced phase-separation is elusive and requires further investigation. To our understanding particles being highly charged might become too hydrophobic with the double-chain surfactant and cause phase separation. Next, we test less hydrophobic single alkyl chain sodium lauryl sulfate surfactants. To start we used sodium dodecyl sulfate (SDS) a 12-carbon chain long surfactant. Again a series of SDS concentrations are tested for

precursor mixture stability. Fig 4.4 shows the prepared precursor mixtures, below 30 mM SDS precursor mixture phase separates (shown in yellow dashed lines), and above 50 mM precursor mixture becomes considerably turbid (red dashed line). Precursor mixtures remain stable and clear from 30 to 50 mM SDS. Further, we tested different concentrations (30, 31.5, 33.75, 35, 40 mM) of SDS in the stable regime.

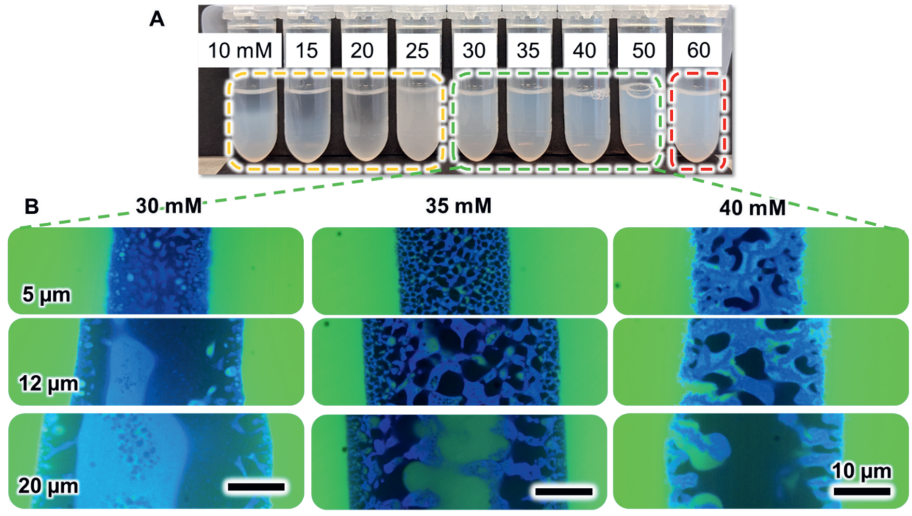

Fig. 4.4 A) Precursor mixtures with varying concentrations of sodium dodecyl sulfate (SDS). **B)** Confocal micrographs of alumina bijel with varying concentrations of SDS in the mixed regime.

Confocal micrographs in Fig 4. 4B show the structure of the bijel as a function of SDS concentration. In this study, we have labeled oil, water, and particles in green, black, and blue respectively. Around 30 mM concentration of SDS anisotropic shape droplets of oil are formed in water. Confocal analysis shows that particles partition in both to the oil and water phase. Around 35 mM SDS bicontinuous structures are recognized with domain sizes of 2-10 micrometers dimensions. A visible gradient of domain size is observed from the surface to the center of the fiber forming a hierarchical structure. This gradient suggests that the coarsening of domains happens for an extended period of time in contrast to the 1-propanol Ludox TMA precursor mixture. Higher concentrations of SDS (40 mM) show a clear partitioning of the particles in the oil phase. Interestingly particles are aggregated within the oil channels and dewet the water completely to form a shell-like structure (Fig 4.4B right column). Concentrations above 50 mM show visible aggregation (red dotted line) of particles in the precursor mixture and do not form stable structures. Analyzing the particle partitioning from the confocal micrograph indicates that the most uniform bicontinuous structures show a gelled network of particles in the oil phase.

The particle wettability is discussed later in this section. From this first set of experiments, we concluded that hierarchical porous structures can be formed using alumina particles with SDS surfactant using DEP-water-1-propanol ternary system. Preferable partitioning of the particles in the oil phase for all the tested concentrations suggests that they do not attain amphiphilic hydrophobicity during STrIPS to stabilize the submicron sized structures.

Obtained alumina bijels structures are quite comparable to the 2-propanol bijels. Where slow partitioning of 2-propanol in toluene during STrIPS fails to render amphiphilic hydrophobicity via in situ particle modification, resulting in extended coarsening and hollow shell-like structures.[6]

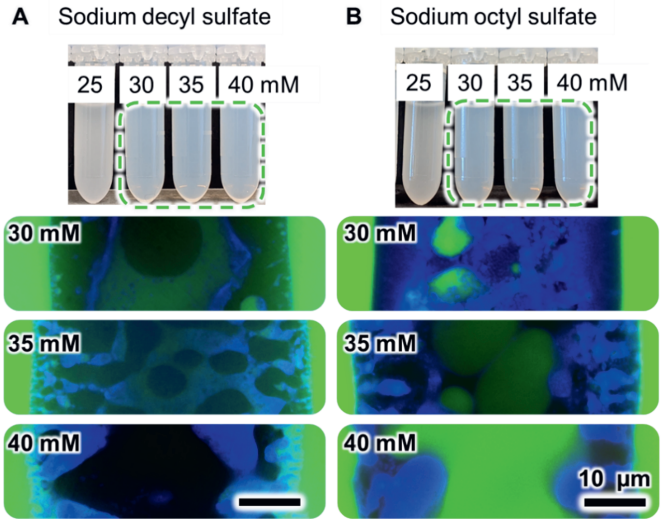

Fig. 4.5 Precursor mixture stability and corresponding bijel structures for sodium decyl sulfate **(A)** and sodium octyl sulfate **(B).**

For alumina bijel fabrication precursor composition and extrusion, conditions are the same as the submicron sized bijel system so that solvent transfer-mediated interfacial tension evolution remains unaffected. Another pivotal variable is the in-situ modification of particles. In the case of Ludox TMA particle in 1-propanol ternary system, we have learned that the initial charge density of the particles and the surfactant concentration majorly control the in situ particle modification during the STrIPS process.

Confocal micrographs indicate that particles are too hydrophobic for the tested concentrations of SDS. To further tune the hydrophobicity of the particles we tested sodium lauryl surfactants with shorter alkyl chains. Fig. 4.5 shows the precursor mixtures formed with different concentrations of 10 carbon chain long sodium decyl sulfate and 8 carbon chain long sodium octyl sulfate. We observed a similar trend in terms of the precursor mixture stability and bijel structure upon varying the surfactant concentrations.

Particles preferably partition in the oil phase for all the tested concentrations of the octyl and decyl sulfate surfactants. Although the formed domains seem to coarsen more for the shorter chain surfactants.

Quantitative assessment of the nanoparticle surface activity during the STrIPS is probed through their interfacial attachment efficiency (η). The attachment efficiency of the particles is defined as the percentage of the particles attached to the interface to the particles disperse in the precursor mixture. For calculating the attachment efficiency we require interfacial area which is determined by using confocal images analysis in image J. Image processing method using image J has been discussed in the previous chapter (Appendix 3.5.9) in detail. Image processing was done carefully to discern the interface between oil and water and locate the particles. Next, we measure the interfacial area of different surfactants with varying concentrations ($c_{surfactants}$) and calculate the attachment efficiency (η).

The attachment efficiency is found to be highest around 14 ± 2.5% for the sodium dodecyl and lowest 3.5 ± 0.3% octyl sulfate. This suggests that sodium dodecyl sulfate facilitates the stability of particles and required surface chemistry during the STrIPS to arrest the coarsening. The lines in the graphs are to guide the eyes.

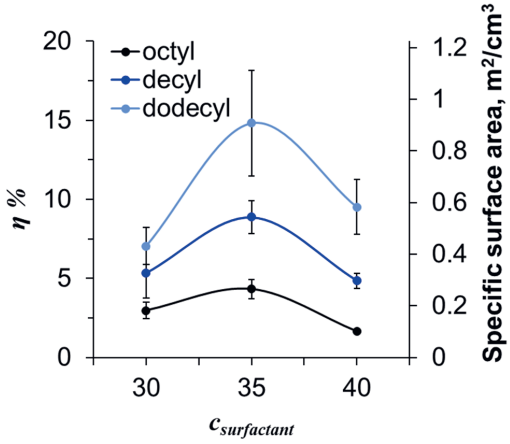

Fig. 4.6 Different surfactants are color coded in light blue (sodium dodecyl sulfate), dark blue (sodium decyl sulphate), and black (octyl sulfate). The attachment efficiency and specific surface area of different surfactants are shown as a function of the concentrations.

The confocal images obtained upon surfactant type and concentration variations refer that particles remain in the oil phase for all the tested conditions. To this end, we hypothesize that the Ludox CL particles remain hydrophobic during STrIPS and prefer to be in the oil phase. The surface modification of the particles during STrIPS via surfactant adsorption is a dynamic process and depends on the solvent fraction at a given point of time during phase separation.[5, 19] The amount of surfactant adsorbed onto the particles determines the partitioning of the particles either in water or oil-rich phases. We start with hydrophilic particles and add a surfactant in the precursor mixture to tune the particle hydrophobicity during STrIPS.

The extent of surfactant adsorption determines the three-phase contact angle θ of the particle at the oil-water interface. For $\theta < 90^{o}$ particles remain hydrophilic and prefer partitioning in the water-rich phase whereas $\theta > 90^{o}$ renders particles hydrophobic to move to the oil-rich phase. Only near 90^{o} contact angle of the particle allows bicontinuous structure formation due to nonpreferential curvature of the interface.[20] To test the particle partitioning during STrIPS emulsion inversion experiments are performed. As shown in Fig 4.7A different compositions are selected at the mid-point composition of the tie lines labeled as 1, 2, 3 and 4. Each composition has a different solvent fraction in the water rich phase ($\varphi"_{1prop}$). All these compositions have a range of SDS concentrations with 20 *wt* % ludox CL particles. All the samples were mixed vigorously to facilitate the emulsification and a fluorescent dye Nile red is added to the toluene (oil) to allow the labeling of the emulsions.

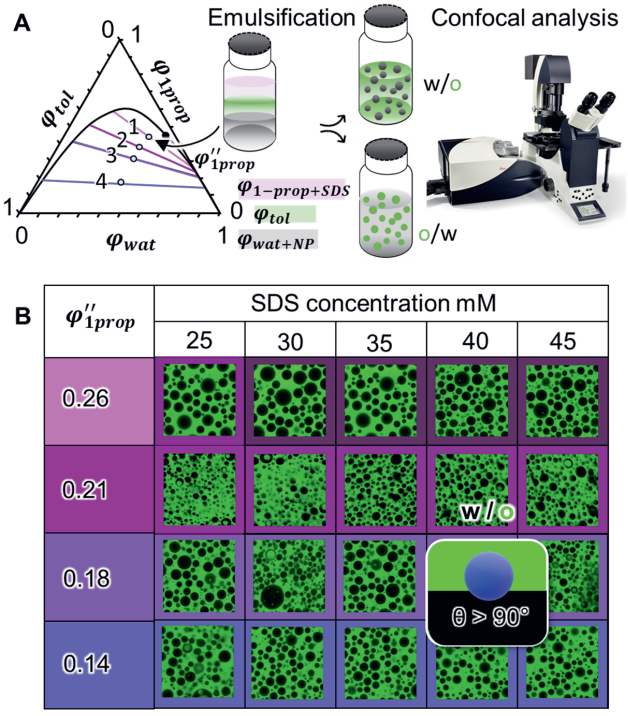

Fig. 4.7 Emulsion inversion during STrIPS. (A) Schematic depiction of Ternary phase diagram for toluene/1-propanol/water. Particle-stabilized emulsions are prepared for a midpoint of the tie-line shown as 1, 2, 3, and 4 compositions using different SDS concentrations. (B) Confocal micrographs of the emulsion formed for each composition upon SDS variation from 13 to 30 mM. The oil phase of toluene is fluorescently labeled with Nile red and shown as green in the images.

In Fig 4.7B the table shows the confocal images of the emulsions prepared at different compositions with varying concentrations of SDS. As shown in the images all tested samples show water in oil (w/o)

emulsions. These results suggest that the particles remain hydrophobic for all the tested compositions and SDS concentrations. The hydrophobicity of Ludox CL particles during STrIPS can be explained by the high charge leading to excessive surfactant adsorption in the acidic pH range (discussed in the next section). Emulsion inversion experiments suggest that the particles become hydrophobic at an early stage of phase separation (high φ_{1prop}). We can also relate these results with the confocal micrographs of SDS variation (Fig 4.5B) which shows that even at the lowest tested concentration particles are mostly in the oil phase. As the concentration of the SDS increases particles start to preferentially partition in the oil phase and form a gelled network in the oil domains.

4.2.2 pH and salt variation of Ludox CL

In the previous section, we tested different surfactants toward alumina bijel structure at a given pH of 3.8. Results show that surfactant variation has limited control over the formed structures as the particles are charged at acidic pH of 3.8. To further tune the surface charge of the particles we tested pH variation on bijel structures. Ludox CL particles are 30 *wt* % aqueous dispersion of alumina coated silica nanoparticles.

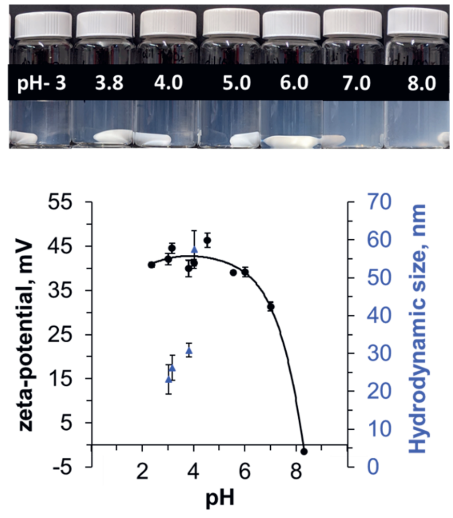

Fig 4.8 Zeta-potential vs pH curve, in the top image pictures of diluted Ludox CL particles with varying pH. The bottom graph shows the zeta potential measurements vs pH variation.

The measured pH of the particles received from the supplier was 3.8. Ludox CL sols have a high weight fraction and small (12 nm diameter) particle size that tends to gel significantly and make a viscous aqueous dispersion. The size and concentration of particles are interrelated for the gelling effect, gelling rate is proportional to the total surface area of particles in a given volume of sol.[21] A short probe

sonication helps with the redispersion. The pH of diluted particle dispersions is varied from 3 to 8. As shown in Fig 4.8A, diluted samples with increasing pH also show some turbidity. Zeta-potential measurements showed that Ludox CL particles have a zeta-potential of ~ 40 mV for a wide range of acidic pH which decreases drastically near the isoelectric point around ~ pH 8.3 The measured zeta potentials and isoelectric point of Ludox CL agree with the previous reports.[22]

Further comparing the aqueous colloidal stability of silica and alumina particles as a function of pH, silica particles remain relatively stable even near the isoelectric point.[21] This property is further assisted in Ludox TMA particles by aluminum functionalization to impart stability in the acidic pH range [17]. We have learned that Ludox TMA particles are quite stable in precursor mixture for a wide range of physiochemical parameters. To analyze the stability of Ludox CL particles in the precursor mixture at different pH, we adjusted the pH using 1 M HCl and 1 M NaOH. It is observed that particles at 30 *wt* % concentration do not disperse above pH 4.6 and below pH 2.5 even after vigorous mixing and sonication (Appendix Fig 4.15).

The colloidal stability of particles in the precursor mixture can be significantly different than the aqueous dispersion. To further validate, samples with varying SDS concentrations are made at different pH values. Fig 4.9 shows precursor mixtures at pH 3 and below phase separates and show aggregation above pH 5. Consequently, only a narrow range of pH from 3.5 to 4.5 allows the mixing of precursor mixture with varying concentrations of SDS. Fig 4. 9 shows the most uniform confocal micrographs of bijels formed upon SDS concentration variation for pH 3.8 and 4.5. There are no major structural differences as also expected from the zeta potential measurements in this pH range. Notably, at pH 3.8 the domain size gradient is the smallest for the tested pH range small.

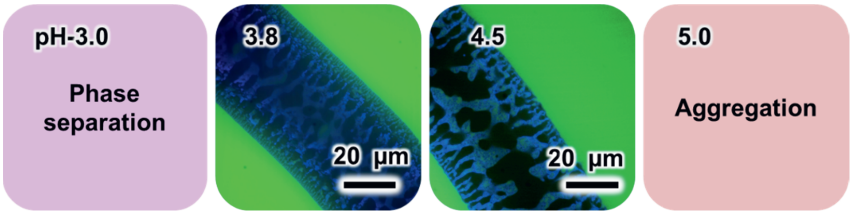

Fig 4.9 Ludox CL colloidal stability in precursor mixture and bijel structure.

Ideally, we use stable dispersion of particles to make precursor mixtures but that narrows the screening pH range of Ludox CL particles. To further extend the pH-dependent colloidal stability screening we prepare precursor mixtures with aggregated particles. We use mechanical agitation to mix the aggregated particles upon the addition of an increasing volume of 1 M NaOH. Through this method, we want to test the colloidal stability for a wide range of pH in the precursor mixture. Particle sample preparation is described in Appendix 4.16. We prepare a precursor mixture with varying SDS

concentrations for each set of particles, all but sample 1 showed aggregation/phase separation. Sample-1 particles are measured to be around pH 4.6 and comply with the earlier results of pH variation.

To summarize the pH variation, we found that Ludox CL particle gel significantly at high concentrations and as we increase the pH tends to aggregate. Further, the stability in the precursor mixture also follows the same trend and the mixture remains stable only in the pH range of 3- 4.5. These limitations with the pH variation restrict the possibilities of surface charge modulation during STrIPS. It is well recognized that higher charge density is attained in the presence of electrolytes at a given pH.[23] In these experiments, we rule out the effect of electrolytes on colloidal stability in the precursor mixture. Positively charged Ludox CL particles are stabilized with chloride counter ions and to vary the electrolyte concentration we dialyzed particles at pH 3.8 with varying concentrations of NaCl. The colloidal stability of the particles is tested by making the precursor mixtures with varying concentrations of SDS at each NaCl concentration (Appendix 4.17).

We observed only at low concentrations of salt precursor mixture remain stable. These experiments are important in furthering our understanding of the surface charge and electrolyte interplay toward colloidal stability in the precursor mixture. Based on these results, we can hypothesize that for concentrated sols like Ludox CL with small (12 nm) particle size we need a relatively high proportion of chloride counterions to Aluminium to charge the surface. The concentration of chloride ions can be so high that it reaches its critical coagulation concentration at the existing pH. This could be the reason for particle aggregation even upon adding a small amount of salt.

4.2.3 Nanoparticle weight fraction

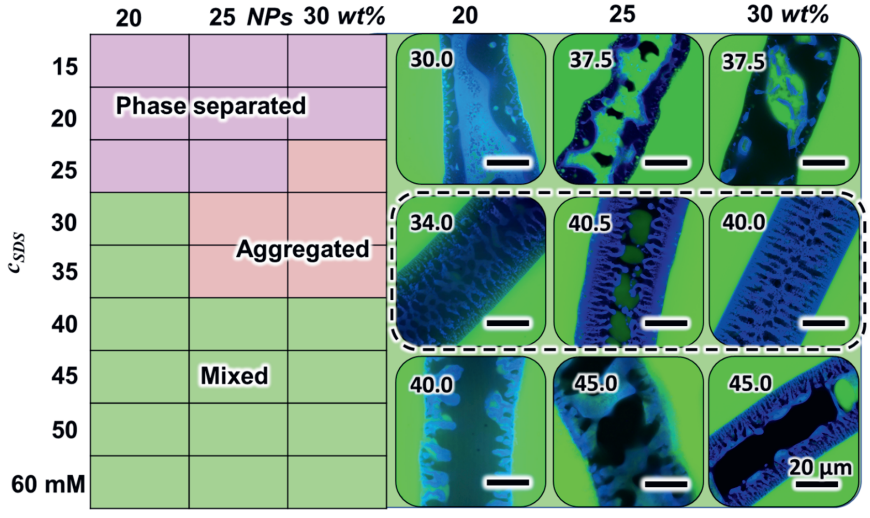

Fig 4.10 Ludox CL weight fraction variation with SDS variation to analyze the effect on the bijel structure.

The other variable which controls the domain size and surface pore size of the bijel is the nanoparticle weight fraction in the precursor mixture[4],[5]. We varied the nanoparticle weight fraction 20, 25 and 30 *wt* % of the water phase in the precursor mixture. Colloidal stability in the precursor mixture and formed bijel structures are displayed in Fig 4.10. The black dotted line highlights the most uniform bijel structures for all three tested particle fractions. Increasing particle *wt* % does not show a significant change in the bijel domain size though excess particle aggregation is seen in the oil phase.

4.2.4 Doping of Ludox CL particles in precursor mixture with silica particles

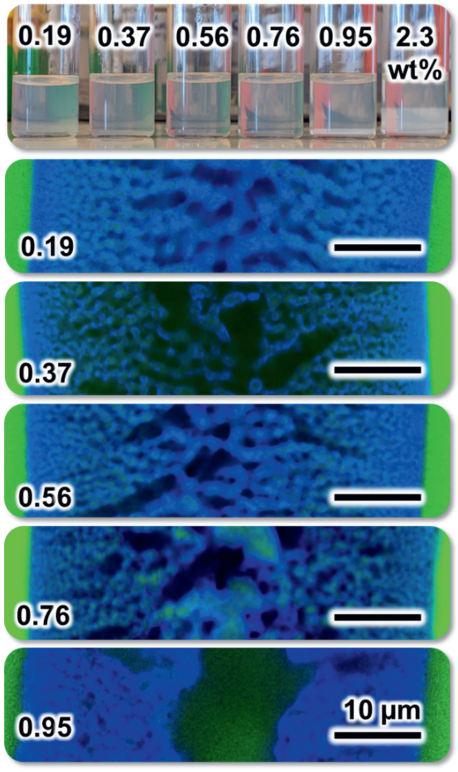

Fig 4.11 Colloidal stability in the precursor mixture with varying *wt* % of alumina to the total nanoparticle and the corresponding bijel confocal micrographs.

We also explored other methods to make catalytic alumina bijels such as the addition of a small fraction of Ludox CL particles as a dopant in the silica precursor mix. In recent years, researchers have shown an increased interest in heteroaggregation as a method of controlled self-assembly to form application-specific composite.[22, 24-26] Especially in the field of catalysis, molecular or particular (multimodal particle population) doping has emerged as an instrumental tool to enhance the properties of a catalyst.[27-29] The following experiments are an attempt to develop some understanding of alumina particle doping in oppositely charged silica precursor mixture to make catalytic bijels. The details of sample preparation are provided in the appendix. We specifically investigated the colloidal stability in the precursor mixture and corresponding structures for varying *wt* % of doping precursor mixture. Fig 4.11 (top image) shows the stability of the precursor mixture with varying *wt %* of particles. Precursor mixture remains stable up to 1 *wt %* of Ludox CL particles and above that evident aggregation of particles is observed due to strong electrostatic interaction.

It's important to keep in mind that Ludox CL particles are significantly charged at pH 3.8 which can cause strong aggregation upon increasing concentrations. The corresponding structures show that structure retains bicontinuity and submicron size of oil domains until 0.6 *wt %* along with some radial channels. As we increase the *wt %* the occurrence of the radial channels increases and above 0.8 *wt %* a central oil cavity is formed. Interestingly the surface of bijel fiber still has relatively small domains in comparison to the bijels made only with Ludox CL particles. It suggests that the particles gain desired surface chemistry to arrest the phase separation at least during the start of demixing and later on due to increased aggregation larger domains and a central cavity forms. To validate the obtained results, we need to further characterize alumina functionalization with spectroscopy techniques and perform comparative analysis for catalytic conversions.

4.2.5 Alumina coating in the submicron-size bijel

One of the popular methods of preparing functional porous materials is interfacial coating and polymerization.[30] It is usually a chemical reaction to deposit material at a liquid-liquid or liquid-air interface to form capsules, crosslinked emulsions, and membranes. We took advantage of the bicontinuous morphology of the bijel to introduce the alumina onto the silica template. There have been multiple studies showcasing the applications of alumina functionalized silica in Pickering emulsions and catalysis.[31],[32] Generally, alumina deposition is performed via chemical vapor deposition (CVD) and high temperature assisted condensation of alumina.[33] There are also other methods using aluminum butoxide precursor in a modified sol-gel reaction.[34] For the bijel system, we can't afford high temperature assisted reactions hence we tested a modified reaction at room temperature followed by 50 ºC incubation for 120 minutes. Methods of sample preparation and steps can be found in the appendix.

A series of reaction containers are prepared to have the same number of bijel fibers and are treated with 3 *wt* % TEOS for 24 hours. As shown in appendix 4.5.4 a varying concentration of aluminum butoxide is added to the ambient phase of mineral oil and mixed well. The highest two concentrations 5 and 1 *wt* % showed visible white precipitate formation after 15 mins of reaction which increased significantly during the heating process. The rest of the samples remain clear during the reaction. We washed all the samples thoroughly and dried them to be analyzed under the scanning electron microscope (SEM). Fig 4.12A shows the corresponding micrographs, all the fibers seem to have typical porous bijel structures upon drying and do not show any damage or structural deformation. Although higher concentrations of aluminum butoxide showed precipitate formation on the bijel fibers the surface remains porous and internal channels are open (see cross-sections). Furthermore, to analyze the bijel surface morphology we calculated the average pore size and surface pore density (pores per unit area) as a function of aluminum butoxide concentration.

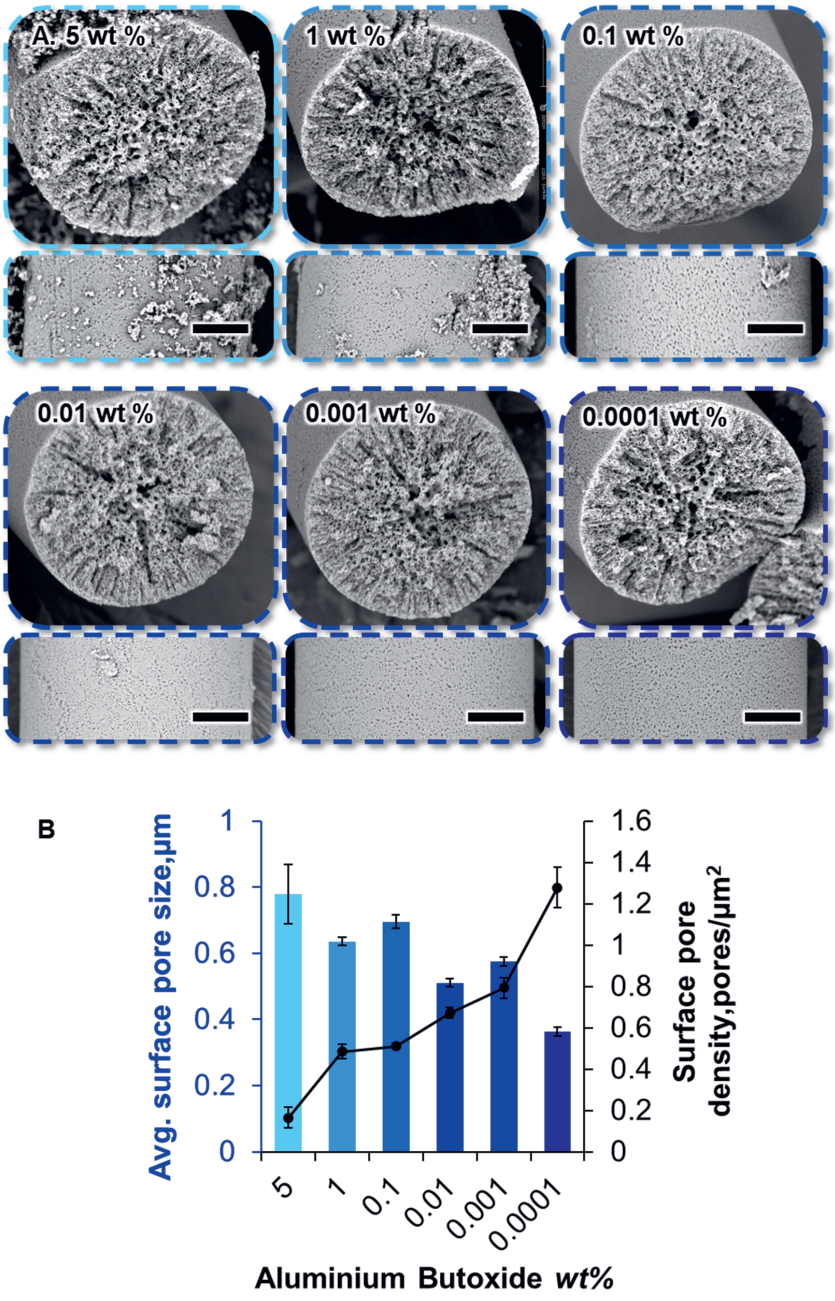

Fig. 4.12 Interfacial coating of alumina using aluminum butoxide as a precursor. A) shows the scanning electron micrographs of bijel treated with varying concentrations of aluminum butoxide. B) Graph describes the surface porosity by average pore size and pore density analysis as a function of aluminum butoxide concentration.

Fig 4.12B shows that average pore size increases with aluminum butoxide concentration whereas the surface pore density decreases. This is because the deposition of alumina on the surface blocks the small pores which results in the lower pore density whereas the average size of the pore is skewed towards the higher end. It's important to note that the percentage porosity of these fibers shows that the fiber surface remains porous even at the higher end of coating concentrations (Appendix) to allow the flow of liquids.

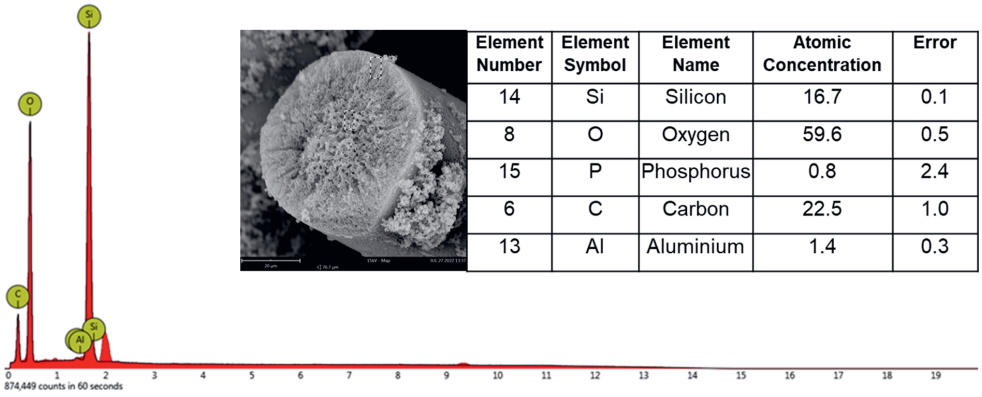

Element Number	Element Symbol	Element Name	Atomic Concentration	Error
14	Si	Silicon	16.7	0.1
8	O	Oxygen	59.6	0.5
15	P	Phosphorus	0.8	2.4
6	C	Carbon	22.5	1.0
13	Al	Aluminium	1.4	0.3

Fig 4.13 EDX spectra of 5 *wt* % Aluminum butoxide coating

Further to confirm the chemical deposition of alumina we performed Energy Dispersive X-rays Spectroscopy (EDX or EDS) which is an analytical technique where element specific radiation is used for chemical characterization of the surface near volume. EDX results confirm the presence of aluminum, especially at the higher concentrations of tested aluminum butoxide coatings. For the lower concentrations, we did not get signals strong enough to make a conclusive remark about the coating efficiency. In appendix 4.5.4, we show the EDX spectra of surface precipitates having a considerably high fraction of aluminum which confirms the reaction. The EDX analysis is performed at the center of the fiber considering the diffusion based limitations of precursor aluminum butoxide. We confirm the presence of aluminum upon coating with aluminum butoxide in comparison to noncoated bijel fibers.

The major challenges ahead for the interfacial deposition of alumina are optimization of the coating method and better characterization. To achieve higher sensitivity, chemical, and spatial characterization of the alumina deposition we can use HR-SEM EDX and Raman spectroscopy. The catalytic activity of epoxidation can also be used as a comparative method for the different coating methods and conditions.

4.2.6 Post-processing and electro-osmosis in Alumina bijel

In order to check the catalytic activity of the alumina functionalized fibers we need to flow liquids into the channels with reactants and products. This can be done via diffusion[35] and more rapidly with electroosmosis[1]. Electroosmosis in the bijel requires water reservoirs to be added at the cut ends of the fibers to connect the internal channels across the length of the fibers. This step is crucial as we have been taking advantage of the hydrophobic nature of the silica bijels to add the water reservoirs at the ends. The chemical nature of bijel fibers made with Ludox CL is hydrophilic as we add the water drop at the end of the fibers it spreads over the fiber. To carry out electroosmosis we treated the fibers with n-hexyltriethoxysilane (0.01 and 0.1 *wt* %) to make them hydrophobic. In the figure below we show the treatment renders the fiber hydrophobic and allows electroosmosis.

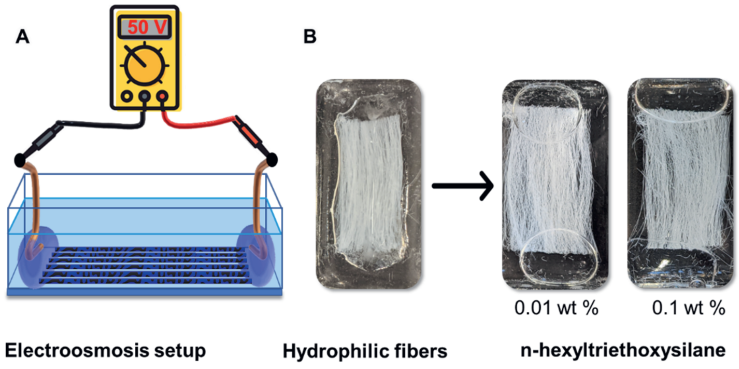

Fig 4.14 A) Schematic depiction of electroosmosis setup with electrodes submerged in the water reservoirs and a voltage is applied. B) Shows the images of fibers before and after treatment of the n-hexyltriethoxysilane.

With these preliminary experiments, we learned that alumina bijels made with Ludox CL particles can be surface modified to allow the electro-osmosis flow to be tested. For the future outlook, we need quantitative studies to define and validate the electroosmotic flow in the catalytic alumina bijels made via Ludox CL particles or alumina-coating on silica bijel fibers. The understanding gained from these experiments will allow us to perform interfacial catalysis in a controlled and optimized manner.

4.3 Conclusion

This study set out to explore the possibility of employing functional particles in the STrIPS bijels. In the first half of this work, we discuss bijels stabilized with Ludox CL particles formed via STrIPS. For the first time, we report that alumina particles (Ludox CL) can be used as stabilizers to form bijels. The findings suggest that the high charge density of Ludox CL particle limits the control over the bijel

structure. Parameter studies of different dependencies such as surfactants type and concentration, pH, salt, and weight fraction of nanoparticles confirm that limitations of bijel domain size control.

Next, we also explored other means of alumina functionalization like doping of silica bijels with alumina particles and interfacial coating of alumina in silica bijel. Ludox CL doping in silica precursor mixture showed that particles up to 1 *wt* % form a stable precursor mixture and generate bicontinuous structures. Scanning electron micrographs show that interfacial coating using aluminium butoxide precursor does not affect the submicron sized bijel structure. Characterization of alumina functionality was done by EDX which confirms the presence of aluminum. A major limitation of the current study is the characterization of alumina and the major outlook of this project. Further investigation and experimentation are required to understand the implications of alumina functionalization of bijel towards the catalysis of alkene to form epoxides.

4.4 Materials and methods

Chemicals: All solvents used in the experimental study are HPLC grade. Silica nanoparticles (Ludox TMA), Alumina nanoparticles (Ludox CL), aluminum tri-sec-butoxide, (97%), Hexadecyl-trimethylammonium bromide (C_{16}TAB, >99%), 1-propanol (>99.5%), 2-propanol (>99.5%), Nile red, Tetraethyl orthosilicate (TEOS, >99%), Sodium hydroxide (≥99%), Sodium lauryl sulfate (≥99%), Dioctyl sodium sulfosuccinate (≥99%) and mineral oil are purchased from Sigma-Aldrich UK. Diethyl phthalate (DEP, 99%), Toluene (99.85%), n-Hexane (99% HPLC), Glycerol (>99%), hydrochloric acid (HCl, 37% pure) were received from Acros organics. Ethanol and Triethylamine (TEA, >99.5%) are purchased from VWR international Ltd.

pH measurements:`pH measurements were carried out using the Toledo pH electrode In Lab Routine Pro-ISM. Three point calibration was used for the desired range of analysis.

Zeta-potential measurements: 10 ml dispersion of diluted aqueous Ludox CL particles (0.1 *wt*%) solid was prepared to measure the zeta potential microelectrophoresis with a zeta sizer (Zetasizer Ultra, ZSU5700, Malvern Pananalytical). All samples were mixed well by vortex and sonicated for 15 mins before the analysis. The zeta potential was determined as a function pH at 25 °C in triplicates.

Confocal analysis: Confocal analysis was used to visualize the fluorescently tagged bicontinuous immiscible phases. Nile red was added to hexane which shows solvatochromism property. Upon shining the 488 laser emits green emission spectra (500-550 nm) for hexane and red (600-700 nm) for the particles. Please refer to the appendix of the previous chapter for the spectral graph and further details. To differentiate the particles in this chapter we have used different false colors blue for the particles,

Scanning electron microscopy analysis: A Phenom Pro Scanning Electron Microscope has been employed for imaging the dried bijel fibers. Dry samples are sputter-coated with platinum (8-10 nm) before imaging. An accelerating voltage of 10 kV was used for the image acquisition. Energy dispersion x-ray spectroscopy analysis was done using the same microscope with element detection suite to quantify the aluminum for the coating experiments.

4.5 Appendix

4.5.1 pH variation for 30 *wt* % Ludox CL

We used 1M HCl and 1 M NaOH to change the pH of the 10 ml aqueous dispersion of particles from a starting pH of 3.8.

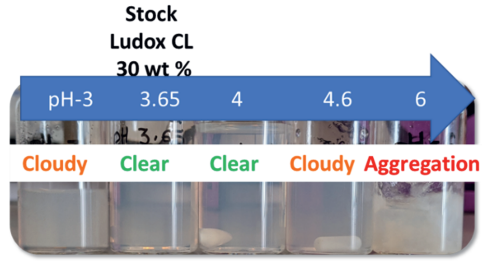

Fig 4.15 Colloidal dispersion of 30 *wt* % Ludox CL particles at various pH

4.5.2 pH variation by direct addition of base

For changing the pH of the particles, 1 M NaOH is used and different volumes are added to 15 ml Ludox CL dispersion (30 *wt* %, pH 3.8) to make six samples (S1-S6). As the pH increases particles gel and aggregate to make a thick paste that can't be mixed with vortex or sonication. Mechanical agitation is done to allow the mixing of particles via a spatula.

C_{SDS}, *mM* → / *NaOH, mL* ↓	10	15	20	25	30	35	40
0.2	Phase separated			Mixed			
0.5							
1.0							
2.0							
3.0			Aggregated				
5.0							

Fig 4.16 The table shows the colloidal stability of Ludox CL in the precursor mixture as a function of NaOH volume added and SDS concentration.

Precursor mixtures are made with a constant weight fraction of the particles with varying concentrations of SDS.

4.5.3 Salt variation

To vary the concentration of electrolytes in the aqueous dispersion of Ludox CL, dialysis is performed. We follow the same dialysis procedure as discussed in the previous chapter. We use 20 ml of Ludox CL particles at pH 3.8 and put them in a 12 kD MWCO dialysis membrane and sealed the ends with dialysis clips. These constructs are put in a 2-liter beaker of water at pH 3.8 and varying concentrations of NaCl. The dialysis was carried out for 24 hours. Further, each sample was used to make a precursor mixture with varying concentrations of SDS.

Fig 4.17 The table shows the colloidal stability of Ludox CL in the precursor mixture as a function of salt and SDS concentration.

4.5.4 Aluminium butoxide coating

Several containers with the same number of bijel fibers are prepared and treated with 3 *wt* % TEOS for 24 hours. Next, all the samples are washed with mineral oil to remove the excess TEOS and stored in mineral oil. Aluminium butoxide stock solution (5 *wt* %) is prepared in mineral oil and added to the containers as per the desired final concentration in 3 ml of total volume. Now the reaction is carried out at 50 ºC for 2 hours under the fume hood. After the reaction, all samples were washed with hexane and dried under the hood before the SEM and EDX analysis. The platinum coating was done for all the samples and in the EDX mass fraction graphs, the Pt peak is misidentified as Zr.

A

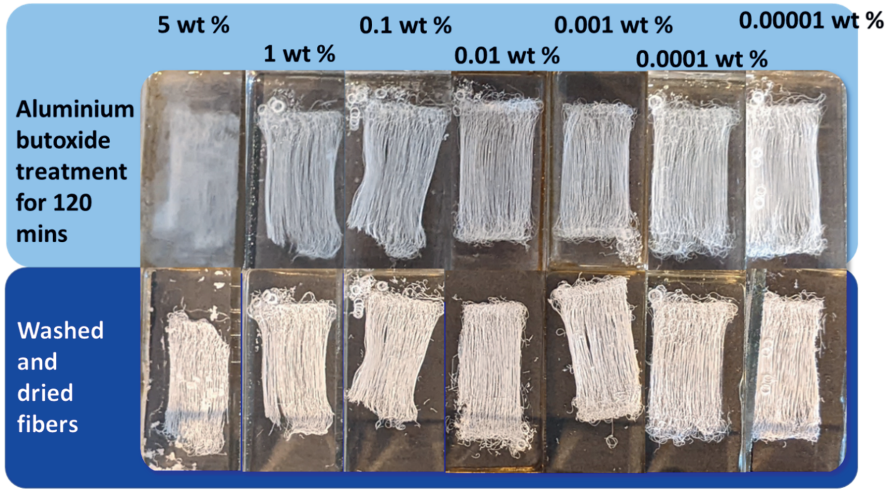

B

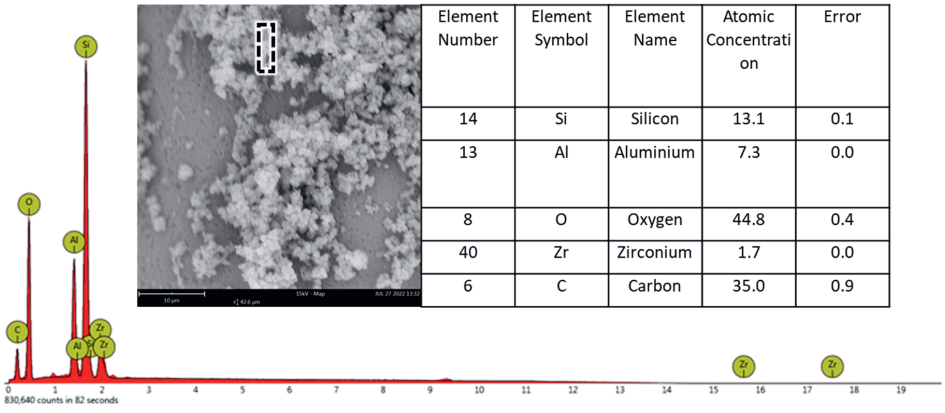

Element Number	Element Symbol	Element Name	Atomic Concentration	Error
14	Si	Silicon	13.1	0.1
13	Al	Aluminium	7.3	0.0
8	O	Oxygen	44.8	0.4
40	Zr	Zirconium	1.7	0.0
6	C	Carbon	35.0	0.9

Fig 4. 18 A) shows the images of the treated bijel containers with varying concentrations of aluminum butoxide and the dried fibers after the washing. B) EDX analysis of the surface precipitates at 1 *wt* % of aluminum butoxide.

4.6 Bibliography

[1] M. A. Khan, A. J. Sprockel, K. A. Macmillan, M. T. Alting, S. P. Kharal, S. Boakye-Ansah, M. F. Haase, Advanced Materials 2022, 34, 2109547.
[2] J. A. Witt, D. R. Mumm, A. Mohraz, Journal of Materials Chemistry A 2016, 4, 1000.
[3] T. J. Thorson, E. L. Botvinick, A. Mohraz, ACS Biomaterials Science & Engineering 2018, 4, 587.
[4] M. F. Haase, H. Jeon, N. Hough, J. H. Kim, K. J. Stebe, D. Lee, Nature Communications 2017, 8, 1234.
[5] H. Siegel, A. J. Sprockel, M. S. Schwenger, J. M. Steenhoff, I. Achterhuis, W. M. de Vos, M. F. Haase, ACS Applied Materials & Interfaces 2022, 14, 43195.
[6] M. A. Khan, A. J. Sprockel, K. A. Macmillan, M. T. Alting, S. P. Kharal, S. Boakye-Ansah, M. F. Haase, Advanced Materials, n/a, 2109547.
[7] E. M. Herzig, K. A. White, A. B. Schofield, W. C. K. Poon, P. S. Clegg, Nature Materials 2007, 6, 966.
[8] M. C. A. van Vliet, D. Mandelli, I. W. C. E. Arends, U. Schuchardt, R. A. Sheldon, Green Chemistry 2001, 3, 243.
[9] B. Qi, Q. X. Zhang, M. Bannister, Y. W. Mai, Composite Structures 2006, 75, 514.
[10] F. G. Garcia, M. Elena Leyva, A. A. Alencar de Queiroz, O. Zazuco Higa, Journal of Applied Polymer Science 2009, 112, 1215.
[11] R. Auvergne, S. Caillol, G. David, B. Boutevin, J.-P. Pascault, Chemical Reviews 2014, 114, 1082.
[12] V. Russo, R. Tesser, E. Santacesaria, M. Di Serio, Industrial & Engineering Chemistry Research 2013, 52, 1168.
[13] B. S. Lane, K. Burgess, Chemical Reviews 2003, 103, 2457.
[14] J. Palanuwech, J. N. Coupland, Colloids and Surfaces A: Physicochemical and Engineering Aspects 2003.
[15] N. Mizuno, K. Yamaguchi, K. Kamata, Coordination Chemistry Reviews 2005, 249, 1944.
[16] W.-Q. Yuan, S.-Q. Zhou, Y.-Y. Jiang, H.-H. Li, H.-D. Zheng, Journal of Flow Chemistry 2020, 10, 227.
[17] G. B. Alexander, R. K. Iler, Google Patents, 1959.
[18] M. Kosmulski, Advances in Colloid and Interface Science 2016, 238, 1.
[19] S. Boakye-Ansah, M. A. Khan, M. F. Haase, The Journal of Physical Chemistry C 2020, 124, 12417.
[20] K. Stratford, R. Adhikari, I. Pagonabarraga, J.-C. Desplat, M. E. Cates, Science 2005, 309, 2198.
[21] R. K. Iler, *The chemistry of silica : solubility, polymerization, colloid and surface properties, and biochemistry*, Wiley, 1979.
[22] M. Koroleva, D. Bidanov, E. Yurtov, Physical Chemistry Chemical Physics 2019, 21, 1536.
[23] S. Sasaki, H. Maeda, Journal of Colloid and Interface Science 1994, 167, 146.
[24] S. Guo, Y. Zhu, W. Xu, S. Huan, J. Li, T. Song, L. Bai, O. J. Rojas, Carbohydrate Polymers 2022, 120154.
[25] P. Dušak, A. Mertelj, S. Kralj, D. Makovec, Journal of Colloid and Interface Science 2015, 438, 235.
[26] N. B. Alsharif, S. Muráth, B. Katana, I. Szilagyi, Advances in Colloid and Interface Science 2021, 294, 102456.
[27] O. Ben Moussa, L. Tinat, X. Jin, W. Baaziz, O. Durupthy, C. Sayag, J. Blanchard, ACS Catalysis 2018, 8, 6071.
[28] G. Wu, A. Santandreu, W. Kellogg, S. Gupta, O. Ogoke, H. Zhang, H.-L. Wang, L. Dai, Nano Energy 2016, 29, 83.
[29] F. Z. Su, Y. M. Liu, L. C. Wang, Y. Cao, H. Y. He, K. N. Fan, Angewandte Chemie 2008, 120, 340.
[30] F. Zhang, J.-b. Fan, S. Wang, Angewandte Chemie International Edition 2020, 59, 21840.

[31] J.-F. Dechézelles, C. Ciotonea, C. Catrinescu, A. Ungureanu, S. Royer, V. Nardello-Rataj, Langmuir 2020, 36, 3212.
[32] A. Sachse, V. Hulea, A. Finiels, B. Coq, F. Fajula, A. Galarneau, Journal of Catalysis 2012, 287, 62.
[33] H. Murthy, S. S. Miya, Surface and Coatings Technology 2017, 328, 13.
[34] J.-Y. CHANE-CHING, L. C. KLEIN, Journal of the American Ceramic Society 1988, 71, 86.
[35] S. Cha, H. G. Lim, M. F. Haase, K. J. Stebe, G. Y. Jung, D. Lee, Scientific Reports 2019, 9, 6363.

Summary

The shape of a liquid is dictated by surface tension, driving the liquid towards minimum surface energy configuration. Surfactant-mediated surface tension manipulation is the most common means to modify the bulk property of food, drugs, and commercial products. In recent decades a century-old discovery of Pickering and Ramsden has revolutionized the field of emulsions ranging from particle-stabilized spherical drops to 3D networks of liquid channels. The first part of my thesis (***Chapter 2***), demonstrates how can we rigidify the interface of a liquid to shape it away from the minimum surface area principle. In this project, we study various physiochemical parameters of anisotropic drop-shape formation, especially emphasizing the mechanism of non-spherical drop shape stabilization. In previous reports, anisotropic shapes of drops are stabilized by interfacial jamming of particles whereas we discovered that self-assemble silica nanoparticles at the interface can also stabilize the nonspherical structure upon crosslinking by a trivalent cation (La^{3+}). We found that a threshold volume fraction of ethanol is required to deform the shape of a droplet either via gravitation- or hydrodynamic forces. We hypothesize that non-spherical shape stabilization is achieved by the synergistic surface modification with cetyltrimethylammonium (C_6TAB) and trivalent lanthanum cations (La^{3+}). The interfacial activity of different systems is tested by the foaming of particles added with different components. To test our hypothesis, pendant drop and microfluidics experiments under different conditions (C_6TAB, La^{3+}, and $C_{16}TAB$) are performed, and obtained results confirm the difference between La^{3+} mediated interfacial crosslinking and jamming of particles. Further, we support the experimental data with force balance and particle diffusion-based monolayer formation models. The proposed models reasonably agree with the experimental data and validate the hypothesis. This method suggests an easy, scalable method with commercially available components to be applied in 3D printing and additive manufacturing.

After discussing the drop shape modulation with external means (gravity and hydrodynamic forces) we further worked on remodeling the liquid internally to form a porous liquid-liquid material. In nature, this unique architecture is formed by the spinodal phase separation of two immiscible liquids. To preserve this liquid network particles with equal affinity for both phases are employed to jam at the interface and form a bicontinuous emulsion gel (Bijels). Bijels are unique materials that allow two immiscible fluids to interact through a percolating, rigid scaffold of particles. Through this research, in ***Chapter 3*** we introduce a scalable synthesis route of nanoparticle-stabilized bicontinuous emulsion gels

with average liquid channel sizes below 500 nm and specific surface areas of 2 m^2 cm^{-3}. To elucidate the complex synthesis methods and variable dependencies of solvent transfer induced phase separation (STrIPS), we critically assess the role of each parameter towards the bijel structural variation. We hypothesize that uniform submicron bijel formation is controlled by two major factors, rapid interfacial tension evolution, and in-situ particle modification to attain amphiphilicity. First interfacial tension evolution is measured using tensiometry as a function of solvent fraction for two different solvent ternary systems (1- and 2-propanol). Solvent partitioning and interfacial tension data are used for complementary simulation studies to obtain the timeline of interfacial tension evolution during STrIPS. It is found that the 1-propanol ternary system upon demixing shows a rapid interfacial tension evolution in comparison to 2-propanol. Next, in-situ surface modification of particles is tested for both the systems and results suggest that the 1-propanol ternary system renders amphiphilic surface modifications of particles during phase separation. The combination of experimental findings and complementary simulations provides strong support for the conceptual premise of our hypothesis. This investigation described for the first time the complex dependencies of the nanoparticle surfactant modification on multiple parameters, guiding future bijel synthesis approaches.

The last part of my thesis (***Chapter 4***) discusses the functionality aspect of the bijel by introducing catalytic properties to the solid interface. We choose the alumina-catalyzed interfacial epoxidation of alkenes in the presence of hydrogen peroxide. The enormous interfacial area generated between oil and water can function as a microreactor by selective supply and removal of chemicals via the bicontinuous channels. This chapter is subdivided into three sections as per the opted strategies to make catalytic alumina bijels *i*) using alumina particles as stabilizers, *ii*) adding a small concentration of alumina particles in a silica precursor mixture, *iii*) coating the bijel with alumina using an alumina precursor. The first section attempts to translate the knowledge gained from submicron-size silica bijels by employing alumina particles (Ludox CL) as bijel stabilizers. Different structural dependencies such as pH, surfactants, salt, and nanoparticle weight percentage are examined to form uniform submicron size bijels. Obtained results suggest that the hydrophobicity of the alumina particles can not be tuned to stabilize the submicron domains and extended coarsening leads to the formation of a hierarchical porous structure. The second section discusses the possibility of adding small concentrations of alumina particles to the silica precursor mixture without losing the submicron sized domain. Finally, in the last section, we explore the prospect of interfacial coating of alumina onto silica by using an alumina precursor. Preliminary studies confirm that alumina coating preserves the bicontinuous structure and the surface remains porous for tested conditions. The present study provides the first comprehensive assessment of different alumina bijel fabrication methods however further experimental investigations are required to fully understand the implications of fabrication methods and other dependencies on catalytic properties of alumina bijels.

Samenvatting

De vorm van een vloeistof wordt bepaald door oppervlaktespanning. Deze energetische straf drijft de vloeistof naar een configuratie met een zo klein mogelijk oppervlak. Door het toevoegen van oppervlakte-actieve stoffen kan de oppervlaktespanning van een vloeistof gemanipuleerd worden. Deze techniek wordt in de industrie vaak gebruikt om de eigenschappen van voedsel, medicijnen en andere producten te wijzigen. Met het gebruik van stabiliserende colloïdale deeltjes bracht Pickering begin 20^{e} eeuw een revolutie teweeg op het gebied van emulsies, dat nu varieert van deeltjes-gestabiliseerde bolvormige druppels tot 3D-netwerken van vloeistofkanalen.

In het eerste onderzoeksdeel van mijn proefschrift (**Hoofdstuk 2**) wordt besproken hoe we het grensvlak van een vloeistof kunnen verstevigen met nanodeeltjes en het grensvlak op deze manier kunnen vervormen – iets dat dwars tegen het principe van oppervlakte-minimalisatie indruist. Uit eerdere rapporten is reeds bekend dat vloeistoffen anisotroop gestabiliseerd kunnen worden door het vastzetten van het grensvlak door adsorptie van deeltjes. In dit onderzoek bestuderen we de invloed van verschillende fysisch-chemische parameters op de formatie van deze anisotroop gevormde vloeistoffen, waarbij nadruk wordt gelegd op het stabilisatiemechanisme. We vonden dat silica nanodeeltjes die zich zelf-organiseren aan het grensvlak van een vloeistof ook non-sferische structuren kunnen stabiliseren door middel van kruiskoppeling van de deeltjes gefaciliteerd door La^{+3}-ionen. We observeerden dat onder deze omstandigheden een druppel vervormd kan worden door zwaartekracht of hydrodynamische krachten mits er ook een kritische hoeveelheid ethanol in het systeem aanwezig is. Onze hypothese is dat de vormstabilisatie wordt bereikt door de synergetische oppervlaktemodificatie van de silicadeeltjes met cetyltrimethylammonium (C_6TAB) en driewaardige lanthaankationen (La^{+3}). De grensvlakactiviteit van verschillende systemen werd getoetst door middel van de hoeveelheid schuim die ontstaat bij het schudden van de dispersies waaraan verschillende (combinaties van) componenten zijn toegevoegd. Om de hypothese verder te onderzoeken worden hangende druppel-experimenten uitgevoerd, eveneens onder aanwezigheid van nanodeeltjes, C_6TAB, La^{+3}, C_{16}TAB, of combinaties van deze componenten. In deze experimenten konden we druppelstabilisatie door middel van La^{+3}-gemedieerde kruiskoppeling van nanodeeltjes op het grensvlak onderscheiden van oppervlaktestabilisatie via simpele adsorptie van deeltjes op het grensvlak. De experimentele data wordt ondersteund met simulaties gebaseerd op krachtenbalansen en diffusie-gestuurde monolaag-formatie. De gebruikte modellen komen redelijk

overeen met de experimentele data en helpen bij het valideren van onze hypothese. Hiermee hebben we een eenvoudig en schaalbaar proces ontwikkeld voor het produceren van vloeistofstructuren waarvan alle componenten commercieel verkrijgbaar zijn en dat toegepast kan worden in 3D-printing en additive manufacturing.

Naast de vervorming van vloeistoffen door middel van externe middelen zoals zwaartekracht en hydrodynamische krachten hebben we ook gewerkt aan het fabriceren van een poreus vloeistof-vloeistof materiaal. Deze unieke architectuur wordt spontaan gevormd door de spinodale fasescheiding van twee niet-mengbare vloeistoffen. Om dit vloeibare netwerk te behouden worden deeltjes met gelijke affiniteit voor beide fasen gebruikt om aan het grensvlak te adsorberen en op deze manier het grensvlak vast te zetten. Met gebruik van deze techniek worden bicontinue emulsie-gels (bijels) gevormd. Bijels zijn unieke materialen die twee niet-mengbare vloeistofnetwerken gescheiden door een percolerend geraamte van nanodeeltjes. In **Hoofdstuk 3** introduceren we een schaalbare synthesemethode gebaseerd op oplosmiddeltransfer geïnduceerde fasescheiding (STrIPS). Deze synthesemethode resulteert in bijels waarvan de vloeistofkanaaltjes kleiner zijn dan 500 nm en de specifieke oppervlakte 2 m^2/cm^3 bedraagt. Om de complexe synthesemethode en parameter-afhankelijkheden van STrIPS op te helderen beoordelen we kritisch de rol van elke parameter in de structurele variaties van de bijel. We veronderstellen dat de vorming van uniforme submicron bijels wordt gedicteerd door twee belangrijke factoren: de snelle evolutie van de oppervlaktespanning en de in-situ oppervlaktemodificatie van de nanodeeltjes, waarbij de deeltjes amfifiel gemaakt worden. De eerste factor, de evolutie van de oppervlaktespanning, kan worden bestudeerd met behulp van tensiometrie. We meten de oppervlaktespanning als een functie van de hoeveelheid toegevoegd oplosmiddel voor twee verschillende ternaire systemen die 1- ofwel 2-propanol bevatten. Het partitiegedrag van de twee verschillende oplosmiddelen en de gemeten oppervlaktespanningen worden gebruikt voor complementaire simulaties waaruit we de tijdsevolutie van de oppervlaktespanning verkrijgen. We vonden dat de ontmenging van het ternaire systeem met 1-propanol in een veel snellere stijging van de oppervlaktespanning resulteert dan het systeem met 2-propanol. Vervolgens testten we de in-situ oppervlaktemodificatie van de deeltjes voor de twee systemen met 1- en 2-propanol. De resultaten suggereren dat in het ternaire systeem met 1-propanol de deeltjes door de oppervlaktemodificatie amfifiel worden tijdens de fasescheiding. De combinatie van de experimentele bevindingen en de complementaire simulaties biedt sterke ondersteuning voor het conceptuele uitgangspunt van onze hypothese. Dit onderzoek beschrijft voor het eerst de complexe parameter-afhankelijkheden van de modificatie van deeltjesoppervlakken door oppervlakte-actieve stoffen. Dit begrip is van groot belang voor het ontwikkelen van synthesemethoden voor bijels.

Het laatste deel van mijn proefschrift (**Hoofdstuk 4**) bespreekt een praktische toepassing van bijels door het introduceren van katalytische eigenschappen in het vaste geraamte van de bijel. We bespreken de alumina-gekatalyseerde epoxidatie van alkenen in de aanwezigheid van waterstofperoxide. Het

enorme grensoppervlak dat aanwezig is tussen de olie- en waterfasen van de bijel kan dienst doen als een microreactor, waarbij chemicaliën selectief aan- en afgevoerd kunnen worden door de bicontinue kanaalsystemen. Dit hoofdstuk is opgedeeld in drie secties die elk een strategie bespreken voor het maken van katalytische alumina bijels. Deze zijn i) het gebruik van aluminadeeltjes als bijel stabilisators, ii) het toevoegen van lage concentraties aluminadeeltjes in een silicadeeltjes-bevattende bijel precursorvloeistof en iii) het aanbrengen van een laagje alumina op de bijel met behulp van alumina precursors. In de eerste sectie wordt de kennis die vergaard is in de fabricatie van submicron bijels met behulp van silicadeeltjes vertaald naar een nieuw systeem waarin aluminadeeltjes (Ludox CL) gebruikt worden om de bijel te stabiliseren. Verschillende afhankelijkheden zoals de pH, het gebruik van oppervlakte-actieve stoffen, de aanwezigheid van zout, en de gebruikte hoeveelheid nanodeeltjes worden bestudeerd met het doel bijels met submicron domeinen te kunnen maken. De resultaten suggereren dat de hydrofobiciteit van de aluminadeeltjes niet juist afgestemd kan worden. Hierdoor is de stabilisatie van de submicron domeinen niet effectief en groeien de poriën uit tot een hiërarchische poreuze structuur. In de tweede sectie bekijken we of we kleine hoeveelheden aluminadeeeltjes toe te voegen aan de silicahoudende percursorvloeistof toe te voegen zonder de submicron domeinen van de resulterende bijel te verliezen. Tot slot verkennen we in de laatste sectie de optie om een laagje alumina op het silicaoppervlak van de bijel aan te brengen met behulp van een alumina precursor. Preliminair onderzoek bevestigt dat de bicontinue structuur behouden blijft bij het aanbrengen van een alumina coating en dat de oppervlakte van de bijel poreus blijft onder de gebruikte omstandigheden. De verkregen resultaten bieden een eerste uitgebreide toetsing van verschillende alumina-bijel fabricatiemethoden. Er is echter meer experimenteel onderzoek nodig om de verdere implicaties van de verschillende methoden en de katalytische eigenschappen van deze materialen volledig te begrijpen.

Volume 17
Number 8
28 February 2021
Pages 2013–2342

Soft Matter

rsc.li/soft-matter-journal

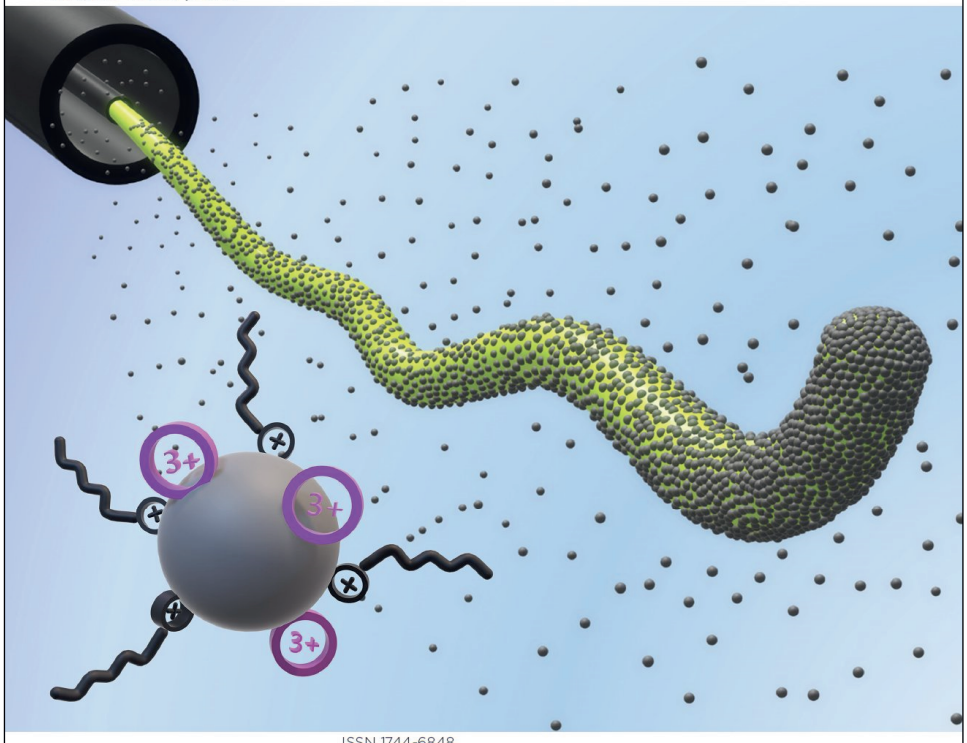

ISSN 1744-6848

ROYAL SOCIETY OF CHEMISTRY

PAPER
Mohd A. Khan and Martin F. Haase
Stabilizing liquid drops in nonequilibrium shapes by the interfacial crosslinking of nanoparticles

Publications

Ph.D. publications

1. **Khan, M. A.**, & Haase, M. F. (2021). Stabilizing liquid drops in nonequilibrium shapes by the interfacial crosslinking of nanoparticles. ***Soft Matter***, *17*(8), 2034-2041.

2. **Khan, M. A.***, Sprockel, A. J.*, Macmillan, K. A., Alting, M. T., Kharal, S. P., Boakye-Ansah, S., & Haase, M. F. (2022). Nanostructured, Fluid-Bicontinuous Gels for Continuous-Flow Liquid–Liquid Extraction. ***Advanced Materials***, 2109547. (first authors*)

3. Sprockel, Alessio J.* and **Khan, Mohd A.*** and de Ruiter, Mariska and Alting, Meyer T. and Macmillan, Katherine A. and Haase, Martin F., Fabrication of Bijels with Sub-Micron Domains with a Single-Channel Flow Device (Under review) (first authors*)

4. **Khan, M. A.**, & Haase, M. F. Fabrication of catalytic alumina bijel for in-situ epoxidation of alkenes to produce epoxides (*in preparation)*

Other publications

1. Boakye-Ansah, S., **Khan, M. A**., & Haase, M. F. (2020). Controlling surfactant adsorption on highly charged nanoparticles to stabilize bijels. ***The Journal of Physical Chemistry C***, *124*(23), 12417-12423.

2. Pareek, V., Gupta, R., Devineau, S., Sivasankaran, S. K., Bhargava, A., **Khan, M. A**., ... & Panwar, J. (2022). Does Silver in Different Forms Affect Bacterial Susceptibility and Resistance? A Mechanistic Perspective. ***ACS Applied Bio Materials***,

About the author

Mohd Azeem Khan was born in the Indian town of Gyanpur, which is close to the spiritual city of Varanasi. He finished his schooling in his hometown before moving 1865 kilometers to the south to begin his bachelor's degree in biotechnology (B.tech) at Vellore Institute of Technology (VIT). He was actively involved in academic and extracurricular activities during his bachelor's studies. His early interest in research led him to work on projects such as keratin waste biodegradation and arsenic nanoparticle synthesis for cancer treatment. Under the supervision of Prof. Amitava Mukharjee at the Nanobiotechnology Center (CNBT-VIT), he completed his bachelor thesis focused on Chromium (VI) sensing using gold nanorods. Further, he started his master's in engineering (M.E., biotechnology) at BITS Pilani in Rajasthan. The research-oriented curriculum at BITS aided him in developing his interest in nanobiotechnology. He worked on the biosynthesis of silver and gold nanoparticles using metal-tolerant fungus during his master's degree. Under the supervision of Prof. Jitendra Panwar, his master's thesis project resulted in two research papers based on systematic mechanistic studies of nanoparticle cell interactions and application-based assays. He also qualified for various national scholarship tests, such as the Junior Research Fellowship, Department of Science and Technology (JRF-DST) and the National Eligibility Test (NET). Before starting his Ph.D.he worked at various research institutions such as TERI-Deakin Institute of Biotechnology, BK-project Yeungnam University, and the Indian Institute of Technology Bombay (IITB). Azeem began his Ph.D. with Dr.Martin Haase in the United States in 2018 and moved to the Netherlands with him in 2019 to join Physical and Colloid Chemistry (FCC) at the Debye Institute for Nanomaterials Science, Utrecht University. The majority of the research described in this thesis was conducted at the FCC under Martin's supervision. Azeem supervised two master thesis projects, several bachelor projects and gave exercise classes. As part of his Ph.D. training program, he attended winter and spring Debye schools, as well as several seminars such as Debye lunch lectures and nanoseminars. He presented his research at national and international conferences such as AIChE (Atlanta, USA-2019), CHAINS (Veldhoven, Netherlands-2019,20), ECIS (Athens, Greece-2021), and GCS (Berlin, Germany-2022). The poster presentation in Germany was awarded the best poster prize. Three research papers are published from his Ph.D. project and he also co-authored two research papers from other collaborative projects.

Acknowledgment

The Ph.D. is a liminal space where learning prepares a student's transition to not only an academic or industrial role but for life. Starting of my Ph.D. journey was full of surprising challenges and now when I look back I have no regrets that I wandered off on those trails to realize what I liked the most. I remember my first interview with Martin vividly it was 1 am in Daegu, South Korea December 2017. He described his research on bijels and almost immediately I was convinced to work on bijels. After that, for weeks I had no news and suddenly one day late in the night I got a call from Martin offering a Ph.D. position. From there till now I find my journey quite an anecdote, full of challenges, learning and rewards.

First and foremost I am extremely grateful to my supervisor, Dr. Martin Haase for his valuable pieces of advice, continuous support, and patience during my Ph.D. journey. He encouraged me to think critically in order to develop my own ideas and approaches, which has aided my development as a researcher and professional. His excitement is very infectious and at times helped me to keep my motivation up to go back to the lab and try new experiments. His office doors were always open for questions, discussions, or just a quick chat, which almost always ended up in us being in the lab. I am grateful for the time and effort he has put into me and the project, and I am glad to realize that I have also adopted some of his perfectionist approach.

I would like to specially thank Prof. dr. W.K. Kegel, who has been a constant source of support throughout my Ph.D. journey and a go-to person for advice. I would also like to thank my assessment committee members, Prof. dr. A. Meijerink, Prof. dr. D. Bonn, Prof. dr. P.E. de Jongh, Prof. dr. A.P. Philipse and Prof. T. Zemb for their valuable insights and feedback on my thesis.

After moving from the US to the Netherlands the first two people I became friends with were James and Alessio. I would like to thank James for being a great friend, housemate, and banter buddy during that difficult time of COVID-19 pandemic. Alessio (bijel brother) was a constant support system in every possible way, not only in research but also and more importantly, as a friend; I treasure our time in labs, working on papers, and going to the gym. Last but not least I would like to appreciate my favorite officemate, Mariska. She is one of the most kind person I have met so far, her positive attitude made our shared workspace a warm and welcoming environment. Also, I have to especially thank her

for keeping up with all impromptu conversations, floating ideas and being the first critique of anything I have made or written during my Ph.D.

I consider myself fortunate to have had such a pleasant research group in which we all collaborated and helped each other succeed in our individual projects. I would like to take this opportunity to thank Henrik (productive boy), Matthijs, Katherine, Marieke and Jesse (long-long man) for their helpfulness, and friendly demeanor which made every day at work a little brighter. I can't miss out Neshat (Nishat, thesis buddy), your unwavering spirit, passion for drama, and infectious energy never cease to amaze (irritate) me, and I think we both should do something about our food cravings at work. Alex (my second housemate), I am continuously impressed by your ability to deliver awful jokes, and I know we will never agree on who told the worse (probably Joren). I'd like to thank Amanda for all of our wonderful conversations about food and our fictitious plans(party, movies).

A big thanks to all the technicians at the physical and colloidal chemistry (FCC) group Alex, Dominique and Bonnie. I always felt welcomed and found the right help/advice from your offices. I am also grateful to my other colleagues especially Joren for taking nice pictures of my defense ceremony (candid photographer), Stephen, Shankar, Mathew, Fara, Riande, Daniel, Mengwei, and Geert who made my Ph.D. journey even more pleasant. I learned a lot from my master's students Jelle and Steffen, I am grateful to be a part of your learning journey.

I feel lucky to have a friend like Raimon, your positive energy is contagious and brightens up even the dullest of days. Nikos, I must admit that I find you amusing, and it only gets better when you explain the joke to Raimon the second time. Akshita, Ruchika, and Nandish, you guys have been a huge support and a much-needed source of Indian food and culture at times. Even after being continents apart my friends in India and abroad showered great support and encouragement, Amol, Parul, Gaurav, Itisha, Etee, and Pooja and many more thank you all for being there.

I would also like to thank my family for their unwavering support and understanding throughout this journey. Their love and encouragement have been a constant source of motivation and inspiration for me. My mother is one of the most important people in my life, and I am so grateful for all that she has done for me. I will never be able to repay my parents for everything they have done for me, but I will always strive to make them proud and to be the kind and loving person that they have taught me to be. Without a doubt, I have the best siblings in the world, and I will miss you all during my Ph.D. defense.

Finally, I would like to acknowledge all the participants who generously agreed to help, contribute, and collaborate with me in past four years. Their contributions have been invaluable to my research.

This acknowledgment is just a small token of my appreciation for all the support and guidance I have received. I am deeply grateful to each and every one of you for your role in my academic and personal journey.